Experimental Cascade Simulation of First Stage High Pressure Gas Turbine with Effects of Leakage Flow and Contouring on Endwall Film Cooling

A THESIS

SUBMITTED TO THE FACULTY OF

UNIVERSITY OF MINNESOTA

BY

Reema Saxena

IN PARTIAL FULFILLMENT OF THE REQUIREMENTS

FOR THE DEGREE OF

MASTER OF SCIENCE IN MECHANICAL ENGINEERING

Dr. Terrence W. Simon, Adviser

JUNE 2015

ACKNOWLEDGEMENTS

The development of this work has been made possible with the help and blessings of several people to whom I would like to extend my heartfelt gratitude. First and foremost, I want to thank Professor Simon who considered me eligible to join the Heat Transfer Laboratory and work on this project. The experience working with him has been very enriching. His deep technical knowledge of the subject and words of wisdom helped me get past hard times. Also, his friendly nature made it really easy for me to adjust to the new country and its ways.

I would like to acknowledge Solar Turbines Inc. for its sponsorship of the project. In particular, I would like to thank Luzeng Zhang and Hee Koo Moon for their valuable inputs throughout the project.

I would also like to extend my gratitude to Michael Jensen and Pat Nelson from the Mechanical Engineering Research Shop. It was very pleasant collaborating with them for the manufacturing of the test facility.

Next, I want to acknowledge the contribution of Yuh Yen Seah in the experiments on the rotor cascade test facility, some of whose results are discussed in the present work. I also want to thank Mahmood Alqefl and Zhao Liu for their immense help during the setting up of the test facility, members of our research group Longzhong Huang, Chao Zhang, Leanne Reich, Hunkwan Park and Lake Chen for their sound advices on complicated problems encountered during the project.

Finally, I want to thank my parents for their constant support and blessings. Their encouragement strengthens me to undertake even the most complicated tasks and perform to the best of my ability.

ABSTRACT

Flow in a high pressure gas turbine passage is complex, involving systems of secondary vortex flows and strong transverse pressure gradients. This complexity causes difficulty in providing film cooling coverage to the hub endwall (or platform) region which is subjected to high thermal loading due to combustor exit hot core gases. Therefore, an improved understanding of these flow features and their effects on endwall heat transfer is needed to assist designers in developing efficient cooling schemes.

The present experimental study is performed in a linear, stationary cascade with a contoured endwall, representing a first stage stator of a high pressure gas turbine. Passage thermal fields and endwall adiabatic effectiveness values are measured using a traversing thermocouple probe. Engine representative conditions such as high free stream turbulence, large eddy length scales, high Reynolds number, leakage mass flow ratios of 0.5%, 1.0% and 1.5%, and engine representative approach flow dimensionless temperature profiles are set up. Rotation effects, coolant density ratios and Mach number effects, however, are absent. Performance of the *stator* cascade test facility is also compared to that of another cascade test facility in the Heat Transfer Laboratory that represents a first stage *rotor*. The comparison allows assessment of the varying coolant flow migration patterns for both cascades under different design and operational conditions.

Results show that a 'thin' geometry of the leakage slot in the stator cascade enables coolant to be ejected out quite uniformly, although a greater amount of coolant lies nearer to the suction side region. Better coolant spread is also observed near the trailing regions of the passage. On the other hand, in the rotor cascade the coolant undergoes

undesirable mixing within a much larger slot, subsequently leading to lower effectiveness values in the passage particularly on the pressure side and trailing edge regions. A combined effect of slot geometry, endwall profile shape, and mass and momentum flux ratio is identified as an important determinant in assessing the film cooling effectiveness for both turbine passage configurations.

Table of Contents

LIST OF TABLES

LIST OF FIGURES

NOMENCLATURE

Symbols

A, B, n	Hotwire Calibration Constants [dimensionless]
C	Blade True Chord Length [m]
C_{ax}	Blade Axial Chord Length [m]
C_P	Blade Mid-Span Static Pressure Loss Coefficient [dimensionless]
E (w)	Energy Density Spectrum [m^2/s^2.Hz]
Lu	Turbulence Energy Length Scale [m]
$\overline{U}$	Time Averaged Mean of Velocity in Axial Direction [m/s]
u(t)	Instantaneous Velocity [m/s]
u'(t)	Instantaneous Fluctuation about Time Averaged Mean Velocity [m/s]
U_{RMS}	Root Mean Square of Velocity Fluctuations [m/s]
M	Mach Number [dimensionless]
MFR	Mass Flow Rate Ratio of Leakage to Mainstream Flow [%]
N	Sample Size [dimensionless]
P_s	Static Pressure [Pa]
P_t	Total Pressure [Pa]
Q	Volumetric Flow Rate [m^3/s]
R	Specific Gas Constant for Air [J/kg.K]
Re_C	Reynolds Number scaled on Blade's True Chord Length [dimensionless]
Re_{Lu}	Reynolds Number scaled on Energy Length Scale [dimensionless]
Re_λ	Reynolds Number scaled on Taylor Microscale [dimensionless]
S_i	Blade Span at Inlet of Cascade [m]
S_e	Blade Span at Exit of Cascade [m]
P	Cascade Pitch (blade spacing) [m]
T	Absolute Temperature [K]
Tu	Turbulence Intensity [%]
U_O	Approach Flow Velocity [m/s]

Greek

ρ	Density [kg/m^3]
Δ	Difference Operator
Λ	Turbulence Integral Length Scale [m]
η	Endwall Adiabatic Effectiveness [dimensionless]
θ	Recovery Temperature Field [dimensionless]
ε	Turbulent Kinetic Energy Dissipate Rate [m^2/s^3]
λ	Taylor Microscale [m]
ν	Kinematic Viscosity [m^2/s]
w	Frequency of Energy Density Spectrum [Hz]
w_s	Sampling Frequency [Hz]
μ	Dynamic Viscosity [Pa.sec]

Subscripts

o	Located at Passage Inlet Plane
w	Located at wall (z=0)
L	Leakage flow property
M	Mainstream flow property
x	Passage Axial Coordinate [m]
y	Passage Pitchwise Coordinate [m]
z	Passage Spanwise Coordinate [m]

Chapter 1 Introduction

1.1. Motivation

Gas turbines are an integral part of our lives providing electricity, powering aircraft and ships, supplying fuel to our homes and running power plants. As a result of the endeavors by engineers all over the globe with efforts dating back to the 1900s, the thermal efficiency of gas turbines has been greatly enhanced (reaching as high as 60% for combined plants). Although thermal efficiency is achieved through a combination of methods, one of the most significant methods is to increase the turbine inlet temperature. In modern turbines, this temperature can be as high as 1600˚C. This creates an extremely hot environment within the gas turbine, particularly the high pressure turbine stage. One of the several turbine components exposed to these conditions is the hub endwall (or platform) of the first stage high pressure turbine which is the focus of the present study. Recent regulations on the exhaust emissions have led to improved combustor designs which lower the 'peak' combustion temperature and, consequently, the emission of gases like nitrous oxides. This is, however, accompanied by more efficient mixing within the combustion chambers leading to 'flatter' combustor exit temperature profiles. This results in hotter core gases reaching nearer to the endwall. Therefore, given material limitations, efficient endwall protection strategies that can be included with certainty in new gas turbine designs are needed. Several techniques can be employed to address the issue of high thermal loading of the endwall such as thermal barrier coatings and film cooling through an array of shaped holes or slots. The flow field within the high pressure turbine passage is quite complex, involving strong secondary flows and transverse pressure gradients. These features collectively tend to disrupt the coolant coverage over the endwall. Given these

complexities, cooling becomes difficult making it important to understand the flow physics and its relation to the endwall heat transfer. This knowledge may serve as a guide for gas turbine designers to develop better endwall protection methods.

Several cooling flows are introduced into the turbine passage such as ‘leakage flows’. Besides sealing the interfacial clearances between components, these flows also have high cooling potential [1], [2], [3]. In addition to this, coolant coming from the combustor liner also contributes significantly to the coolant coverage. Another method used to improve the effectiveness of the various cooling flows is the ability to weaken the secondary flow structures. This can be achieved by the use of endwall that is ‘contoured’ [4], [5]. There have been several studies on these topics (some of them cited above). However, the present study adds to the literature an understanding of the flow physics in the *combined* presence of leakage flow, combustor liner coolant and endwall contouring for two separate cascade configurations.

1.2. Objective

The present experimental study aims to develop an understanding of the flow physics within the first stage of a high pressure gas turbine passage. The major experimental conditions include varying mass flow rates of leakage flow, the presence of combustor liner coolant in approach flow and endwall contouring. Experimental results are analyzed from two separate cascade test facilities, the stator stage cascade and rotor stage cascade, with an aim to compare the resultant passage thermal fields and endwall adiabatic effectiveness. This analysis can help determine the effect of secondary flow structures on the coolant flow migration and mixing occurring within the passage. The final objective of the study is to assist designers in determining the applicability of these features in a real turbine.

Chapter 2 Background

The turbine endwall aerodynamics and heat transfer have always been topics of interest for researchers. One can find a plethora of papers investigating the complex flow features of a gas turbine passage and discussing methods to manage secondary flows and achieve enhanced cooling of the endwall. The background provided herein is a summary of several interesting studies performed on this topic, some of which date back to the 1950's. The reader is encouraged to read these articles cited as references through the text for a more comprehensive understanding of the topic.

"Often it is possible to study and understand a simple member of a fluid flow family and predict the behavior of a more complex flow of that family" [6]. Linear cascades and rotational test rigs are methods to visualize flow in an actual gas turbine in a simplified manner. The discussions below begin with some of the early pioneering studies performed in linear cascades. The first section describes the turbine endwall aerodynamics as understood currently followed by discussions on the methods to modify the endwall by means of axisymmetric and non-symmetric contouring. Next the studies involving turbine endwall heat transfer are reviewed followed by the effects of film cooling by injection blowing over the endwall. These discussions are to give the reader a greater understanding of the background and objective of the current study.

2.1. Turbine Passage Flows

Many early studies including those by Herzig et al. [7], Eckerle and Langston [8], Peirce and Shin [9], and Goldstein and Karni [10] present visualization of the secondary flow structure formation within the passage. They describe the process in which the passage approach flow undergoes three dimensional separation of the flow at the junction of the

airfoil and the endwall. In their review study, Simon and Piggush [11] explain the formation of secondary flows. The endwall approach flow boundary layer has a dynamic pressure gradient due to the velocity gradient within the boundary layer. On stagnating at the junction, this total pressure gradient becomes the endwall-normal pressure gradient. The fluid within the boundary layer as a result of this pressure gradient moves towards the endwall migrating slightly upstream of the leading edge where it rolls into a vortex. This is popularly known as the horseshoe vortex. Also dominant within the passage is the flow that is driven from the pressure side to the suction side of the passage due to the cross-stream pressure gradient from the pressure side to the suction side. This is sometimes referred to as the passage secondary flow. The interactions of this type of flow with the horseshoe vortex combined with several corner vortices cause the passage flow field to be quite complex.

Building upon these early efforts were further studies including popular ones by Langston [12] and Langston et al. [13] that describe the flow features in detail (Figure 2-1). The location of the saddle point is approximated to be around 20%-50% of the pitch distance from pressure side to suction side. A horseshoe vortex is created between the saddle point and the airfoil-endwall leading edge junction. This vortex divides into its suction side leg that wraps around the suction side of airfoil-endwall within the passage and a pressure side leg which, as was proposed by Langston, gets augmented due to the cross-stream passage flows. Another conclusion drawn in their study was the formation of a new boundary layer within the passage downstream of the separation line after the inlet boundary layer is separated as it encounters the leading edge region.

Another study was performed by Sieverding and Van den Bosche [14] using colored smoke to visualize the secondary flow structures (Figure 2-2). It was concluded from the study that the aforementioned passage flows cause the stream surface to rotate and result into what is often cited in the literature as the passage vortex. The passage vortex increases the effect of secondary flows on the passage flow field as it tends to entrain the flow that was originally outside the region affected by the horseshoe vortex. Studies by Kawai et al.[15] and Chung and Simon [16] corroborate these findings with important

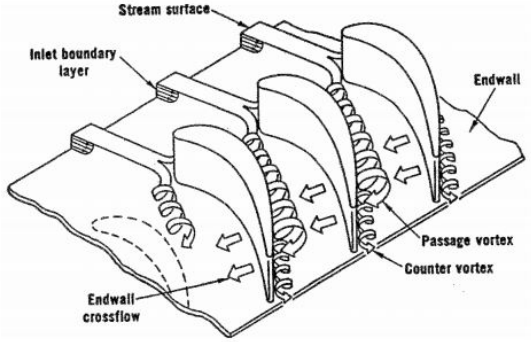

Figure 2-1: Development of endwall secondary flows by Langston [12]

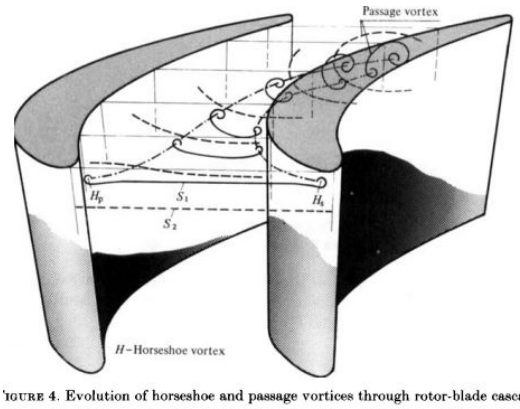

IGURE 4. Evolution of horseshoe and passage vortices through rotor-blade cascade.

Figure 2-2: Evolution of horseshoe and passage vortex by Sieverding and Bosche [14]

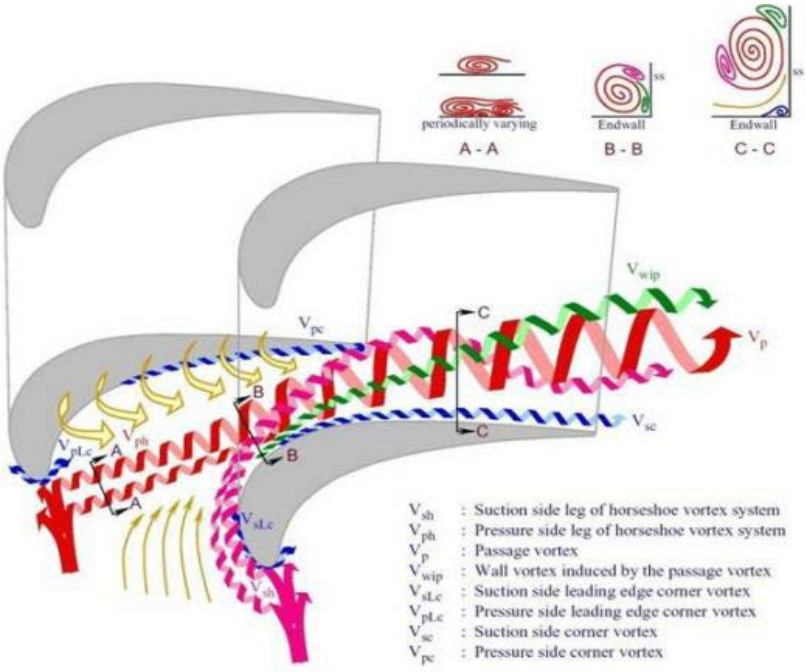

Figure 2-3: Endwall secondary flow model by Wang et al. [17]

additions to details of the flow within the passage. Figure 2-3 depicts the endwall secondary flow model proposed by Wang et al. [17]. The turbine passage is mainly dominated by the passage vortex that evolves from the pressure side leg of the horseshoe vortex and the endwall cross flows. The suction side leg of the horseshoe vortex has an opposite sense of rotation and hence weakened due to the shear with the passage vortex and the endwall cross flow. Also seen in the model are the various corner vortices that contribute to the complexity of the flow field within the passage.

Modification of Endwall

The studies reviewed above deal with cascade flows with flat endwalls. The fact that the secondary flows may cause undesirable aerodynamic losses as well as impact the endwall heat transfer led the researchers to develop techniques to reduce or weaken their effects, some of which are discussed in the following sections.

1. Axisymmetric and Non-axisymmetric Contoured Endwall

One of the methods to achieve the objective mentioned above is to make one, or both endwalls within the passage contoured. The acceleration caused by contouring the endwall tends to make the boundary layer thin, which, in turn, causes the secondary flows to weaken. The endwall may be contoured upstream of the leading edge and/or within the passage. The shape as well as the location of the beginning and end of the contouring are important parameters on which a gas turbine engine designer focuses. Contouring of the endwall can be achieved in an axisymmetric or non-axisymmetric manner (Figure 2-4). The term “axisymmetric” is used in reference to the engine geometry although the studies discussed here mostly were performed on straight linear cascades.

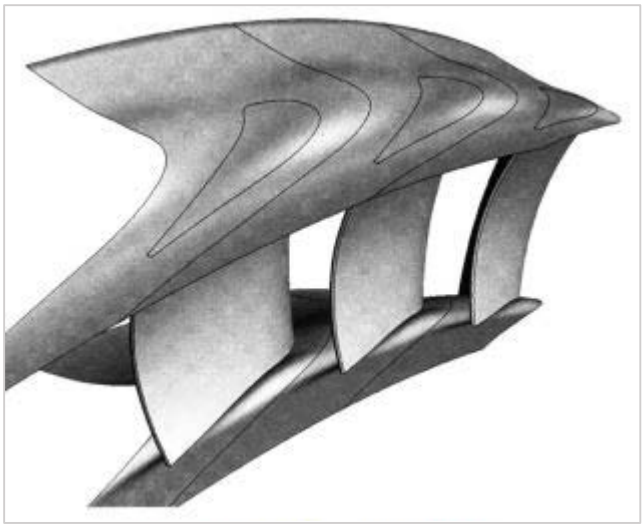

Figure 2-4: High pressure nozzle guide vane with non-axisymmetric contoured endwall [21]

One of the early studies, performed by Kopper et al. [18], investigated the effects of axisymmetric endwall profiling. It was found that the cascade with profiled endwalls yielded lower pressure losses as compared to the cascade with flat endwalls. Testing was conducted at an isentropic exit Mach number of 0.85, although the secondary loss results agreed reasonably well with the correlations developed from incompressible flow testing of similar configurations. A detailed characterization of the flow field within a cascade with endwall contouring was given by Burd and Simon [4]. They have documented the streamwise and cross stream velocities, turbulence and velocity fluctuations along with total pressure losses and kinetic energy losses. In a recent examination of axisymmetric contouring by Miyoshi and Higuchi [5], computational and experimental evaluation of contouring is performed in a high pressure turbine nozzle test rig. The numerical and experimental results with the baseline axisymmetric endwall case are compared. Their target was to control the horseshoe vortex at the leading edge and the secondary flows in the passage. The results showed a 27% reduction of the pressure loss coefficient in the numerical approach and 35% in the experimental approach.

Due to the difficulties associated with the physical testing of the non-axisymmetric contouring of the endwall, it is typically designed using CFD as a tool. Some of the studies performed include those by Brennan et al. [19], Rose et al. [20] and Schobeiri and Lu [21]. Most of these studies indicate that a well-designed non-axisymmetric contoured endwall may prove to be a viable option to decrease the losses associated with secondary flows. Also, the non-axisymmetric profile may help reduce exit angle non-uniformities of the flow.

2. Boundary Layer Fences and Jets

The use of a boundary layer fence to reduce the strength of secondary flows has been investigated in several studies. Chung et al. [22] examined the fence located on the endwall at mid-pitch of the passage. As discussed above, in an unfenced passage, the pressure side leg of the horseshoe vortex is strengthened by the boundary layer flow that gets skewed within the passage. The near-endwall portion of the boundary layer flow migrates towards the suction side due to the existence of a cross-stream pressure gradient. The fluid in the upper portions of the boundary layer moves forward along with the mainstream flow. The high shear component normal to the horseshoe vortex axis intensifies the pressure side of the horseshoe vortex embedded in this boundary layer. Chung et al. found that by introducing the fence into the flow at the mid-pitch location within the passage, the vortex leg augmentation by this mechanism is prevented and the vortex leg lifts up into the main flow within the passage and rotates into the direction of the main flow. Thus, the vortex is weakened until it reaches the downstream locations of the passage and is displaced both from the endwall and the suction surface. Hence, its impact on endwall heat transfer is reduced. In another study, Kawai et al.[23] used fences of varying heights and positions along the endwall. They concluded that the secondary flows within the passage are greatly reduced by the choice of right size and position on the

endwall. However, the survival of the fences in the hot gas environment of an actual gas turbine is difficult, making it hard to implement this idea.

Use of jets to impact the secondary flow field within the passage has also been a technique that has intrigued researchers. These jets are located on the endwall and are used to divert the pressure side leg of the horseshoe vortex. Aunapu et al. [24] studied the effects of these jets placed on the mid-pitch line within the passage. They were successful in inhibiting the migration of pressure side leg of the horseshoe vortex. But it was noted that the secondary losses increased due to the additional turbulence caused by the jets.

2.2. Turbine Endwall Heat Transfer

After reviewing the existing knowledge on secondary flows within a turbine passage, the next step in accordance with our objective to study endwall adiabatic effectiveness is to understand the extent of the impact of secondary flows upon endwall heat transfer. Vortices of varying intensities have been shown to cause variations in local heat transfer coefficients. In some of the early efforts, Blair [25] indicated that the heat transfer was high in the region near the leading edge of the vanes due to the existence of the horseshoe vortex. The resolution of the study, however, was not high enough to capture the detailed distribution of the heat transfer coefficients. A more complete picture was given by Graziani et al. [26] where it was observed that the leading edge experienced high heat transfer rates due to the horseshoe vortex, supporting Blair's study. Also, they observed a distinct wedge-shaped region bounded by the leading edge plane, the suction side leading edge separation line and the separation line of the pressure side leg of the horseshoe vortex. The heat transfer rate was approximately equal to that of the incoming boundary layer. A steep decrease of heat transfer rates was observed downstream of the separation line of the pressure side leg of the horseshoe vortex with low heat transfer rates

continuing until the trailing edge. It was noted that a new boundary layer must form since the inlet boundary layer is already rolled up into the horseshoe vortex. Therefore, the heat transfer rates over the endwall at the throat and within the passage are dependent on the inlet boundary layer thickness. Also noted was the high heat transfer rate region in the wake region behind the trailing edge region. Correlations were proposed by Kumar et al. [27] to compute average heat transfer rates within the passage.

An interesting study was performed by Goldstein and Spores [28] to compute Stanton number contours over the endwall in a linear cascade using the concept of heat and mass transfer analogy (Figure 2-5). This, low approach flow turbulence study, involved high spatial resolution and used naphthalene mass transfer sublimation experiments to apply to the heat and mass transfer analogy for calculation of Stanton number. Many of the previous findings, as discussed above, were confirmed and supplied with detailed explanations of the turbine endwall heat transfer characteristics. Visualization of the

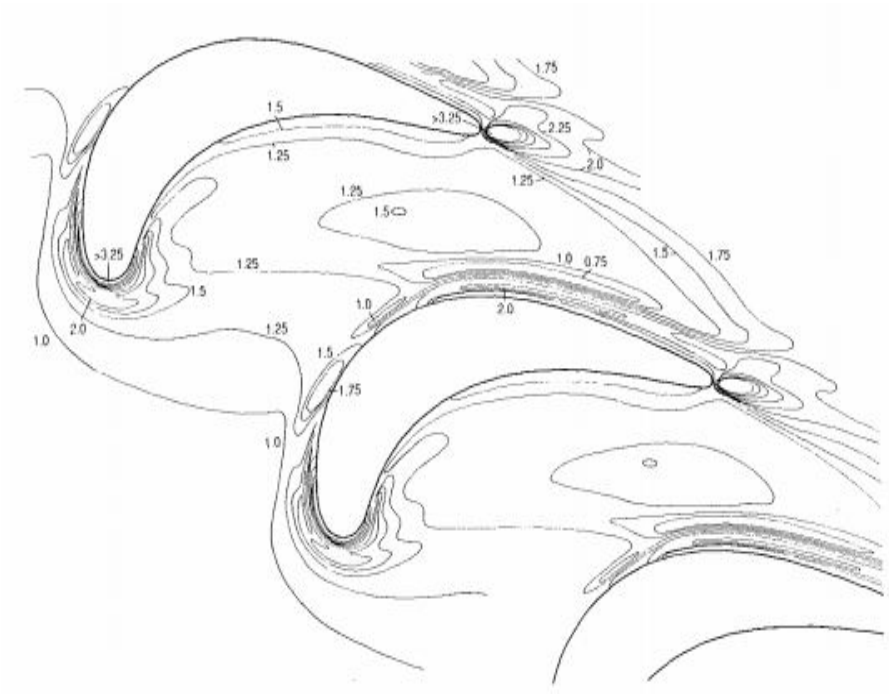

Figure 2-5: Stanton number contours showing the effect of secondary flows on endwall heat transfer [28]

effects of corner vortices was greatly enhanced. High heat transfer zones were observed in the leading edge and trailing edge regions. In the trailing edge region, two peaks of heat transfer were seen, one of which was attributed to the recirculating wakes. The other occurred nearer the suction side, and was interpreted as a result of the intensification of the vorticity due to the interaction of suction side corner vortices and the trailing edge wakes.

Effect of Free Stream Turbulence

The flow exiting the combustor in a gas turbine has high turbulence intensity values and large turbulence length scales. Therefore, it is important to review the literature to learn more about the effects of turbulence on the endwall heat transfer. High free stream turbulence can trigger earlier transition to turbulence of the endwall boundary layer. This can cause higher temperature fluid nearer to the endwall due to the increased momentum transport by turbulent eddies which can eventually cause higher endwall heat transfer [29]. Lee et al. [30] also reported that the higher free stream turbulence levels increases heat transfer throughout the passage, but with reduced effect near the trailing edge. Another study [31] performed in a rotor cascade showed that the high free stream turbulence enhances the heat/mass transfer in the central area of the turbine passage, thus making the endwall heat load more uniform.

Effect of Mach number

The experimental studies performed on turbine cascades often only involve low Mach number conditions. In fact, most of the studies reviewed above did not have engine representative Mach numbers. Perdichizzi [32] evaluated the effect of high Mach number on the secondary flow structures formed downstream of the turbine cascade. He observed

that the passage vortex migrates nearer to the endwall. Hermanson and Thole [33] noted that the development of secondary flows is similar to transonic flows up to the location of the shock.

Effect of Surface Roughness

The surface roughness of the turbine endwall has a significant effect on the endwall heat transfer rates. Since this effect is not being simulated in our test facility, it is important to understand the extent that this effect may have in an actual gas turbine. It was found by Blair [34] that the roughness causes an early transition of the endwall boundary layer to turbulent flow which in turn increases the heat transfer rate over the endwall. Some more recent studies performed on this subject include those by Lorenz et al. [35] and [36].

2.3. Endwall Blowing (Film Cooling)

The following sections discuss studies based on the interaction of 'leakage' flows with the mainstream flow and the resulting secondary flow structures. This discussion is then followed by the cooling potential of these leakage flows and the extent of the coverage they provide on the endwall surface.

2.3.1. Interaction of Secondary flows with Cooling Flows

External film cooling is one of the most commonly used techniques to protect the hub endwall region from the hot core gases exiting the combustor in a high pressure turbine. The film cooling and the associated heat transfer are strongly influenced by the secondary flow structures within the passage. Several efforts have focused on studying the interaction of coolant flows with the mainstream flow and the flow field as affected by the secondary flows.

In one of the earlier studies, Sieverding and Wilputte [37] introduced coolant by means of two double rows of discrete holes within the passage and a double row upstream of the leading edge. They confirmed the reduction in losses and exit angle non-uniformity along the airfoil axis. They noted that the coolant to mainstream total pressure ratio, the coolant mass flow ratio and the relative angles between the coolant flow, main flow and endwall boundary layer are all important parameters that determine whether or not the coolant has an optimal effect on the endwall heat transfer. In yet another study by Biesinger and Gregory-Smith [38], it was concluded that the blowing rate of the cooling air is important in determining its effect on the secondary flows. It was shown that at low rates of injection of the coolant, the boundary layer tends to thicken resulting in higher secondary flow losses. Conversely, at higher rates of injection, the boundary layer has added momentum thus counteracting the effects of secondary flows. However, at higher rates of injection, the possibility of coolant penetrating into the mainstream flow is high.

In a more recent study by Yapa et al. [39] the endwall vortex effects on film coolant are studied by means of full flow field, three dimensional velocity and concentration measurements using magnetic resonance imaging in a nozzle vane cascade. The cross flow vorticity on the vane's suction side is observed to roll up into the passage vortex that tends to strongly distort the streamlines near the endwall. The turbulent dispersion of coolant was measured to be quite high due to the effects of the passage vortex. The aerodynamic performance of the turbine stage as affected by the purge (or leakage) flow was examined by Ghopa et al. [40]. The overall total pressure loss was found proportional to the mass flow rates of the purge flow. The position of the pressure loss core was observed to move towards the midspan due to strengthening of the pressure side leg of

the horseshoe vortex and the consequent upward deflection of the leading edge corner vortex.

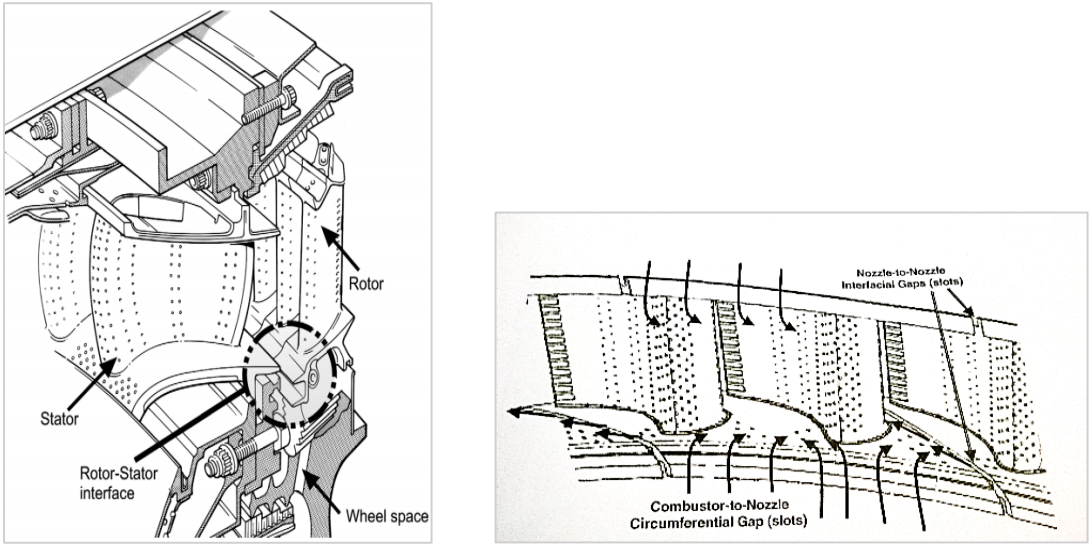

Figure 2-6: (Left): First stage rotor-stator disc cavity (Image Courtesy: Rolls Royce); (Right) Combustor-to-nozzle interfacial slot (Image Courtesy: Von Karman Institute for Fluid Dynamics)

2.3.2. Film Coolant Enhancement due to Leakage Flows, Combustor Liner Coolant and Endwall Contouring

The rotating and stationary components' interface and the component-to-component transition interface in a high pressure gas turbine exist in the form of gaps. They are necessary for providing clearance and to allow for the thermal expansion caused by the high temperature of the hot core gas. To prevent the ingression of the mainstream gas into these interfacial gaps, relatively cooler fluid is bled from the later stages of the compressor to seal them. These cooling flows are often cited in the literature as 'leakage' flows or in case of a stator-rotor disc cavity as 'purge' flow (Figure 2-6). They interact with the mainstream flow and influence (or are influenced by) the secondary flows. The leakage flow acts as the coolant in the current study performed, therefore it is essential to review the existing knowledge on the subject. The influence of the leakage flow on the endwall

heat transfer combined with the effect of endwall contouring on the film cooling effectiveness have been of great interest lately and a wealth of literature is available on the topic. Presented here are some of the recent findings.

Haselbach and Schiffer [1] performed a study where the cooling flow is introduced through a slot ahead of a vane row with various pitch, swirl angles and blowing rates. Lynch and Thole [2] measured the heat transfer coefficients along a first stage vane endwall with upstream leakage flow through a simulated combustor-stator interface slot. Leakage flow with higher mass flux increased the film cooling effectiveness immediately downstream of the slot but had a very slight effect elsewhere in the vane passage. It was observed that the high heat transfer in the vane passage throat region had low film cooling effectiveness, indicating that the part would be likely to experience high metal temperatures and large thermal stresses at that location. In another study by Thrift et al. [41], the effect of varying the combustor-turbine interface slot orientation and position on the vane endwall film cooling effectiveness was investigated. They evaluated the effectiveness values for two slot orientations 90˚ and 45˚ at various mass flux ratios along with time resolved digital particle image velocimetry measurements capturing the flow field in the leading edge. As shown in Figure 2-7, the slot angled at 45˚ yields much better coolant coverage than the 90˚ slot angle. The coolant ejecting out the 45˚ slot angle tends to attach to the surface much more efficiently than the other case of 90˚ where the ejected fluid shoots into the main flow thus losing its cooling value. Although it was expected that the leakage flow through 45˚ would yield better coolant coverage than the 90˚ angle oriented slot. The important outcome of their study was the drastic differences in the horseshoe vortex formation for the various cases. The case of 90˚ angled slot caused the coolant flow to be ejected right into the main flow resulting in the separation of the incoming boundary layer

and the subsequent formation of a large leading edge horseshoe vortex. Coolant ejected from the slot was turned back down toward the endwall and beneath the vortex due to the pressure gradient caused by the stagnation of the incoming boundary. The PIV measurements indicated some unsteadiness in the position of the vortex center. There also have been studies where leakage flow alone was not effective in providing desirable coolant coverage. For example, Thole and Knost [42] measured the endwall adiabatic effectiveness values for a nozzle vane passage with upstream slot cooling and film cooling holes in the endwall. With the cooling slot alone, it was found that many regions around the vane were devoid of any coolant. The coolant seemed to be exiting the slot in a non-uniform manner most of it through the mid-passage between the vanes. The streamlines showed stronger turning towards the suction surface with increasing flow rates due to the existing crossflows resulting in such a behavior. With combined hole and slot film cooling, the coverage was enhanced. This points to an important conclusion that leakage flow can be expected to provide a desirable coverage over the endwall in the presence of supporting factors, as is shown by the following studies.

Several studies have been performed with the contoured endwall in the presence of leakage flows to explore their combined effect. Generally, the contoured endwall serves

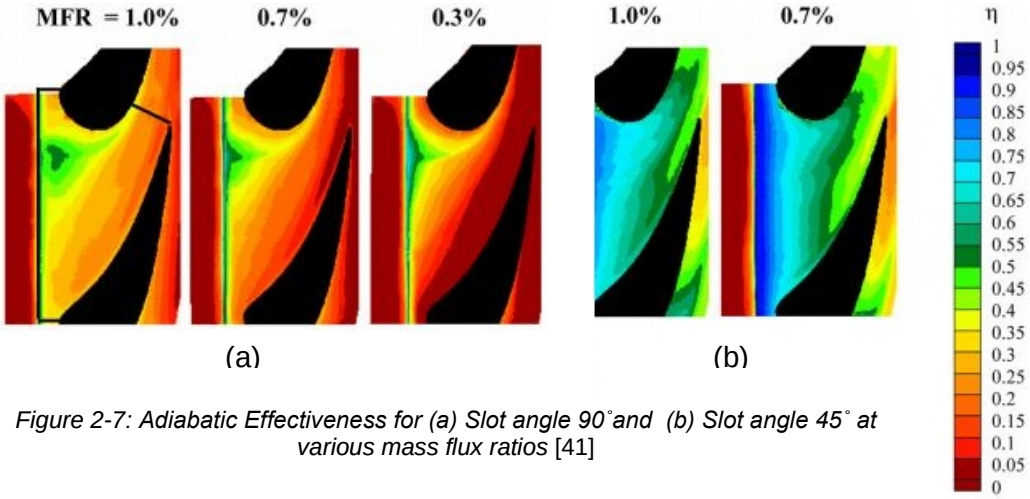

Figure 2-7: Adiabatic Effectiveness for (a) Slot angle 90˚and (b) Slot angle 45˚ at various mass flux ratios [41]

to provide streamwise acceleration to the flow by reducing the passage width. This in turns leads to the thinning of the boundary layer of the approach flow and hence weakens the resultant secondary flow structures. Also, in some cases, depending upon the design of the endwall, the contouring of the endwall contributes by reducing the coolant ejection angle enabling the coolant to remain closer to the surface that is to be cooled. The effect of an axisymmetric contoured endwall on a nozzle guide vane endwall adiabatic effectiveness was investigated by Thrift et al. [43] in the presence of leakage flow and film cooling holes. Figure 2-8 shows the results for three endwall configurations at different blowing ratios of the leakage flow. The contoured endwall provided better coolant coverage, especially in the leading edge region where the endwall is contoured. However, the effect was insignificant in the downstream locations where the endwall was essentially flat. High resolution experiments were conducted on a symmetric airfoil linear cascade by Laveau et al. [44] to compare the heat transfer coefficient distributions offlat and contoured endwalls. The contoured endwall case showed an increase of up to 25% in the heat transfer coefficient values in the leading edge region by weakening the horseshoe vortex forming in the region. Subsequently, the downstream portions also experienced enhanced heat transfer coefficient. An aerodynamic efficiency comparison study of two different non-axisymmetric endwall contouring and a baseline axisymmetric contouring case for a one-and-a-half stage axial turbine was performed by Schuepbach et al. [45]. It was shown that the rotor dominates the static pressure field at the rim seal exit when the purge flow is present. The purge flow shoots out as jets near the blade suction side corner. The strength of the jet is influenced by the first vane pressure field. A circumferential component of vorticity is created as the jets enter the rotor passage with a subsequent formation of a streamwise vortex component as the injected fluid turns around the rotor leading edge. The different endwall designs redistributed the pressure field in different manners thus

causing differences in the associated aerodynamic losses. It draws a key conclusion that "it is important to consider the influence of purge flow when designing endwalls. If not, it can happen that most of the improvements due to the profiling are lost when the purge flow is present".

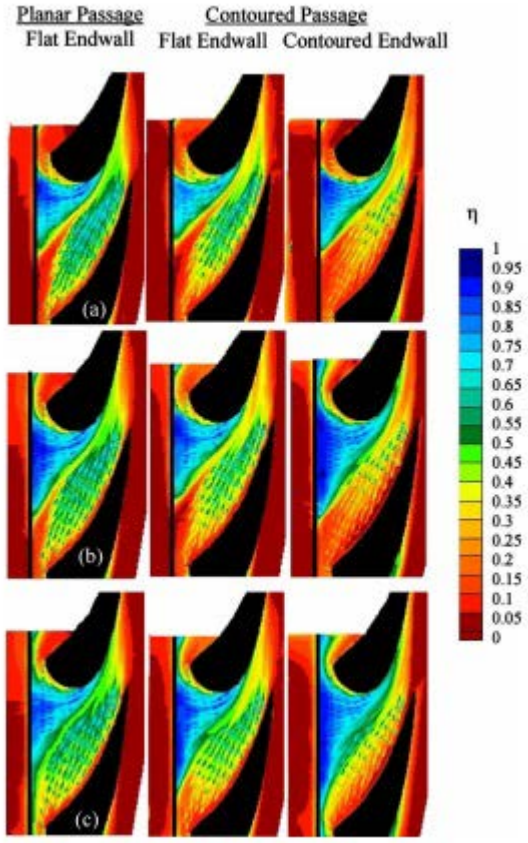

Figure 2-8: Comparison of adiabatic effectiveness contours for different endwall configurations for (a) 0.3% leakage flow (b) 0.5% leakage flow, and (c) 0.7% leakage flow [43]

A computational study comparing adiabatic effectiveness of two different axisymmetric endwall contour shapes in a high pressure turbine rotor stage cascade was performed by Simon and Erickson [46]. One endwall contour ('dolphin nose') is present in the vicinity of leading edge region and the other ('shark nose') extends further down into the passage. It was shown that for the dolphin nose endwall shape, the pressure redistribution due to the decreasing passage area and consequently the thinning of the approach flow boundary layer weakened the secondary flow structures in the leading edge and upstream

portions of the passage. The ‘shark nose’ endwall shape, on the other hand, had a less significant but more sustained effect on improvement of the adiabatic effectiveness values.

Several studies aim to address the utility of combustor liner coolant effect in the flow approaching the high pressure turbine stage. One such study by Seah et al. [3] examines this effect in a first stage rotor passage with axisymmetric endwall contouring and the thick engine representative temperature profile. The leakage flow is injected at mass flow ratios of 0.5%, 1.0% and 1.5%. The cases with the thick temperature profiles of the approach flow showed appreciable augmentation of the passage thermal fields over cases with the thinner approach flow temperature profiles, as can be seen in Figure 2-9. These measurements are helpful to a gas turbine designer in designing the combustor with the endwall heat loading in consideration. Also, this study investigated the extent to which the blowing ratio of the coolant to the mainstream flow can augment the endwall adiabatic effectiveness. Figure 2-10 shows the measured contours of adiabatic effectiveness with three mass flow ratios. It was concluded from the study that the higher blowing rate of the coolant enables the fluid with sufficient momentum to overcome the strong secondary flows and hence much better coverage is obtained over the endwall. Some other related studies were conducted by Kristina et al. [47] and Barringer et el. [48].

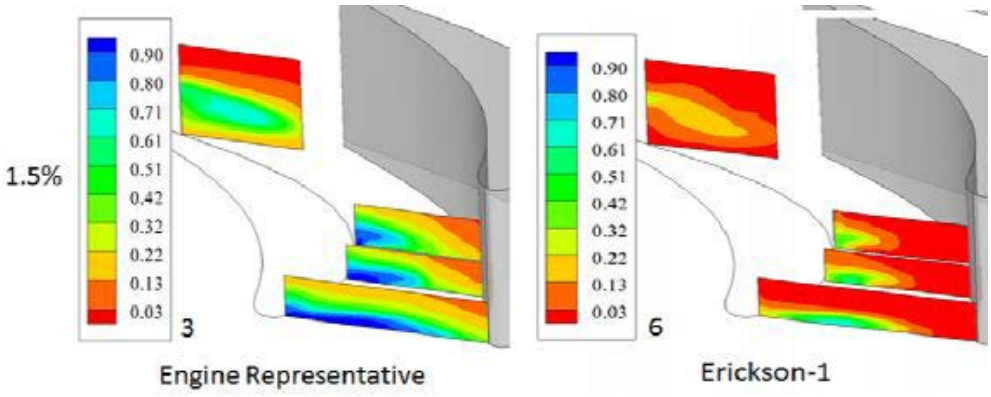

Figure 2-9: Passage thermal fields for coolant mass flow ratio of 1.5%. (Left) Engine representative inlet temperature profile, (Right) Erickson-1 (thin inlet temperature profile) [3]

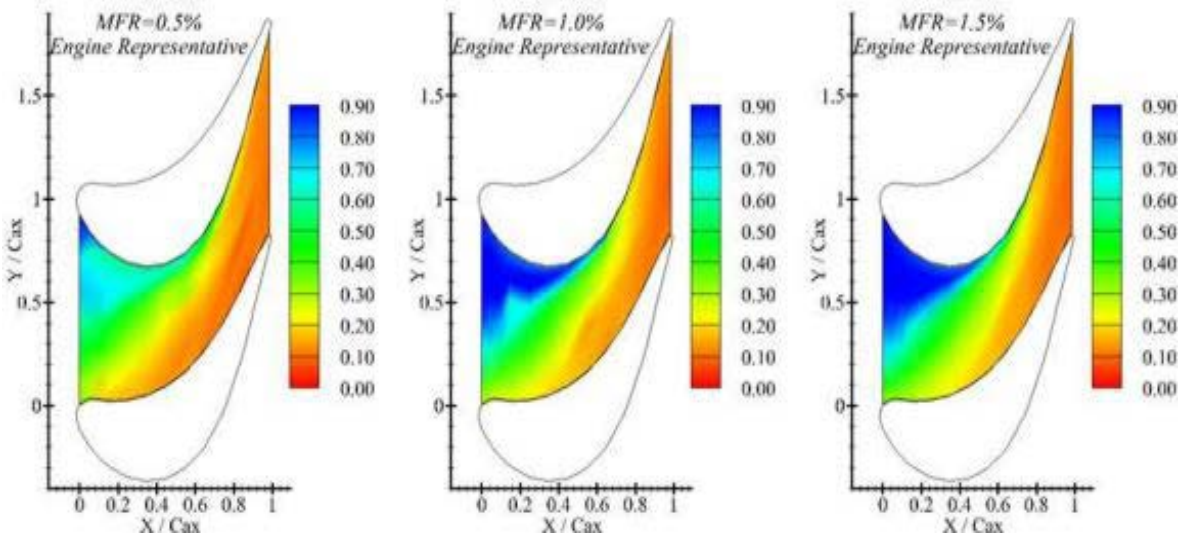

Figure 2-10: Adiabatic effectiveness contours [3]

Most of the studies discussed above were performed on stationary cascades. Suryanarayanan et al. [49] examined the effects of rotation on the platform film cooling effectiveness by conducting a study on a three-stage turbine research facility. The secondary flow from the blade pressure surface to the suction surface was found to be strongly affected by the rotational motion that resulted in different film cooling effectiveness distributions at different rotational speeds and blowing ratios.

Effect of the Leading Edge Vortex Modification

As discussed in the preceding sections, the leading edge region of the high pressure rotor and stator stages experiences very low film cooling effectiveness due to the formation of a strong horseshoe vortex in this region, and other corner vortices. Several studies have been conducted to develop methods to control the secondary flows in the leading edge region. One such study by Thrift and Thole [50] explores the effects of various slot injection angles at different momentum flux ratios on the size and location of the horseshoe vortex. Associating the effect of the momentum flux of the injected flow with its turbulence levels

and the shearing within the boundary layer for cases of different slot angles, the endwall heat transfer is examined. In another approach to modify the horseshoe vortex, Zhang et al. [51] used three different leading edge fillet profiles placed at the airfoil leading edge and endwall junction. The different fillet shapes weaken or strengthen the horseshoe vortex and thus dictate, to some extent, the manner in which the secondary flow structures would further develop into the passage.

Effect of Passage Flow to Coolant Flow Density Ratio

In real engines, the density of the coolant introduced into the turbine passage is higher than that of the mainstream gases (usually twice the density of the mainstream gases) due to the higher pressure and lower temperature of the fluid. Several studies have been performed to study the effect of passage to coolant density ratio on the film cooling effectiveness of the coolant over the endwall. Salcudean et al. [52] examined these effects on a symmetric airfoil model in the presence of single row and double row injection focusing on the heat transfer near the leading edge region. They used CO_2 to create the density ratio of 2. In another similar study by Ekkad et al. [53], measurements for the Nusselt number and film cooling effectiveness were taken and compared with the baseline case of density ratio of 1. The film cooling effectiveness seemed to be sensitive to the density ratio. At a given blowing ratio, the case with lower density ratio yielded higher effectiveness values indicating that the denser coolant fluid with its lesser momentum flux fails to be as effective as the lighter coolant fluid with higher momentum. It is important to consider the role that the density ratio can play in determining the coverage of the coolant over the endwall especially while interpreting the data taken in an experimental cascade with passage density the same as the coolant density.

Chapter 3 Experimental Test Facility

The design and development of the main features and components of the stator test facility are discussed in this chapter. These include the wind tunnel for supplying the conditioned flow to the test section, the test section, which includes the nozzle/stator guide vanes and the upstream coolant slots, the exit flow management by diffuser and tailboards, and the methods to access the test section to take measurements. A complete view of the test facility is shown in Figure 3-1.

The details of the main features of the rotor cascade test facility are given in the Appendix.

1: Intake System (intake header and main centrifugal fan)
2: Base Wind Tunnel
3. Turbulence generator
4. Contraction nozzle
5. Test Section (upstream slots, stator blades/vanes)
6. Diffuser

Figure 3-1: Complete view of the test facility with intake system at the inlet and diffuser at the exit

3.1. Wind Tunnel

The flow entering the test section which includes the airfoil cascade along with the upstream coolant slots must have characteristics that are essential to make the test facility

engine representative. Therefore, the open return type wind tunnel facility is designed to deliver subsonic flow with desirable turbulence characteristics and chord Reynolds number. This flow supply section includes three main components that include the main and the auxiliary fans, the turbulence generator and the contraction nozzle. Modifications were done on some of the pre-existing components of the wind tunnel, adapted from Erickson [54], to make them suitable for the current study. The details of each component are discussed in the following sections.

3.1.1. Fans

3.1.1.1. Main Fans

The supply air from the room for the study is derived through a large intake header with several air filters at the beginning of the wind tunnel. A general purpose, centrifugal fan (3.7kW, 5HP) made by the New York Blower Company is used to draw in the room air through the series of air filters. The pressurized air from the centrifugal fan is then passed through a 90˚ turning header to align the flow with the axis of the base wind tunnel built by Engineering Laboratory Design, Inc.

Installed at the beginning of the base wind tunnel is a 5.6kW (7.5HP) axial flow fan made by the Joy Manufacturing Company. The axial fan is used to drive the air delivered by the centrifugal fan forward into the tunnel towards the downstream sections. The axial fan is controlled by a motor speed controller which is used to control the rotational speed of the fan by varying the operating frequency between 0-60Hz at 0.1Hz increments. Followed by the axial fan is a radial-to-square fiberglass transition section. This is connected to an air cooled heat exchanger that is not used in the current study. It only serves to remove large scale vorticity and rotation effects created by the axial fan. The flow then gets transferred to a settling chamber upstream of the turbulence generator discussed in Section 3.1.2.

3.1.1.2. Auxiliary Turbulence Generator Flow

Flow is introduced to the turbulence generation chamber from all four sides by means of two identical turbulence generator fans, as shown in Figure 3-2. These are 3.7KW (5HP) centrifugal blowers (Model 4C330) made by the Dayton Electric Manufacturing Company. The intake flow from these fans is delivered to a flow distribution cabinet whose dimensions are 2.32 m X 0.42 m X 0.43 m (7.62 ft X 1.38 ft X 1.42 ft), as designed by Erickson [54]. The connection from the exit of this section to the sides of the turbulence generator is made by 25.4 cm (10 in.) ducts. The 90˚ turning elbows deliver the flow from top and bottom of the turbulence generator as shown in Figure 3-2. These ducts and elbows are fitted with honeycomb straighteners to reduce the swirling effects that may have been caused by the manner in which the flow is being introduced to the passage.

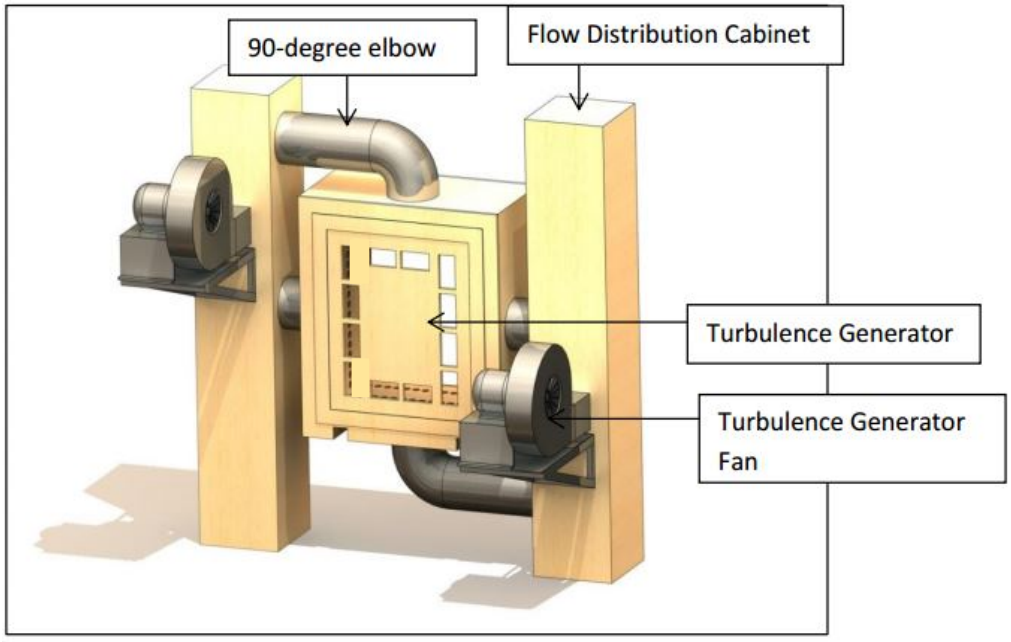

Figure 3-2: Auxiliary flow supply to the Turbulence Generator (adapted from Erickson [54]*)*

3.1.1.3. Leakage Slot Flow

This section discusses the supply system of the leakage flow to the plenum which then delivers the flow to the test section through a slot. The geometrical details of the leakage flow plenum are discussed in detail in Section 3.3. The following description is summarized from previous work by Erickson[54]. The leakage flow consists of the room air which is drawn in by 1.5kW (2HP) centrifugal blowers (Model HPB) made by the Cincinnati Fan and Ventilator Company Inc. The rotational speed of the fan is controlled by MagneTek GPD333 motor controller which is based on pulse width modulation methodology. The connection between the fan exit and the entrance of the chamber that supplies flow to the leakage plenum is made by a series of PVC pipes. At the exit of the fan is a PVC flange and a 38 cm (15 in.) section of schedule 40 straight pipe. Connected to this straight pipe is a 10 cm (4 in.) diameter piping. In order to get a uniform flow out of the pipe, it is packed with approximately 500 small straws (3 mm I.D.) acting as flow straighteners. Before the flow enters the flow rate measurement device installed within the pipeline, the flow is allowed to develop in terms of its hydrodynamic and thermal profiles. This is ensured by installing at the exit of the 10 cm pipe, a long straight pipe of L/D of 14.25.

As mentioned above, the flow now enters Meriam Instrument's 'Laminar Flow Element' (LFE) which enables the measurement of volumetric flow rate which is needed later for establishing the desired mass flow rate of leakage with respect to the mainstream flow. The working principle of the flow meter is discussed in detail in Section 4.5. The LFE has two ports (one at exit and another at the inlet) that are connected to an inclined manometer (see Section 4.3.2) using equal lengths of Tygon tubing. This gives the differential pressure reading that can then be related to the flow rate through the LFE and hence the flow rate of the leakage. Downstream of the LFE is another section of straight PVC pipe with an L/D ratio of 12. The manufacturing company of the LFE, Meriam Instrument,

recommends the length of the straight pipe section of a minimum of 10 diameters upstream and 5 diameters downstream. At the exit of this pipe section is a round-to-square transition duct followed by a 90˚ elbow for directing the flow into the chamber that leads to the leakage flow supply plenum. The chamber has heating elements for raising the temperature of the leakage flow. Typically, for the current study, the leakage flow is heated 7-8˚ C above the mainstream flow by using the heaters at 85% of their maximum capacity.

3.1.1.4. Temperature Control Slot Flow

One of the important conditions of the approach flow to the test section is that it must simulate the effect of the combustor coolant in the approach flow of an actual high pressure gas turbine. In the current study, this is achieved by creating a temperature profile in the approach flow to the test section. Therefore, an inlet thermal profile generation apparatus is designed, which is discussed in detail in Section 3.4. The following description is summarized from previous work by Erickson[54]. This section discusses the components that generate the required flow for the purpose. The supply flow is provided by a 1.5kW (2HP) centrifugal blower (Model HPB) made by Cincinnati Fan and Ventilator Company Inc. It is similar to the centrifugal blower used to deliver the flow to the leakage flow generation apparatus as discussed in the preceding section. A MagneTek GPD333 motor controller drive is used to vary the fan's rotational speed by changing the operating frequency in the range 0-60 Hz at 0.1 Hz increments. The exit of the fan and the inlet of the thermal profile generation apparatus are connected by means of 2.3 m (7.5 ft) of 10 cm (4 in.) diameter Class B gas vent piping. To heat the flow to create the required temperature profile within the test section, a total of 8 heating elements that are capable of providing heating power up to 2.8kW, are installed within the connecting pipe. The flow from the pipe exits into a header, which turns and redistributes the flow. To further distribute the flow uniformly before it enters the aforementioned thermal profile generation

apparatus, a fine screen is placed at the exit of the header. The flow now exits into the acrylic apparatus that finally delivers the flow into the main test section.

3.1.2. Turbulence Generator

The flow exiting the low NO_X combustor of an actual gas turbine is characterized by high turbulence intensity levels and large eddy length scales. It has been found from several studies that the high free stream turbulence can have a significant impact on endwall heat transfer [29], [30] . Therefore it is important to simulate this effect in the current study also. The "turbulence generator," as the name suggests, is used to achieve this objective. It can loosely be thought of as a "combustor simulator" creating the desired turbulence characteristics within the approach flow to the test section. It should be noted here that the turbulence generator is not an experimental simulation of any specific combustor design, but merely an apparatus for creating turbulence characteristics similar to those of the exit flow from a typical combustor of an industrial gas turbine. The turbulence generator used in the current study has been modified from its previous design (Refer to Erickson [54]) to satisfy the requirement of the higher inlet velocity of the new test facility. The recommendations of Ames [55], Chung [56] and Wang [57] were considered to design the turbulence generator.

The turbulence generator consists of essentially a large mixing volume with two separate flows in the form of jets, namely the "core flow jets" and "cross flow jets," shooting into the mixing chamber through several holes on its top, bottom, side and front walls. The dimensions of the mixing volume are 64.5 cm X 91.4 cm X 53.3 cm (25 in X 36 in X 21 in). The source of the core flow, which is essentially the main flow, has been discussed in Section 3.1.1.1. The core flow encounters a blockage in form of the front face of the turbulence generator as seen in Figure 3-3. The front face has large rectangular slot

openings that aim to generate large eddies within the flow. Inside the mixing zone, the second type of flow (cross flow) is introduced by means of the 90˚ elbows and straight ducts as discussed in Section 3.1.1.2. The cross flow is delivered into the turbulence generator through circular holes as shown in Figure 3-5. The circular jets created by these holes are oriented normal to the streamwise direction causing strong interaction between the core flow jets and cross flow jets. This results in the production of shear, which transfers the kinetic energy from the mean flow into the turbulent fluctuating flow. The size of the slots and holes are important since they determine the length scales of large turbulent eddies formed in the resulting flow. The following sections discuss, in detail, the design of the various components of the turbulence generator.

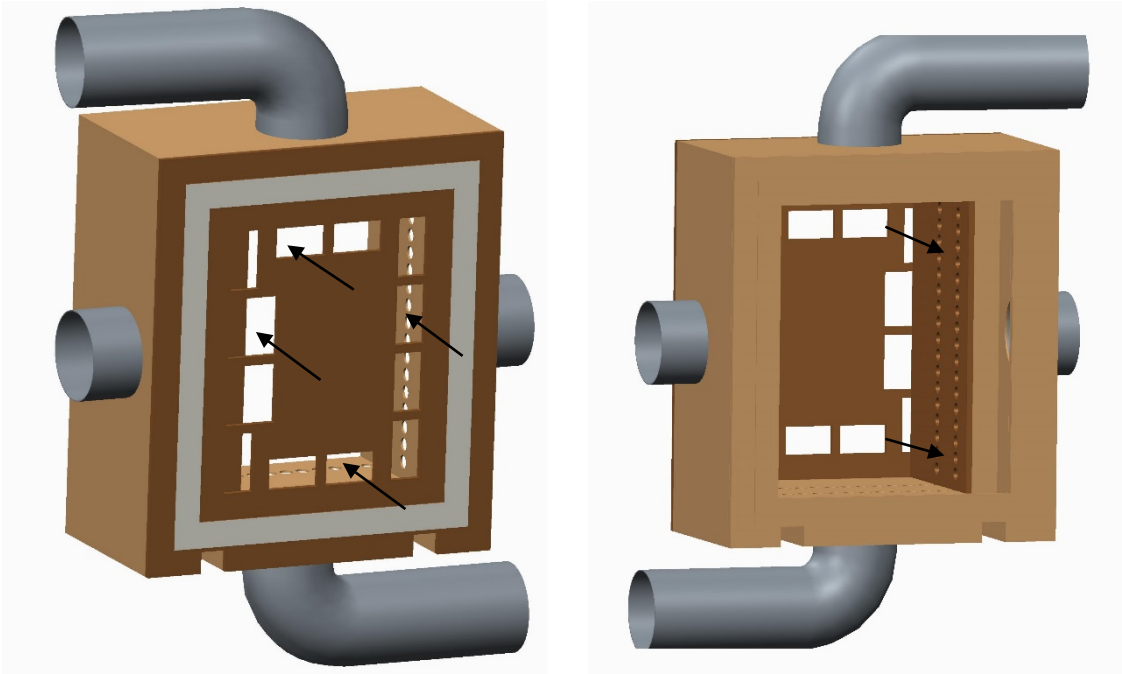

Figure 3-3: Turbulence Generator showing (Left) Front face and (Right) Back face; arrows depict the direction of mainstream core flow from base wind tunnel into the turbulence generator;

3.1.2.1. Core Flow

Jets are created in the main flow as it passes through the front face of the turbulence generator. The slot sizes used depend on whether they are oriented vertically or

horizontally. Detailed dimensions are given in Figure 3-4. Adapted from the original design (Erickson, [54]), are a set of six vertically oriented slots (numbered 2, 3, 5, 6, 7 & 8) with dimensions 17.2 cm X 8.9 cm (6.75 in X 3.5 in), a set of two other vertically oriented slots (numbered 1 & 4) with dimensions 17.2 cm X 2.7 cm (6.75 in X 1.1 in) and all the horizontally oriented slots (numbered 9, 10, 11, 12), with dimensions 15.2 cm X 8.9 cm (6 in X 3.5 in). It is expected that the largest eddy length scale will be of the order of these slot sizes. The spacing between the neighboring slots is 2.5 cm (1 in). The two different sets of vertically oriented slot sizes result from the physical limitations on adapting the previous design to the requirements for the new test facility. As will be discussed in Section 3.2, the airfoil inlet span (or width) for the current study is smaller than the previous generation (Erickson, [54]) of airfoils in the test facility (50.6 cm, 19.92 inches, then as compared to 33.72 cm, 13.28 inches now). This requires the test section inlet width to match the airfoil inlet span to maintain continuity in the flow without any steps in the walls of the test section. As compared to the previous test facility, with the inlet section width reduced and assuming the same mass flow rate of the main flow being drawn in by the wind tunnel discussed in previous sections, the inlet velocity is expected to be higher. This will ensure that the Reynolds number for the study is sufficiently high (expected approximately 400,000). The assumption of approximately the same mass flow rate in the new test facility as compared to the previous facility is justified by the following reasons. Firstly, a major factor that may be expected to affect the mass flow rate through the system is the resistance to the flow caused by the turbulence generator. But with the design remaining similar to the previous facility it is expected that the resistance levels will be the same. Secondly, efficient diffusion of the exit flow into the atmosphere is essential. It is accomplished by designing a new diffuser for the facility, details of which will be discussed in Section 3.5. Therefore, the existing turbulence generator is modified in such a manner

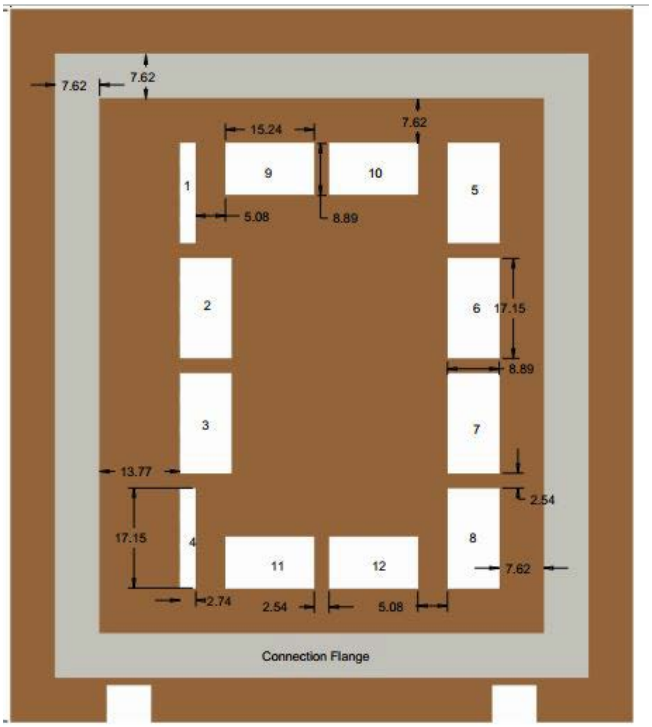

Figure 3-4: Detailed dimensions of core flow slots in centimeters.

that the exit width of the turbulence generator matches the inlet width of the test section with the contraction nozzle serving as the connection. The slot area on the front face of the turbulence generator, representing the open area for flow to pass through, equals approximately 1617 cm^2 (250 in^2).

3.1.2.2. Cross Flow

Entering from the top, bottom and sides walls of the turbulence generator are the cross flow jets in a direction that is normal to the core flow jets discussed above. The region with high shear is created which is the source for continuous turbulence generation throughout the life of the experiment. As shown in Figure 3-5, the holes on the top wall correspond symmetrically to the holes on the bottom wall and the holes on the side walls also are symmetric about the plane passing along the centerline of the tunnel and in the direction of the main flow. Adapted from the original design, each hole has a diameter of 3.8 cm (1.5 in) with the spacing between holes being 5 cm (2 in). The total area opening of the

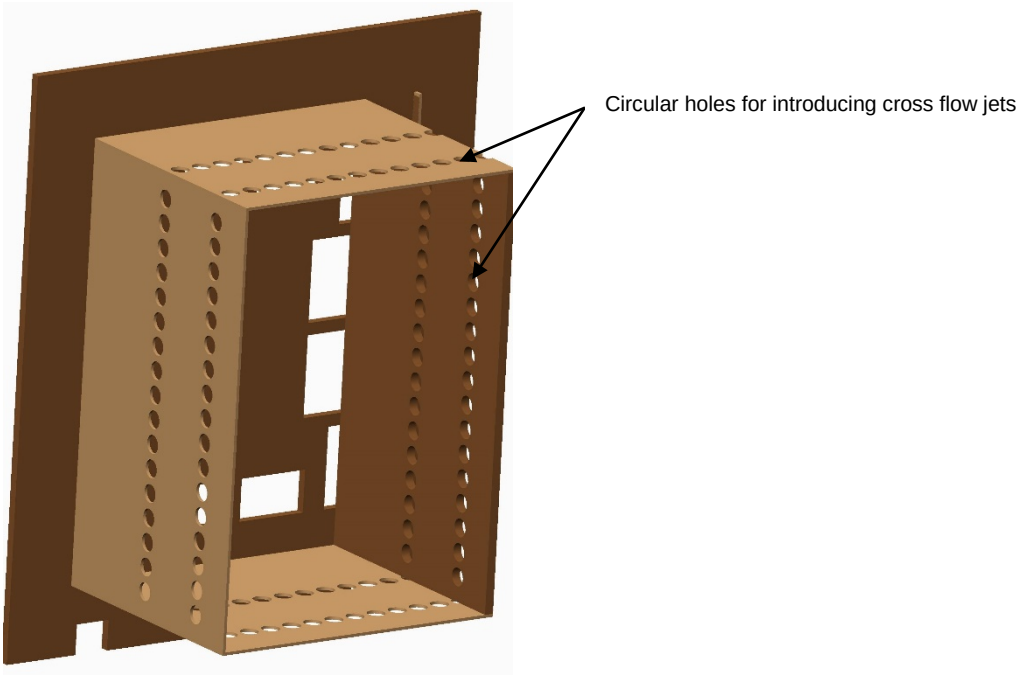

Figure 3-5: Circular holes on top, bottom and side walls to introduce cross flow jets into the mixing volume

holes is approximately 1340 cm^2 (207 in^2). This arrangement of the holes ensures that the flow within the mixing zone derives its energy (source for the turbulent kinetic energy) in a symmetric manner, although once the cross flow and core flow jets mix and create high levels of turbulence intensity, the directional identities are lost. This further justifies modification of the turbulence generator with asymmetric placement of the two vertically oriented rectangular holes on the front face of the turbulence generator.

3.1.3. Contraction Nozzle

The contraction nozzle connects the downstream section of the turbulence generator to inlet of the test section. It serves two purposes, one to provide the flow area contraction between wind tunnel and the test section; and the second, making the streamlines aligned so that a more uniform velocity distribution is obtained at the exit of the nozzle (or the entrance of the test section). The nozzle is made of 13 gage (2.3 mm/0.09 in. thickness) 304 stainless steel. The area ratio of contraction (from nozzle inlet to nozzle exit) is 2:1.

The contours are designed by Erickson [54] using regression analysis technique. Modification to the previous nozzle design has been done in order to match the reduced width of the test section and the turbulence generator. Figure 3-6 shows the acrylic (transparent, marked with arrow in the figure) insertion made for the purpose. It is held secure by means of laser-cut wooden ribs (each 0.5 in. thick). The vaporization technique based laser cutting machine in the Mechanical Engineering Student Shop allows for precise and fast machining of the ribs. The shape of the rib is designed to be same as the side contour of the nozzle so that the symmetry about the centerline axis is maintained. It can noted from the figure that the width of the exit section is 14.50 inch which matches with the passage inlet width of 14.50 inches (also shown in Figure 3-13). It is expected that the size of the largest recirculation zone or eddy is of the order of core flow slot size in the turbulence generator. Since the flow, as it flows past the contraction nozzle, is accelerated, it causes the vortices within the turbulent flow to undergo a stretching mechanism.

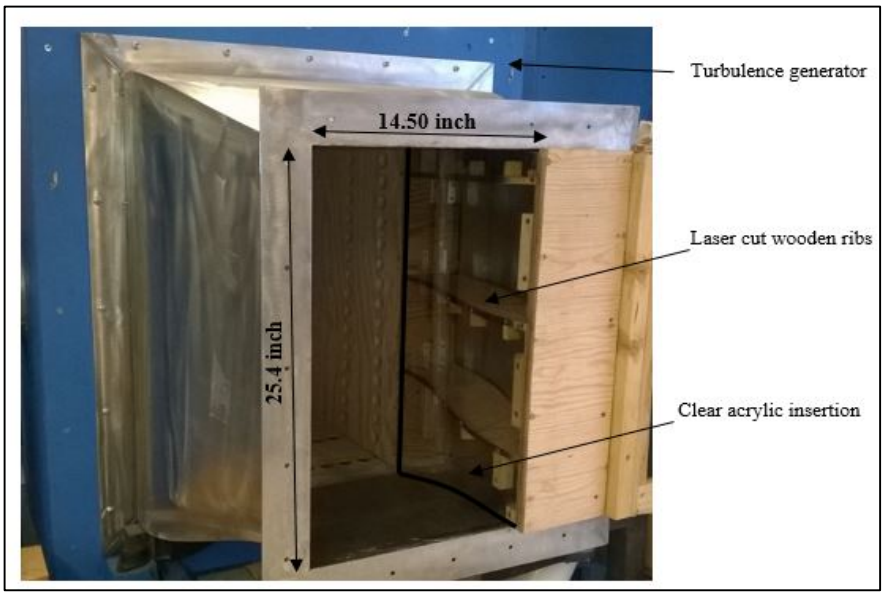

Figure 3-6: Contraction nozzle (Note: For better viewing, the clear acrylic insertion boundary has been marked with a black boundary)

3.2. Stator/Nozzle Guide Vane Simulator

The preceding sections in this chapter have discussed the major components of the test facility that are located before the test section and are used to deliver properly conditioned flow to it. The test section is composed of a scaled up version of stator/nozzle blades and contoured endwall representing the passage of a modern, mid-sized gas turbine engine. It is essentially a two passage linear cascade containing three stator blades, axisymmetric contoured endwall, a flat endwall, an upstream leakage slot and an approach flow temperature control slot. Although more blades are preferred to form a cascade that better addresses the periodicity condition of an actual gas turbine, given the high Reynolds number requirement, this test facility must be composed of three blades (two passages only, hence the larger pitch) which is considered satisfactory for the present purpose.

This section discusses the details of blade and contoured endwall shape, and the manufacturing methods adopted. All the components were designed using Creo Parametric 2.0 CAD software. The machinists in the Mechanical Engineering Research Shop used these drawings as guides to manufacture the various critical test section components (blades and endwall). The other parts were machined in the Mechanical Engineering Student Shop.

3.2.1. Stator Vanes

The profile shape for the blades (or vanes) is provided by Solar Turbines Inc. and represents the blade of a first stage high pressure gas turbine stator (or nozzle). They are scaled up by a factor of 4.9 from their actual engine size for the purpose of experimentation. The material used for manufacturing is acrylic plastic (registered brand name of Plexiglas®, scientific name Polymethyl methacrylate). It is chosen for its shatter resistant and lightweight characteristics. Its good machinability makes it appropriate for

the use with CNC (computer numerical control) vertical and horizontal milling machines. It has a low thermal conductivity of around 0.19 W/mK [58] at room temperature which further makes it a suitable choice since the adiabatic conditions on the surface of blades and endwall must be maintained in the experiment.

Acrylic plastic is readily available in slabs/sheets of standard sizes (0.25 in, 0.5 in and so on). Therefore procuring it in the form of sheets is considered a feasible and an economically viable option. Before use, these are surveyed manually for any burrs or abnormalities with appropriate action taken by making all the surfaces of each slab smooth and level. Using the Mastercam software and the designs delivered to the research shop machinists in the form of CAD models, each slab of acrylic is machined into the desired profile as shown in Figure 3-7 using the CNC vertical milling machine.

Since the design of the static pressure taps is built into the blade design, before clamping the slabs together, a number of holes each of diameter 0.1875 in. (0.476 cm) are drilled all along the slab boundary to allow for the connection to be made to the pressure tap by means of Tygon plastic tubing of outer diameter 0.1875 in. (0.476 cm) and thickness 1/16th in. (0.158 cm). The details of pressure tap design are provided in the next section. Since the measurement of the static pressure only at the mid-span of the blade is of interest, these holes are present only on the set of slabs that are located up to the mid-span, as circled in the figure. In the end, the slabs are stacked together and clamped with sufficient force by means of five 1/2 in. threaded steel rods. The nuts on the ends are tightened to keep the slabs under compression. The clear Tygon pressure tubing that is used to complete the connection from the static pressure tap to the pressure measurement device is shown in Figure 3-7. After clamping them together, a final step of sanding the surface of the blade is performed to remove any improperly levelled slab or machining burrs.

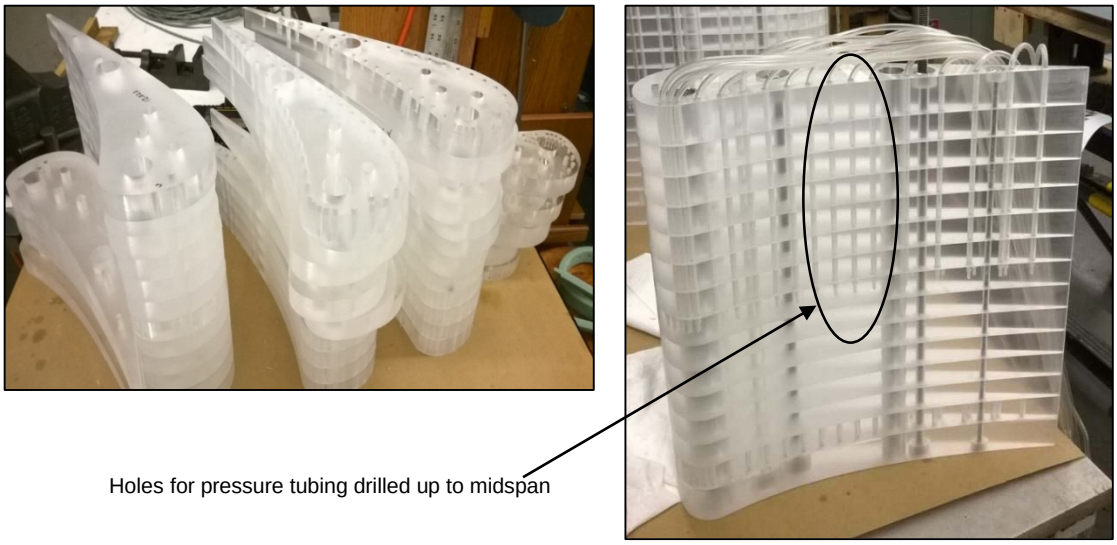

Figure 3-7: (Left) Slabs of acrylic machined into desired blade profile; (Right) All slabs stacked together using the compression force of steel threaded rods

3.2.1.1. Cascade Layout

Using the same methods as discussed above, a total of three blades are manufactured. The detailed dimensions are given in Table 3-1. They are laid out in such a manner that the approach flow (or the main flow) is perpendicular to the leading edge plane of the blades as shown in Figure 3-8. This is important because the cascade represents the first stage *stator* of a gas turbine where the exit flow from the combustor enters the turbine passage perpendicular to the leading edge plane of the blades from where it is then guided towards the rotor stage. To make the cascade in the test facility representative of this condition, the layout is set up in this manner. The blades are highly loaded with the flow experiencing high acceleration and turning in the middle section of the passage. The blades have a low aspect ratio with strong secondary flows that can have a significant effect on the endwall heat transfer making the study of endwall cooling further important. The cascade is a scaled up version of actual engine size with a scaling factor of 4.9. The scaling factor is determined by finding the ratio between the actual engine turbine passage

pitch and the existing experimental cascade pitch. To be noted here is that the inlet span of the blade is different from the exit span due to the presence of a *contoured* endwall. The inlet span was determined such that the associated inlet area satisfies the minimum required value to yield a sufficiently high inlet velocity that corresponds to a high Reynolds number, an essential condition of the experiment. The Reynolds number eventually obtained is discussed in the chapter on “Qualification of Approach Flow” in Section 5.2. The junction at the top wall of the test section and the topmost blade in the cascade contains a small gap that acts as *bleed slot* for the boundary layer of approach flow. In absence of suction of this boundary layer, it becomes difficult to match the mid-span pressure distribution for both passages which in turns violates the periodicity condition of

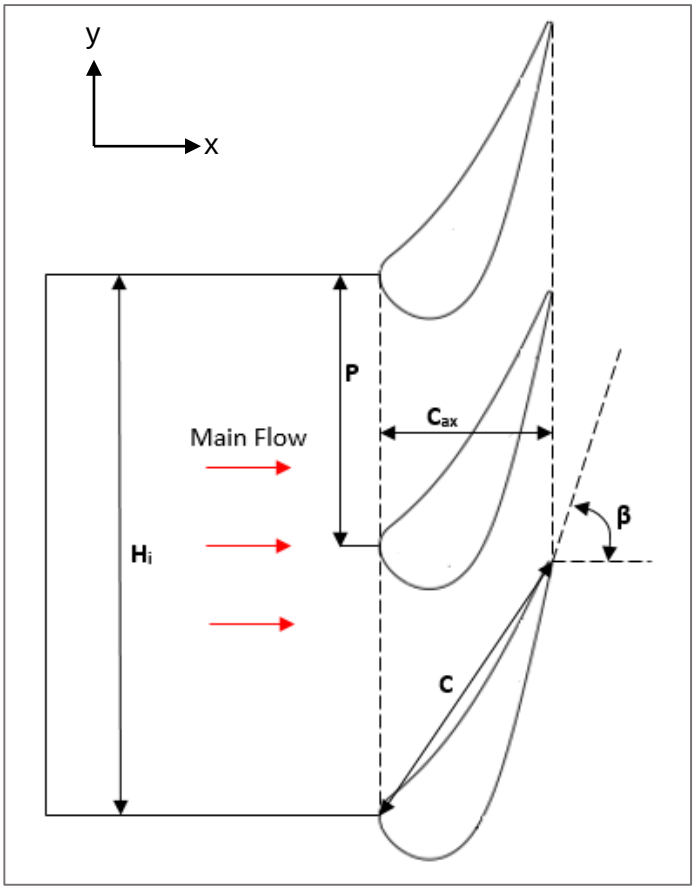

Figure 3-8: Cascade layout

the cascade. It may also result in improper location of stagnation point for the topmost blade.

Table 3-1: Stator Cascade Dimensions

Scale Factor (with respect to actual engine size)	4.91
Blade True Chord Length (C)	36.538 cm (14.385 in)
Blade Axial Chord Length (C_{ax})	20.534 cm (8.084 in)
Cascade Pitch (P)	32.25 cm (12.697 in)
Blade Inlet Span (S_i)	33.72 cm (13.276 in)
Blade Exit Span (S_e)	31.304 cm (12.324 in)
Blade Aspect Ratio, Inlet (S_i/C)	0.922
Blade Aspect Ratio, Outlet (S_e/C)	0.857
Space-Chord ratio (P/C)	0.883
Blade Inlet Angle (α, angle between cascade centerline axis and camber line at leading edge)	0˚
Blade Outlet Angle (β, angle between cascade centerline and camber line at trailing edge)	72.33˚
Inlet Passage Height (H_i)	64.50 cm (25.394 in)
Blade-Endwall fillet radius	0.3 cm (3 mm)

3.2.1.2. Blade Static Pressure Taps

To measure the mid-span static pressure for both the passages, static pressure taps are built into the blades. The measurement of the static pressure is helpful in understanding the extent of acceleration that the passage experiences with the given blade design. Also, by matching the static pressure loss profiles for both the passages, it is ensured that equal amounts of fluid enter each passage. Each tap is square-edged with dimensions of length 0.73 cm (0.29 in) and diameter 0.0508 cm (0.02 in) with L/D ratio of approximately 14 as shown in Figure 3-9. The hole must have its axis aligned perpendicular to the flow direction. This required a methodology that allows to drill such a low diameter hole, especially on the curving shape of the blade. For this purpose, a 3D printed drill jig was

used as shown in the Figure 3-9 to guide the drill bit into the material eliminating the possibility of the slipping of the drill on the surface and misalignment of the axes of the drill bit and the hole. The taps were cleared of any burrs while maintaining the square-edge of the holes. Care was taken in determining the dimensions as well in the manufacturing of the taps based on the recommendations from Shaw [59] and Goldstein [60] to minimize errors in measuring static pressure.

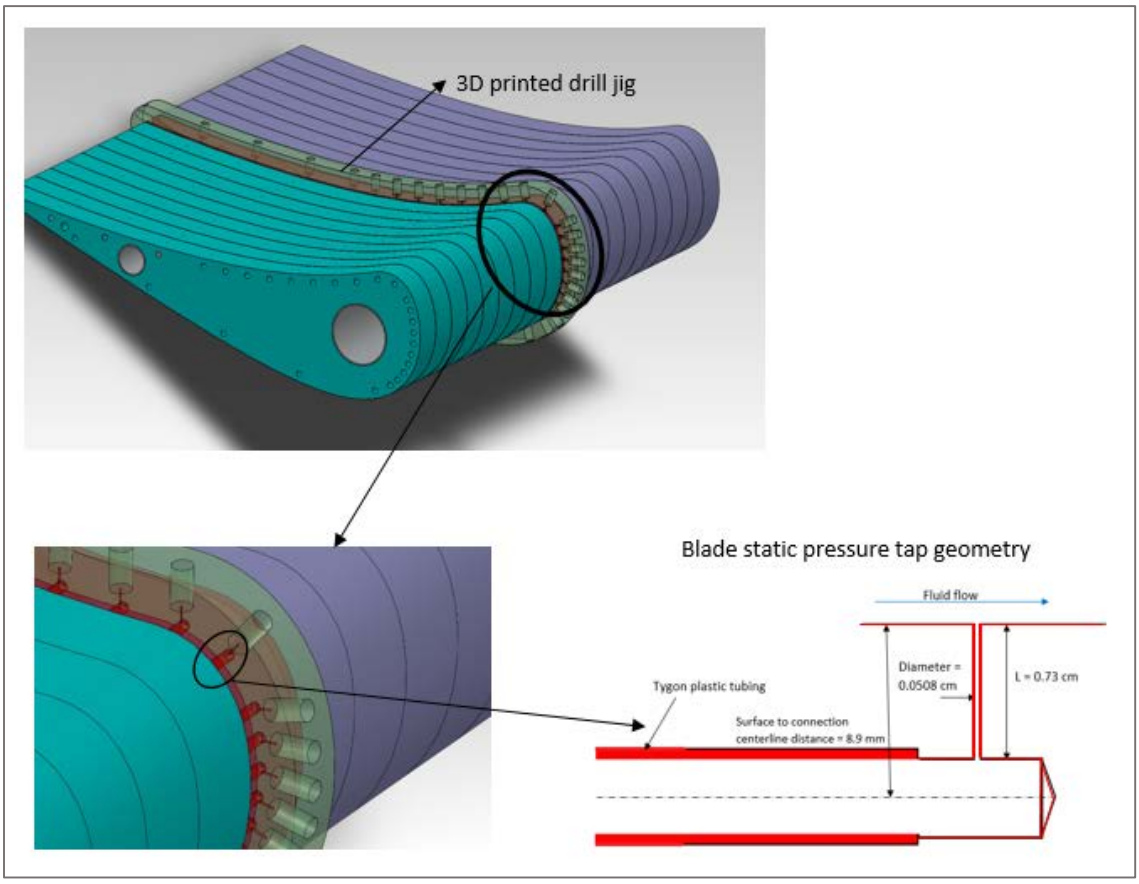

Figure 3-9: Drill jig used for pressure taps on blade surface; detailed geometry of pressure tap

The location of taps is determined such that complete static pressure loss profiles can be measured around the shape of the blade using a total of 38 pressure taps, as shown in Figure 3-10. More taps closer to each other are placed in the leading edge region. They

are more uniformly distributed in the middle zone of high acceleration and then deceleration (changing shape of pressure loss profiles). The trailing edge has relatively fewer taps since it is expected that the pressure profiles in this zone will be relatively flat, thus the spacing between the taps was considered adequate. Tygon plastic tubing is used to complete the connection from the static pressure tap to the pressure measurement device which is two-way pneumatic valve (model TV-2S) made by Clippard Minimatics. A switchboard connecting to the valve having a common line connecting all the pressure measurement locations is used.

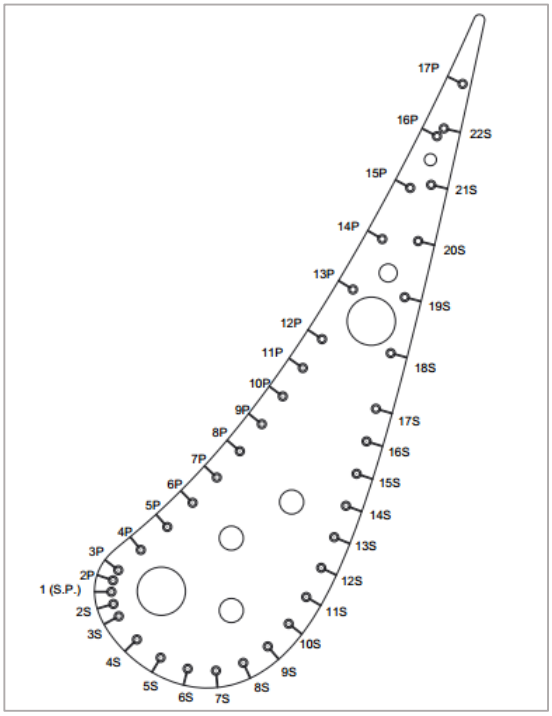

Figure 3-10: Static pressure tap locations; 'P' and 'S' represents pressure side and suction side respectively

3.2.2. Hub Endwall

The hub endwall is the region where the film cooling is being investigated in this study. Therefore it is another very critical component. It is contoured in an axisymmetric manner. The word "axisymmetric" is used in context of the actual turbine which means that the

contour shape of the endwall is symmetric about the axis of the turbine and present only in the axial direction. The endwall contour is provided by Solar Turbines Inc. and is shown in Figure 3-11. The scaling is matched to that of the blade size. The contouring begins upstream (x/C_{ax} = -0.104) of the leading edge and extends throughout the passage and beyond the trailing edge (x/C_{ax} =1.352). It can be seen from the figure that the shape tends to initially decrease the passage width contributing to further acceleration of the flow and then curves back in the downstream regions. The shape results in an unequal inlet and exit span of the passage. The other endwall, which is flat, forms the wall enclosing the other side of the cascade passage. It is made of clear acrylic plastic (1/2 in. thick) and provides access to the test section, therefore measurements are not taken over this endwall.

The material of the endwall is chosen as Medium Density Fiberboard (MDF) due to its good machinability, low cost and low thermal conductivity (0.15 W/mK). The MDF can be procured in form of planks (0.75 in. X 52 in. X 13 in.). The endwalls for both the passages are made in one piece after giving consideration to the assembling ease of the endwall and the blades (endwall-blade assembly is discussed in next section). The CAD model of the endwall with blade profile marked on it is used by the Mastercam software that generates the code to direct the CNC vertical milling machine operation. Three similar planks are bonded together using high strength wood glue and then placed on the milling

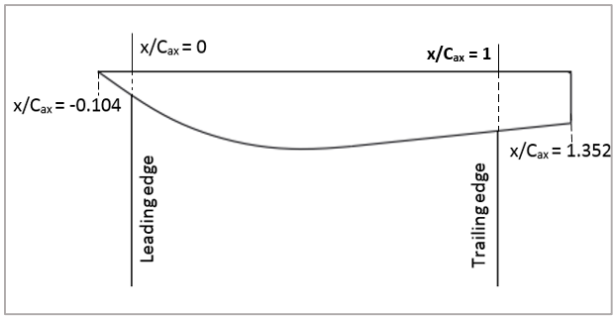

Figure 3-11: Endwall contour (shown are the relative positions of leading edge and trailing edge)

machine. A ball-nose, 1 in. end mill cutting tool is first used to cut the endwall axisymmetric contour which is then followed by cutting out the “blade profile slots” from the block of wood as shown in Figure 3-12. An allowance of 2 mm around the blade’s actual profile is given while making the cuts so that the blades can slide comfortably into the slots. This allowance doesn’t affect the precision of the blade-endwall assembly since it is smaller than the radius of the endwall fillet that is made around the blade-endwall junction at a later stage. A fine cut of approximately 0.0005 in. is used as a final step in establishing the desired contour shape. The manufactured endwall, as shown in Figure 3-12, is then sealed with a polyurethane sealant and then painted over with several coats in order to seal the pores that are a characteristic of the MDF boards. Five inserts are drilled into the rear side of the endwall to house 3/8th in. steel threaded rods to act as supports for the endwall.

Figure 3-12: (Left) Endwall fabrication in progress; (Right) Finished Endwall

3.2.3. Blade-Endwall Assembly

The assembly is an important step in the setting up of the facility since it determines the final orientation of the blade leading edge with respect to the wind tunnel. For this reason, the blade is assembled together with the endwall before it is placed at the desirable position in the test facility. After the manufacture of the three blades and the endwall, they are assembled together by placing the blades in the "blade slots" made in the endwall. A support frame structure (wooden frame bolted to Unistrut® rods) is manufactured into which holes are drilled for receiving the threaded rods, used for supporting the blades and endwall, as discussed above. This method ensures that the blade slots are correctly machined into the endwall and that the relative positioning of the leading edges of the endwall and the blades is as desired (parallel and at the required separation distance). The protruding threaded rods from the blades and endwall are fastened with the support frame structure, thus completing the assembly. As a final step, a round fillet of radius 0.3 cm is made using self-adhesive pliable caulk sealant around the blade-endwall junction. This is required for the purpose of sealing any gaps at the junction and to reduce the strength of the corner vortices formed by eliminating the square-edge junction shape.

3.3. Leakage Flow Generation Apparatus

Besides the mainstream flow, another important flow that enters the cascade passage is the 'leakage' flow, which must be conditioned properly to match the engine representative conditions. It simulates the flow that is introduced through the interfacial gap between the combustor and the first stage stator in a gas turbine. This gap provides clearance allowing for the thermal expansion to occur in the gas turbine. However, in order to prevent the ingression of the hot core gases into the gap, which may cause damage, relatively cooler gas is bled from the compressor into the gap in order to seal it. This leakage flow also has the potential to provide film cooling coverage over the endwall of the first stage stator

vane, an aspect that is being explored in the current study. For this purpose, a leakage plenum geometry is defined based on the design of the combustor-stator interfacial gap of a modern industrial gas turbine. Three values of the ratio of the leakage mass flow rate to the mainstream mass flow rate (MFR, mass flow ratio) are considered in the present study given by 0.5%, 1.0% and 1.5%. The flow rate of the leakage is metered using a 'Laminar Flow Meter' (working principle discussed in the next chapter). A detailed top view of the test section is given in Figure 3-13 and dimensions of the slot in Table 3-2.

Shown in Figure 3-13 are the arrows that mark the direction of the mainstream flow and the coolant flow. The leakage flow is generated with the help of a centrifugal fan, as discussed in Section 3.1.1.3. The flow supplied from the upstream delivery system enters a chamber from where it is redirected to the leakage plenum. It should be pointed out here that the leakage flow is heated when it enters the chamber since in the present study, it is the leakage flow that is at a higher temperature than the mainstream flow. The temperature difference created is used to 'mark' the leakage flow as it migrates and mixes within the passage. The heating power to the leakage flow is delivered by means of resistance heating elements installed in the wooden chamber preceding the leakage plenum. The power is regulated by means of a Variac variable AC transformer. A thin aluminum perforated plate with an open area ratio of 0.4 is placed at the entrance to the leakage plenum which gives an equalizing action on the non-uniform approach flow. It offers a resistance to the flow, creating a pressure drop, thus making the incoming flow spread over the front of the plate and eject out through the pores simultaneously, making the exit flow uniform in the process. The width dimension of the leakage slot is as specified by the sponsor. It is such that the velocity ratio of the leakage flow to the mainstream flow is approximately 1.0 at the MFR of 1.0%. The length of the slot, also specified by the

sponsor, is so that the flow has the opportunity to develop before it exits into the main passage (L/D ratio of approx. 20). It is a much smaller slot than the rotor-stator disc cavity used in a previous study of the rotor cascade in our lab (compare with Figure 0-4: Leakage flow supply plenum [54] in Appendix). The momentum flux ratio and the mass flux ratio of the leakage flow to the mainstream flow play an important role in affecting the flow mixing within the passage, as will be observed in the results. The exit of the slot (x/C_{ax}= -0.16) is

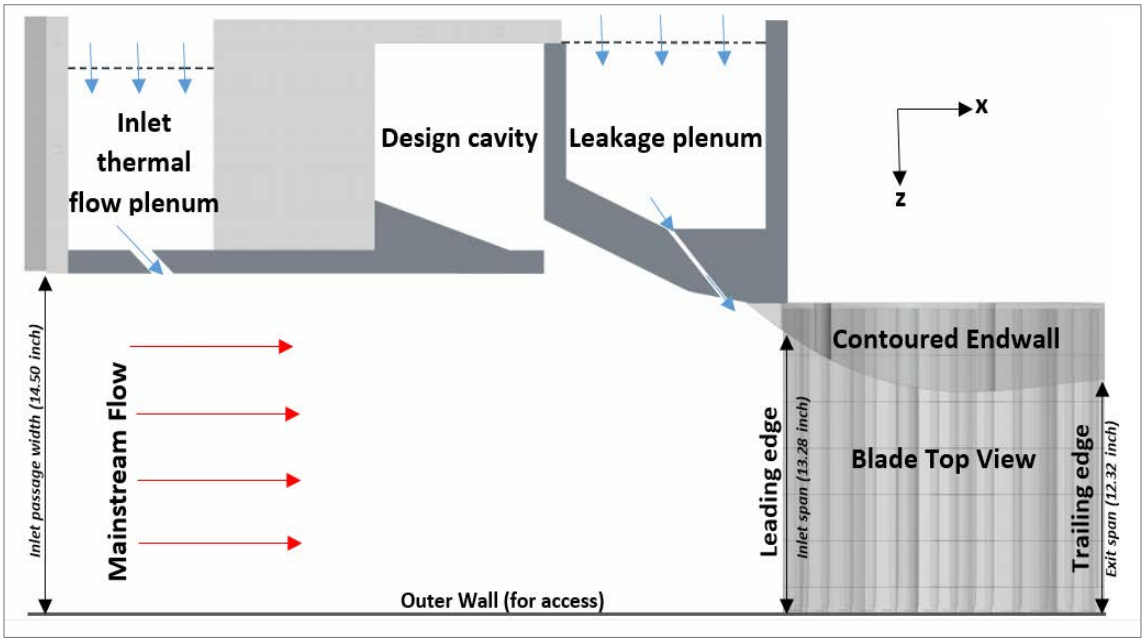

(a)

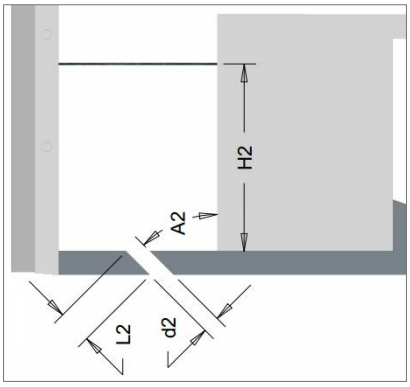

(b)

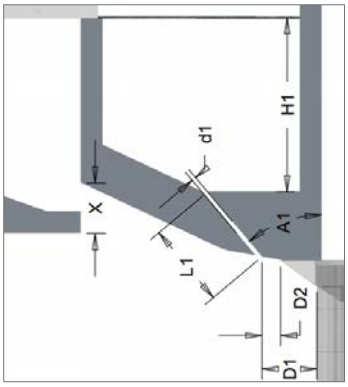

(c)

Figure 3-13: (a) Detailed top view of the test section (b) Important dimensions of approach flow temperature control slot (c) Important dimensions of leakage slot flow (values given in Table 3-2)

shaped in a slanting manner so that flow enters the passage in a direction that is aligned with the shape of the endwall, thus avoiding a sharp turn. This is as specified by the sponsor. In Figure 3-13, a cavity can be observed upstream of the leakage slot. This cavity has no flow going through it and only represents a design feature of the actual gas turbine. It creates a step in the direction of the mainstream flow. The geometry of this cavity is as given by the sponsor. On surveying with a wool tuft, it was found to have recirculating eddies.

Table 3-2: Dimensions of leakage slot and upstream temperature control slot (in centimeters)

D1, D2 (Distance of leakage slot exit from blade and endwall leading edge respectively)	3.22 cm, 1.09 cm	X (Slot height)	2.95 cm
L1 (Leakage slot length)	4.97 cm	L2 (Approach flow slot length)	1.8 cm
d1 (Leakage slot width)	0.25 cm	d2 (Approach flow slot width)	0.9 cm
A1 (Leakage slot inclination angle)	40˚	A2 (Approach flow slot inclination angle)	45˚
H1 (Plenum height)	10.24 cm	H2 (Plenum height)	10 cm

3.4. Approach Flow with Combustor Coolant Generation Apparatus

The mainstream gases exiting the combustor in a gas turbine contains combustor liner coolant, which makes the approach flow temperature profile non-uniform. This profile has a significant impact on the enhancement of the adiabatic effectiveness over the endwall, as found by previous studies [3]. Therefore, in the current study, instead of a flat temperature profile of the approach flow, an *engine representative* temperature profile is used (sample in Figure 3-14). Since in the present study, the temperature difference created between the mainstream flow and the slot flows is used to 'mark' the migration and mixing of the various flows within the passage, the slot flows are kept at a higher temperature than the mainstream flow. This implies that the engine representative temperature profile has heated flow nearer to the wall and cooler (nearly at room

temperature) away from the wall. Recall that in this study, we heat the leakage and combustor cooling flows whereas in the engine, they are coolant flows. A combination of two different methods is used to create the desired temperature profile, as discussed in the following sections.

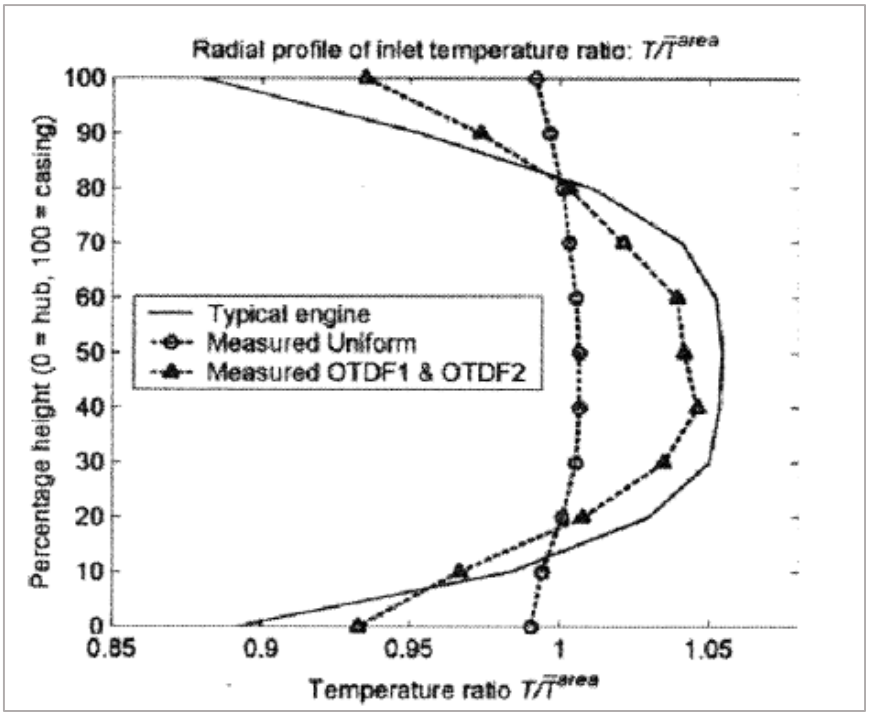

Figure 3-14: Circumferentially-averaged temperature distribution at the turbine vane inlet of first stage high pressure turbine. Shown is a measured profile in a real engine, a measured profile in a simulator in which distortions due to discrete fuel and dilution air injection and endwall cooling flows are active (OTDF1 & OTDF2), and a profile measured in the simulator when the inlet temperature distortion mechanisms are not active (measured uniform) [81]

3.4.1. Inlet Thermal Profile Flow Plenum

The near-wall fluid is heated with the help of an upstream slot (axial location $x/C_{ax} = -1.72$) that is designed to deliver the flow at a higher temperature than the mainstream flow. The temperature of the slot flow is adjusted such that the desired thickness of the temperature profile may be achieved. For this purpose, an “inlet thermal flow plenum” as shown in Figure 3-13, is designed. The plenum receives the flow as generated using a centrifugal

fan discussed in Section 3.1.1.4. From the header, the flow enters an acrylic chamber that connects to the inlet thermal flow plenum. A thin aluminum perforated plate with open area ratio of 0.4 is placed at the entrance to the plenum to create a pressure drop and make the exit flow more uniform. It should be noted here that this flow has been heated with the help of heating elements that are placed in the supply pipe line from the fan to the plenum. With the slot oriented at 45˚, the flow enters the passage and mixes with the near-wall fluid heating it up. The power emitted by heaters installed within the supply pipes is controlled using a Variac. A MagneTek GPD333 motor controller is used for varying the rotational speed of the fan that, when coupled with right amount of heating, can generate the desired temperature profile.

3.4.2. Approach Flow Resistance Heaters

The set-up described in the previous section can help generate a 'thin' temperature profile of heated flow since the heated flow out of the slot affects the near-wall fluid only. To generate the temperature profile that extends out to the mid-span location, more heating power spread over a larger region is required. For this purpose, three resistance heaters are used within the test section in the path of the approach flow located at 2.5 cm, 5 cm and 8 cm away from the wall (z=0) at axial location x/C_{ax}= -1.72. The resistance heaters are made by winding a Nichrome wire on a 1 cm diameter non-conducting rod. The power input to each heater is regulated by means of a Variac. The wakes and vortices forming as a result of placing these heaters in the path of the approach flow are expected to quickly disperse due to high levels of turbulence in the flow. As an improvement on the design, in order to subdue the von Karman vortex street formation, thin plate-like extensions are built onto the back side of each rod. By varying the power to the resistance heaters and the inlet thermal flow through the slot, the desired 'thick' temperature profile can be generated.

3.5. Wind Tunnel Exit Flow Management

It is important that to achieve a high Reynolds number (of the order of 10^5) for the present study, the flow must be diffused out into the atmosphere efficiently. For this purpose, a diffuser is designed and installed at the exit of the cascade connected to the blade trailing edge by means of tailboards. The following sections discuss in detail the diffuser and tailboards used in the present study.

3.5.1. Diffuser

The flow accelerates as it passes through the passage with the velocity becoming as high as four times the inlet velocity. The pressure must be recovered as the flow diffuses into the atmosphere. With inefficient diffusion, mass flow rate of the air entering the wind tunnel may reduce causing the inlet velocity and the Reynolds number to decrease. Also, the diffuser should have an optimum inlet to exit area ratio so that separation of the flow is under control. Based on these considerations and space limitations of the laboratory, a four-vane, three-passage curved diffuser is designed. The curved shape provides a longer path for the air to diffuse and the multiple passages provide optimum diffusion angle with no separation.

The front and back walls of the diffuser are made of 1.9 cm (3/4 in) thick plywood sheets. They hold 0.25 cm (3/32 in) thick acrylic sheets between them that form the panels separating the three passages within the diffuser, as shown in Figure 3-15, with each panel being made of two acrylic sheets. These acrylic sheets fit tightly into grooves cut into the plywood in addition to being glued into the grooves using epoxy resin. Threaded rods are used to clamp the plywood against one another to keep the acrylic panels tightly in place. The entrance region of the diffuser is particularly sensitive since it contains high velocity and low pressure regions. This subjects the diffuser panels, especially the

outermost panels, to large pressure difference on both sides. Also, any variability in pressure field from one diffuser passage to another may cause the acrylic panels to collapse out of the grooves. To ensure that equal amount of flow enters the two cascade passages with similar exit velocities, the design of the diffuser must be robust to withstand any variability of the flow that may occur during the qualification of the facility. Hence, an efficient design of the diffuser is developed using CFD simulation as well as experimental data available in the literature (Sovran [61] and Blevins [62]). The curvature is made such that the diffuser inlet plane is perpendicular to the flow streamlines coming from the downstream channel. An exit-to-inlet area ratio of 2.9 and inlet-to-exit plane angle difference of 15˚ are chosen. Diffuser length based on centerline arc is 124.8 cm (49.1 in). In a turbulent flow with higher momentum flow being brought nearer to the surface, the tendency of the flow to separate is delayed. Therefore, the diffusion angle chosen is considered appropriate.

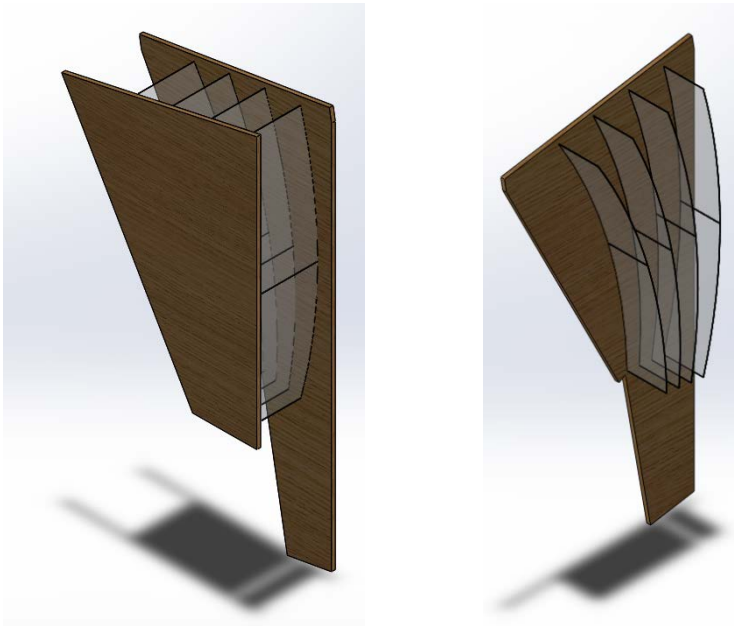

Figure 3-15: Diffuser (shown are the different views)

3.5.2. Tailboards

Tailboards form the link between the cascade's exit plane and the diffuser inlet. They play an important role in the matching of the blade static pressure profiles, as discussed in Section 5.1.1. They are made of 0.16 cm (1/16 in) thick acrylic sheets fixed using acrylic ribs that run across them in horizontal and vertical directions. The ribs in the horizontal direction are made adjustable to effect the curvature of the tailboard. The tailboards are installed so that they are coincident with the camber line of the airfoils at the trailing edge of the blade, but their curvature may change slightly using the adjustable ribs, which is crucial in getting equal amount of flow to enter both passages.

3.6. Access to Test Section

Access to the test section is facilitated by means of removable flat panels that form the flat endwall of the test section. Along with them, a movable hole panel is used, which allows to position the probes at the desired location and also acts as support for the various measurement probes. They are designed in such a manner that their position can be changed depending on the location where the measurement needs to be taken. An automated three-axis traversing system is used to precisely control the movement of the probes. All these components help in accessing all parts of the test section and taking the desired measurements.

3.6.1. Flat Endwall Panels and Movable Hole Panel

As can be seen in Figure 3-17, the flat acrylic panels along with the movable hole panel form the flat endwall (outer wall) of the test section. This endwall serves only to provide access to the test section and no measurements are taken on this endwall. These panels fit tightly once in place ensuring that no leakage into or out of the test section occurs through them. Care is taken every time while changing the positions and re-assembling these panels. To allow the movable hole panel to rotate, a very small clearance between

the flat endwall and the movable hole panel must be tolerated. For the purpose of adiabatic effectiveness and thermal field measurements, this small amount of leakage on the outer flat endwall does not affect the dynamics on the contoured endwall, hence it is considered insignificant to the experiment. The panels lock into place by means of latches. The outer wall rests on the table below it via support ribs, as shown in the Figure 3-17.

The movable hole panel (Figure 3-16) is made of aluminum consisting of inner and outer disks which rotate relative to one another facilitated by means of ball bearings along their perimeter. The inner disk has a hole on its edge that is capable of allowing a probe of maximum diameter 0.25 inch (0.64 cm). The reader may refer to Piggush [63] for more details on the design of movable hole panel.

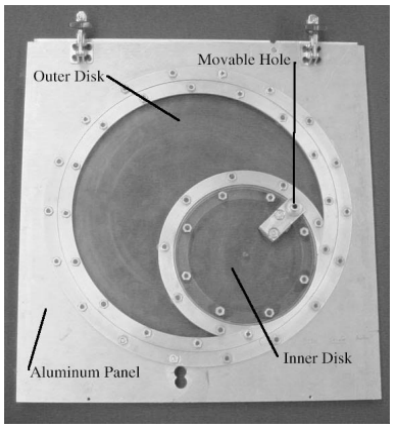

Figure 3-16: Movable hole panel for holding the measurement probe [63]

3.6.2. Automated Traversing System

An automated three-axis (covering the streamwise, spanwise and pitchwise directions within the passage) is used to control the position of the measurement probes (Figure 3-18). Three Velmex UniSlide® models are used for moving in all the three directions. Each unit is driven by a stepper motor having 1.8˚ rotation per step (200 steps per revolution).

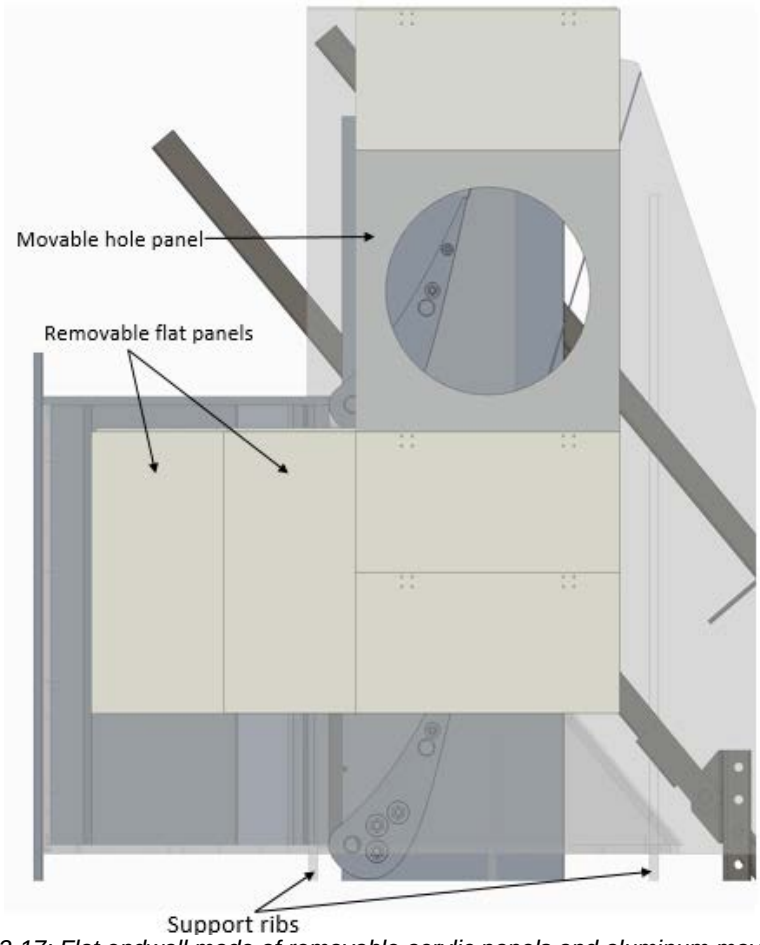

Figure 3-17: Flat endwall made of removable acrylic panels and aluminum movable hole panel

The unit that moves in the spanwise direction has a maximum travel distance of 45.7 cm (18 in) whereas as the remaining two (in streamwise and pitchwise directions) have maximum travel distance of 30.5 cm (12 in). All three units are placed on top of a table whose height can be adjusted for positioning the measurement system coarsely before making finer adjustments. A NF90 Series Stepper Motor Controller made by Velmex, Inc.

is used to control the three motors. To interface the hardware to the computer, an IOTech Serial 488A Bus Converter, IEEE 488.2 (GPIB) cable and National Instruments PCI-GPIB card are used. A software MEDAQ (Erickson [54]) on a Windows machine is used to send commands to the stepper motors which in turn control the movement of the traverse system. For approximate positioning of the probe, a joystick can be used, which controls the movement of the traverse system along all three directions.

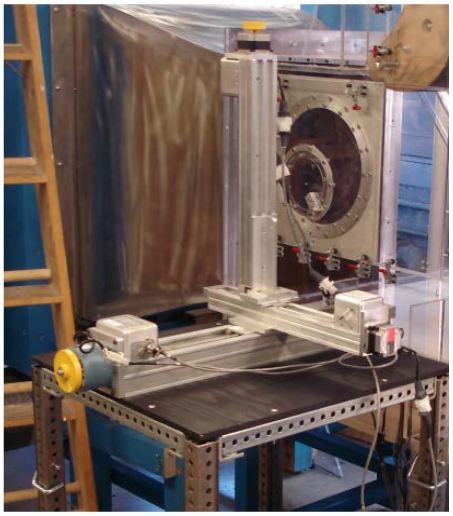

Figure 3-18: Automated traverse system made of Velmex Unislides [54]

Chapter 4 Experimental Techniques

This chapter discusses the experimental techniques used for measurement of velocity, pressure, temperature and leakage mass flow rate. Details of the various instrumentation used can also be found in this chapter. Calibration procedures and results for each type of instrument are described along with their accuracy of measurement.

4.1. Velocity Measurement

Velocity measurements are required in the current study as part of the qualification of the test facility. Two methods are used for measuring the velocity, thermal anemometry and Pitot - static tube. They are discussed in detail in the following sections.

4.1.1. Thermal Anemometry

Thermal anemometry is based on the principle of relating the heat transfer from an electrically heated sensor to the velocity of fluid passing over it. The correlation is most appropriate in applications where the properties like the fluid temperature, composition, density, viscosity and pressure may be assumed constant with the fluid velocity being the only significant variable affecting the heat transfer from the sensor. This technique can be implemented in forms of Constant Temperature Anemometer (CTA, used in the present study), Constant Current Anemometer (CCA) and Constant Voltage Anemometer (CVA).

Working Principle: For the present study, a constant temperature anemometer is used. It involves the use of a control circuit (Wheatstone bridge) with the sensor forming one leg of the bridge which maintains the resistance of sensor constant. The resistance can be linearly related to its temperature (hence a constant temperature implies constant resistance). When the sensor is placed in fluid, it gets cooled, the extent of which depends on the fluid velocity at the point of measurement. This results in lowering of the sensor's

resistance and hence an imbalance is created in the bridge. To bring the bridge back in balance, the anemometer modifies the voltage across the sensor to maintain it at the constant operating temperature. An expression relating the voltage to the velocity of fluid was developed by King [64]. The King's law is given in a general form as:

$$U^n = AV^2 + B \qquad \text{Eq. 4-1}$$

where U = Fluid velocity, V = Voltage, A, B are calibration constants and n = constant (typically 0.43-0.46 for practical hot wire sensors, 0.5 from King)

4.1.1.1. Instrumentation for Constant Temperature Anemometer

The Model 1750 Constant Temperature Anemometer made by TSI Inc. is used for taking the velocity measurements in the present study which works on the same principle as described above. As the sensor is cooled by the passing fluid, depending upon the power needed across the probe sensor, it modifies the voltage output thus maintaining the circuit in balance. The sensor can be maintained at 250 ˚C (recommended for use in air or gases) by adjusting the voltage across it. This sensor temperature is selected to optimize sensitivity and signal-to-noise ratio and maximize sensor's life. The power into the sensor is equal to its cooling rate. Therefore, based on the King's Law described above, a relationship can be established between the voltage measured and the velocity of the fluid to calibrate the sensor. More details on the working and setting up of the anemometer can be found in the TSI manual. The output from the anemometer can be digitized and used to characterize several important flow quantities in the present study; for example, inlet plane velocity measurements and turbulence properties.

The thermal sensors may be in the form of hot-wire or hot-film. Each type of sensor has its own advantages and is chosen depending on the application. A film sensor (typically 50 μm) is suitable for measurements in liquids or gases with particle contamination due to

its relative rigidity against straining or breaking by the particles. Its disadvantage lies in the self-generated turbulence intensity that may limit its performance. A hot-wire sensor with its typical small size (4 μm) has a high frequency response and a reduced output noise due to flow fluctuations caused by sensor itself [60]. After matching the characteristics of the sensor and the flow conditions in the present study, a hot-wire sensor is selected for the present study. Two different models of the platinum coated tungsten hot wire, made by TSI Inc., are used. These are shown in Figure 4-1. One is a Model 1210 General Purpose Probe which uses a straight wire for measuring one component of velocity. To measure this component, the axis of the probe body is held perpendicular to the component of the velocity to be measured. The other is a Model 1218 Standard Boundary Layer Probe which is used to make near-wall measurements. The sensor wire is oriented perpendicular to the axis of the probe body. Hot wires are extremely delicate and may break with a slightest bump on the wall. In a boundary layer probe, this is taken care of by means of a protective pin that sticks out along the axis of probe body such that the sensor is protected. Also the shape of the boundary layer probe is such that there is minimal interference, allowing for accurate measurements within the boundary layer.

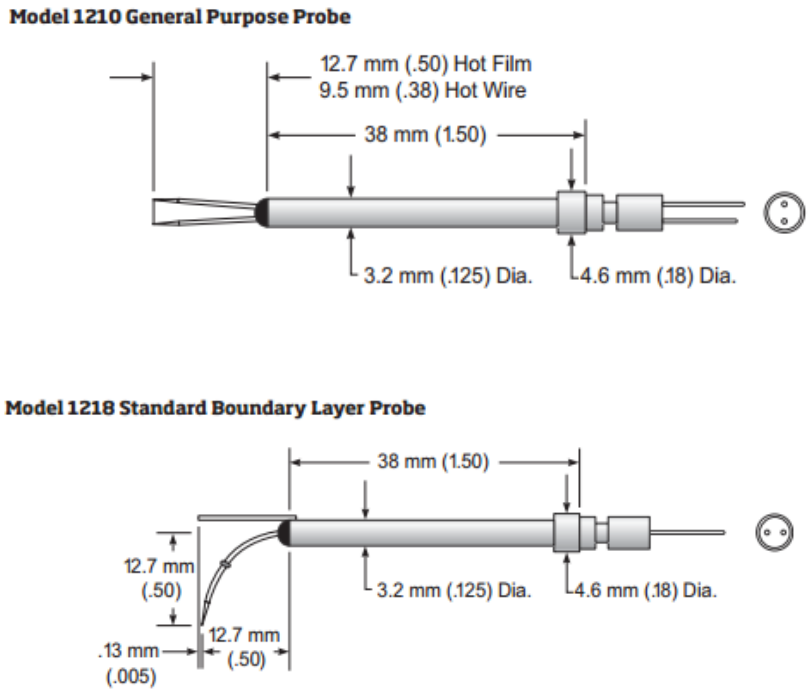

Figure 4-1: Top: General purpose probe for measuring one component of velocity; Bottom: Boundary layer probe for near wall measurements [82]

4.1.1.2. Hot Wire Sensor Calibration

The constants for Eq. 4-1 are obtained after proper calibration of the hot wire so that it can be used for measurements. For this purpose, a 'calibration jet facility' developed by Wilson [65], is used to generate flow with a known velocity. The facility (refer to Figure 4-2) consists of a pressure regulated air supply, a stilling chamber with turbulence reducing screens and an elliptical contraction followed by the calibration chamber, as shown in the figure. Building supply air is fed to an adjustable pressure regulator followed by a needle control valve. The air is deflected by a baffle plate as it enters the stilling chamber. It then passes through a honeycomb aluminum flow straightener, a thick plate of porous sintered stainless steel, and five sets of turbulence control screens that damp out the turbulence in the flow. This is followed by a 14:1 elliptical contraction nozzle leading to the calibration chamber and another metering nozzle at the exit. For the present purpose, the flow at the

exit of the metering nozzle is used where the hot wire is placed such that the wire is oriented perpendicular to the flow direction. The wire should be placed close to the nozzle exit so that it lies in the region of uniform flow at the exit, but not too close so as to cause a blockage to the flow. The static pressure within the chamber is measured by connecting it to an inclined manometer. The difference of the measured pressure and the ambient pressure can be then used to evaluate the velocity of the flow exiting the jet facility by way of the calibration coefficients that were determined for the jet facility.

The anemometer is then set up by first checking its pulse frequency response. The procedure involves sending a square-wave at about 1 kHz to the anemometer circuit and then viewing the signal output on an oscilloscope. For more details, the 1750 CTA manual can be consulted. The connecting cable resistance should be adjusted so that the recommended operating resistance (determines the final operating temperature of sensor) of the sensor is obtained. The output of the anemometer is connected to an Agilent 34411A data acquisition unit which is connected to the computer using a National Instruments GPIB-USB converter interface modem. The temperature within the chamber

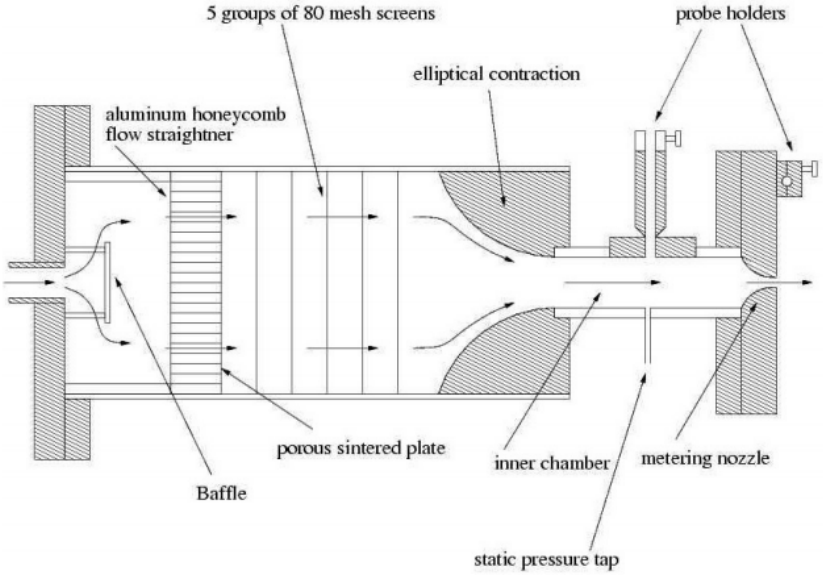

Figure 4-2: Calibration jet facility [83]

(needed for evaluating the density of the flow) is measured by inserting a thermocouple probe and configuring the output to be on another channel of the same data acquisition unit, allowing for simultaneous measurement. The detailed connections are given in Figure 4-3.

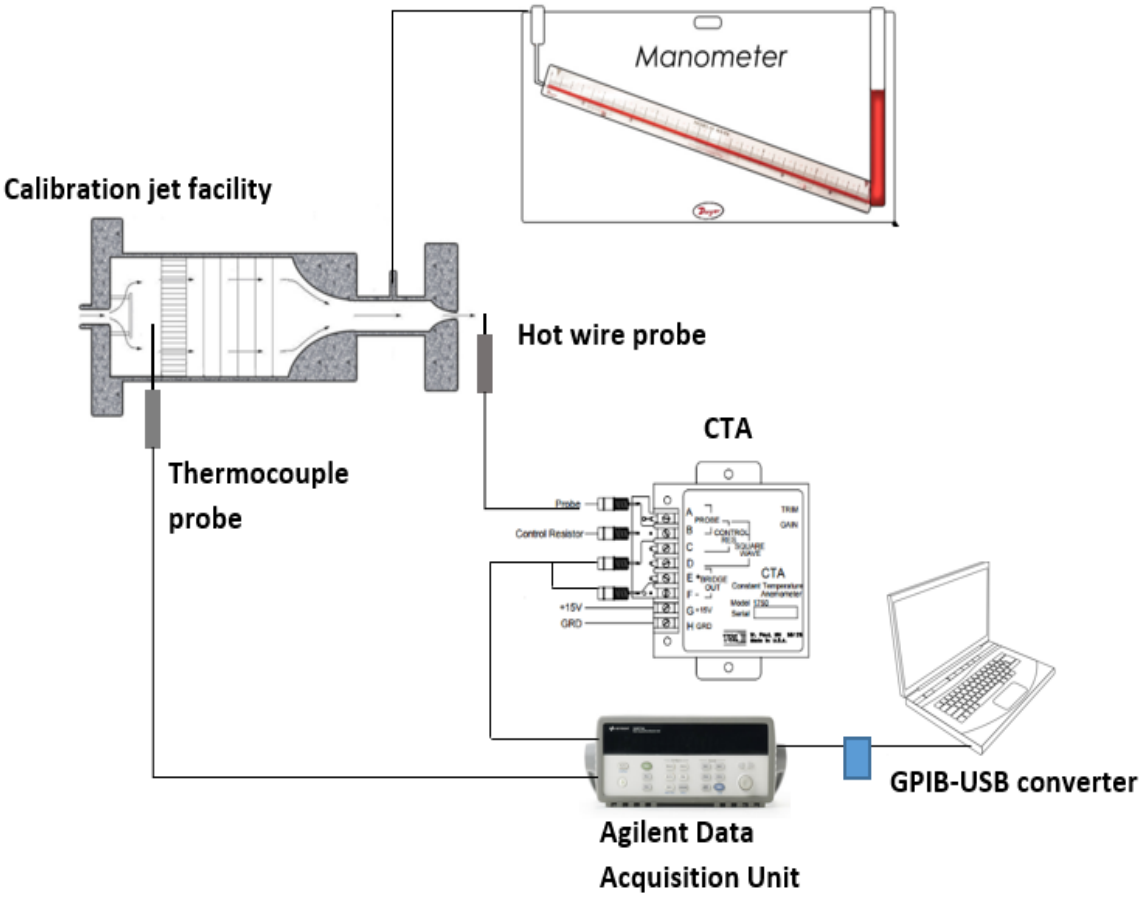

Figure 4-3: Calibration set up for hot wire anemometry

The hot wire is mounted at the exit of the metering nozzle of the jet facility and the needle valve are opened. The $\Delta P = P_{chamber} - P_{ambient}$ values are increased from 0 inches of water to 2 inches of water in increments of 0.06 inches of water by controlling the needle valve. At each ΔP, the anemometer output voltage and the thermocouple output are recorded

for a period of 30 seconds. Finally at the end, the ambient pressure and humidity are recorded for reference.

4.1.1.3. Hot-Wire Sensor Calibration Results

The measured ΔP is used to calculate the velocity of the fluid exiting the jet facility, which is then related to the measured anemometer voltage using the King's law described above. A sample calibration curve is shown in Figure 4-4. A least squares fit method is used to get the best fit equation. The relationship, which is fairly linear, thus obtained is:

$$U^{0.453} = 1.6284V^2 - 2.0349 \qquad \text{Eq. 4-2}$$

The coefficient of determination R^2, a statistical quantity to define how well the fit is, for the given curve is 0.9992.

Errors in Measurement: It is important to define the uncertainty of the measurements to be able to assess the quality of the data. There can be sources of error which may add to the uncertainty. The principle on which the thermal anemometry is based can account to some error. Velocity is not measured directly but is a resultant of the convection heat transfer from the sensor. The sensor is unable to differentiate between the cross-stream components and the desired component perpendicular to the sensor's orientation. Also, it is insensitive to flow reversals, thus leading to a significant uncertainty. A total uncertainty of 5% based on these considerations is suggested by Oke [66].

This brings out another important aspect of holding the probe steadily when taking measurements. Any sort of vibrations may cause the sensor to measure the relative velocity component rather than the absolute value. It is also important that the wind tunnel is run for a sufficient amount of time for any kind of contaminants borne in the air to flow out in order to protect the sensor and to reproduce the same calibration conditions as

closely as possible and hence yield repeatable results. A failure to do this may add to the measurement inaccuracy.

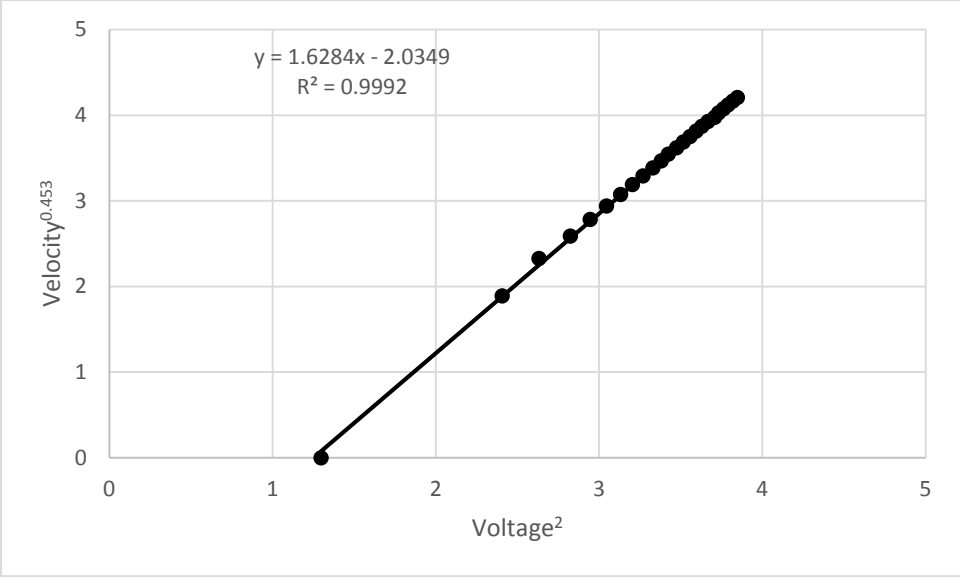

Figure 4-4: Sample hot wire calibration curve

4.1.2. Pitot - Static tube

While thermal anemometry is used for taking accurate and detailed velocity measurements in the qualification of the flow, a pitot-static tube can be used while setting up the test facility at an initial stage. It is much easier and faster and can predict the mean velocity of the flow quite well.

In the present study, the flow is assumed incompressible due to the low Mach number of the flow (~0.17 based on exit velocity). Therefore, the Pitot-static tube may be used to calculate the velocity considering an incompressible flow with negligible viscous effects. A typical Pitot-static tube has two outlet ports, one for total pressure and the other for static pressure connected to two separate conduits within the main body. The total pressure is measured as the flow is isentropically brought to rest at the probe tip whereas the static

pressure is measured through the holes on probe body. The hole axes are aligned perpendicular to the flow direction. To correctly position the probe to measure the velocity, the probe is rotated to different yaw angles until maximum pressure difference is read on the pressure measurement device (discussed in Section 4.3.1). The velocity is then given by:

$$U = \sqrt{\frac{2(P_t - P_s)}{\rho}} \qquad \text{Eq. 4-3}$$

where U = Velocity, P_t = Total pressure, P_s = Static pressure, ρ = density of fluid.

Errors in Measurement: The misalignment of the probe with the flow may cause incorrect stagnation pressure and static pressure to be read. In a turbulent flow, the indicated mean total pressure read from the probe can be high by an amount $\rho\overline{u'^2}/2$, however u' must be 20% of mean velocity before turbulence term effect amounts to 4% of mean dynamic pressure (for present study, u' ~ 11% of mean velocity) [60]. To check for viscous shearing effect in case of low Reynolds number that causes the probe to read higher total pressure, the Re_r based on probe's diameter is calculated. For present study, Re_r = 2500 is considered high enough to neglect this effect [67]. Also, a small diameter of pressure probe is desirable to reduce the blockage caused to the flow. Before use, it is ensured that the probe tip is free of any burrs. In case of a compressible flow, static pressure and total pressure needs to be measured separately and used in the isentropic relationship (p_o/p= f(M)) to evaluate the dynamic pressure head.

4.2. Turbulence Measurement

The flow exiting the combustor in a gas turbine has high free stream turbulence with large eddy length scales. These turbulence characteristics can have a significant impact on the endwall heat transfer. Therefore, it is necessary that the mainstream flow approaching the

test section has the desired turbulence characteristics. For this purpose, an upstream turbulence generator is used, as discussed in Section 3.1.2. It is important to document the various turbulence characteristics, for example, turbulence intensity (Tu), turbulent kinetic energy distribution (energy density spectrum) and turbulence length scales (integral length scale Λ, energy length scale Lu, Taylor microscale λ). This is required as part of the qualification of the approaching mainstream flow to the test section. These quantities may be determined by either taking measurements of temporal fluctuations of velocity at a given point in space or by measurement of velocity signals at points separated in space at a given time and then correlating them using autocorrelation functions. For the present study, the first method is used by measuring one component (longitudinal along axial direction of the test section) of velocity and processing the signal to compute the above quantities. The details of hot wire anemometry used for these measurements have been discussed in the preceding sections. The procedure of computing various turbulence properties from the measured velocity signal are discussed in the following sections.

4.2.1. Root Mean Square Velocity Fluctuations and Turbulence Intensity

Physically, the intensity of the turbulence quantifies the kinetic energy of fluctuating flow as compared to the kinetic energy of mean flow. Thus, mathematically it can be defined by the ratio of root mean square velocity, U_{rms}, to the mean velocity, $\overline{U}$ as given in Eq. 4-6. The quantity U_{rms} is essentially the standard deviation of the velocity fluctuation, u' = u(t) - $\overline{U}$. It should be noted that the mean of u' will be zero for a turbulent flow with steady mean properties. A sample time based signal is shown in Figure 4-5. The higher the value of Tu, the more energy is contained in the fluctuating flow representing higher turbulence levels. The following equations are used for computing these values for a particular velocity time signal (waveform) for qualifying the approach flow:

$$U_{rms} = \sqrt{\frac{1}{N}\sum_{t=1}^{N}(u(t) - \bar{U})^2} \qquad \text{Eq. 4-4}$$

$$\bar{U} = \frac{1}{N}\sum_{t=1}^{N} u(t) \qquad \text{Eq. 4-5}$$

$$Tu = \frac{U_{rms}}{\bar{U}} \qquad \text{Eq. 4-6}$$

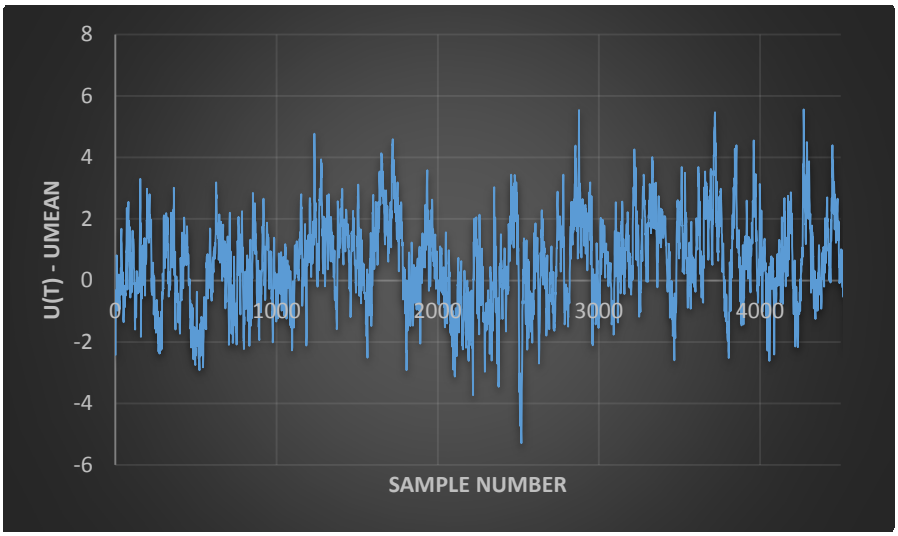

Figure 4-5: Sample velocity fluctuation signal (a part of a longer time-based signal)

4.2.2. Energy Density Spectrum

It is interesting to analyze the distribution of turbulence kinetic energy over a broad range of fluctuation frequencies. This distribution is known as the Energy Density Spectrum (EDS) which can be obtained by measuring the velocity signal at a given point in space over a period of time (Taylor's frozen flow hypothesis). It also adds more details to the description of the turbulent flow because turbulence intensity may not always completely define the flow characteristics. The frequencies are essentially a measure of the various length scales of turbulent eddies contained within the flow. A large size of eddy will lie in the lower frequency zone and vice versa. The generation of turbulence occurs in the

turbulence generator upstream of the test section where the core flow and cross flow jets interact with each other creating shear. This causes kinetic energy to be lost by the mean flow to the fluctuating flow acting as a continuous source of turbulence for the flow. This energy transfer is governed by the dynamics of the large eddies with the extraction occurring at integral length scales. The energy is continually transferred from large eddies to smaller eddies driven by vortex stretching and leads to viscous dissipation at the smallest length scales. At the smallest length scales, the molecular viscosity becomes appreciable and dissipates the kinetic energy to thermal energy. Thus, the EDS gives information about the distribution of kinetic energy contained among different size groups of eddies and several important characteristics can be evaluated from it; for example, the integral length scale (Λ) , energy length scale (Lu), Taylor microscale (λ), and turbulent kinetic energy dissipation rate (ε). The reader is referred to an in-depth study of the physical characteristics of the energy density spectrum by Tennekes and Lumley [68].

The first step in evaluation of these properties is to measure the velocity signal at a given point in space, which is done in the present study at a sampling frequency of 10 kHz for a period of 60 seconds. For the purpose of sampling the data, an Agilent 34411A Digital Multimeter is used. It is important to choose a high sampling frequency for a sufficiently long period of time in order to have enough data samples to form the spectrum containing all the expected ranges of fluctuation frequencies (large and small eddy length scales). Multiple signals may be recorded at a given point and averaged to reduce the ‘noise’ (variability in neighboring bins) in the resultant spectrum. A low pass filter can be used to avoid aliasing by satisfying the Nyquist criterion. If this is not done, then the spectrum obtained at frequencies higher than the Nyquist frequency will be aliased, causing the evaluation of the smallest scales of turbulence to be inaccurate.

Now, the instantaneous velocity signal (u(t)) is converted into fluctuations with respect to its time-averaged mean (u' = u(t) - $\overline{U}$). Note that the mean of velocity fluctuations will be equal to 0. This time-based series must be now converted to frequency domain by performing a Discrete Fourier Transform (DFT) on the signal. This can be achieved by using Cooley-Tukey Fast Fourier Transform (FFT) algorithm. This is a popular method adopted to compute DFT since it reduces the computational time. A program is written on Matlab using its built-in FFT function, which yields two equal-length arrays, one corresponding to the transformed DFT coefficients (j^{th} term shown) and another corresponding to the frequencies. The j^{th} terms of both arrays are shown below:

$$\phi_j = \frac{1}{\sqrt{N}}\left(\sum_{k=1}^{N} u'(t)e^{i\left(\frac{2\pi j}{N}\right)k}\right)$$

$$w_j = \frac{w_s j}{N} \qquad \text{Eq. 4-7}$$

where

ϕ_j= Transformed coefficient (contains real and imaginary parts)
N = Number of samples of $u'(t)$
$u'(t)$ = Velocity fluctuations about mean
k = Index of $u'(t)$ array (k =1 to N)
j = Index of ϕ array (j = 1 to N/2)
w_j = j^{th} element of array of fluctuation frequencies
w_s = Sampling frequency

It should be pointed out here that different software programs use different normalizing constants in their definition of DFT ($\frac{1}{\sqrt{N}}$ must be included in the Matlab program used in this study). Therefore, the expressions derived for the present study for computing various quantities here have been modified to include the $\frac{1}{\sqrt{N}}$ constant. The w_j array contains the

range of frequencies that are contained within the $u'(t)$ array. Now, for each w_j frequency, a corresponding element in the ϕ_j array is obtained, which denotes the fluctuation for that frequency. The resolution of the spectrum is determined by the total number of samples and is given by $\Delta w = \frac{w_s}{N}$. As mentioned above, each element of the ϕ_j array is a complex number where the real part denotes amplitude and imaginary part denotes the phase relative to the start of the $u'(t)$ signal. Therefore, both of these components contribute to the formation of the energy density function, $E(w)$.

The basic idea behind forming the energy density function is the satisfaction of the Parseval's equality theorem for a Discrete Fourier Transform. It implies that the total variance of the time based series is equal to the total variance of the transformed series, as given in Eq. 4-8 by Hinze [69]. It is important to perform this check once the FFT algorithm is run and the array is obtained.

$$\int_0^\infty E(w)dw = u_{rms}^2 \qquad \text{Eq. 4-8}$$

To be able to perform this check, it is necessary to first evaluate $E(w)$ from the ϕ_j evaluated above. This is done by adapting the definition given by Stull [70] to include the normalizing constant used above. It is given below as:

$$E(w) = \frac{2[{\phi_{real}}^2 + {\phi_{imag}}^2]}{N\Delta w} \qquad \text{Eq. 4-9}$$

The energy density function has the units of turbulence kinetic energy per frequency (m^2 / s^2 Hz). Now this function can be plotted against w_j to yield the desired Energy Density Spectrum.

Shown in Figure 4-6 is a sample energy density spectrum on a log-log plot. The red curve is obtained after applying a smoothing function to the spectrum. The 'smoothed' EDS is

then made to check for the condition of Parseval's equality in Eq. 4-8. As can be seen in the spectrum, the low frequency region has very small number of data points indicating that this region represents the fewer, larger sized eddies. It is the high frequency region where most of the data lie, indicating the region of smaller sized eddies. The energy is transferred from large eddies to small eddies, a concept often termed in the literature as "energy cascade." There exists a region (from 200 Hz to 900 Hz) within the energy cascade that is fairly linear, with a slope very close to -5/3. This region is called the "inertial subrange," as identified by Kolmogorov [71]. This refers to the region where kinetic energy is being transferred from one length scale to the other without much loss to the viscous dissipation. It is important to identify this range because it is from this range that the various properties discussed in next section are obtained. It is given by the following empirical relationship as given by Ames and Moffat [72]:

$$E(w) = \frac{18}{55} A\varepsilon^{2/3} w^{-5/3} \frac{2\pi^{-2/3}}{\overline{U}} \qquad \text{Eq. 4-10}$$

Also useful is the von Karman spectrum formula, which is used later in the study to compare with the measured spectrum. It is given by Ames and Moffat [72]:

$$E(w) = \frac{4{u_{rms}}^2 \Lambda}{\overline{U}\left[1 + \left(\frac{8\pi w \Lambda}{3\overline{U}}\right)^2\right]^{5/6}} \qquad \text{Eq. 4-11}$$

Here Λ denotes the integral length scale. Different values of Λ can be used to get the best fit spectrum that matches the measured EDS as closely as possible.

The energy spectral distribution can also be evaluated from the EDS, which is obtained by multiplying each $E(w_j)$ value with its corresponding w_j frequency. This will give the distribution of turbulence kinetic energy (m^2/s^2) with respect to the frequency. This can be useful in visualizing which frequency ranges contain which shares of the turbulence energy in a turbulent flow. A sample distribution curve is shown in Figure 4-7.

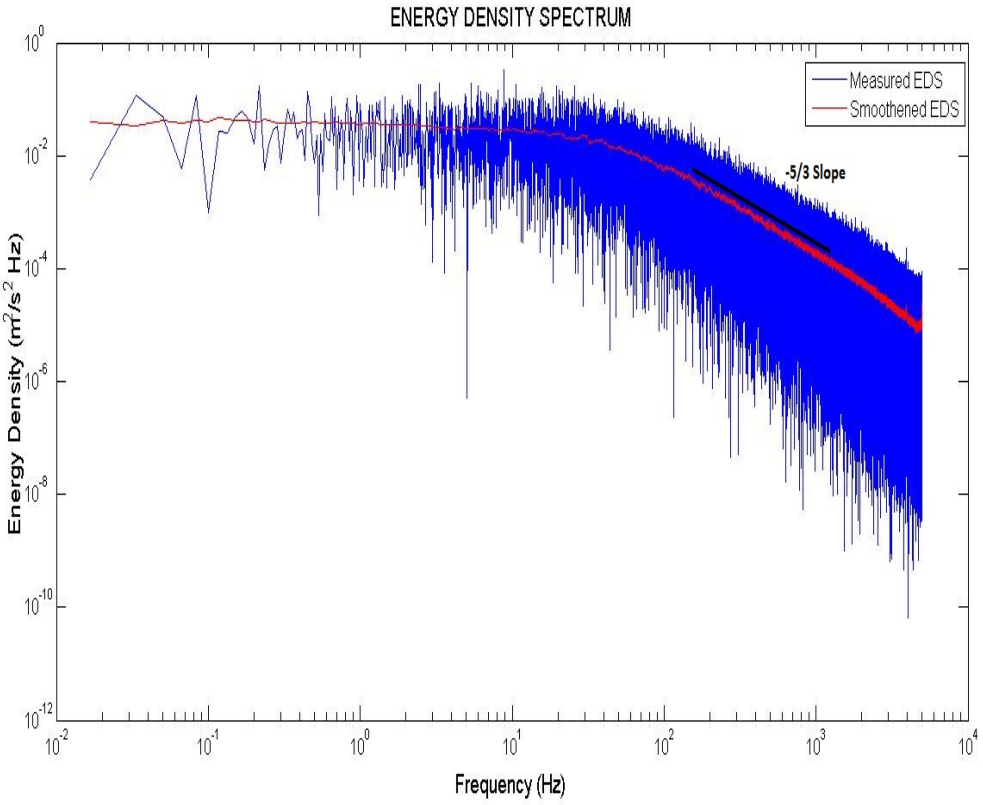

Figure 4-6: Sample Energy Density Spectrum

4.2.3. Turbulence Length Scales

After analyzing the distribution of turbulence kinetic energy over the various frequencies, the calculation of eddy length scales actually contained within the flow is performed. This gives a more complete picture of the turbulent flow in this study.

Before getting to the point where the length scales can be calculated, it is essential that the rate at which the turbulence kinetic energy is being dissipated into thermal energy at

the smallest scales is evaluated. For this purpose, the inertial subrange identified in the preceding section is used. Since this range shows a fair linearity with slope -5/3, any point is chosen and then the turbulent kinetic energy dissipation rate is evaluated as:

$$\varepsilon = \frac{16.2\, E(w_1)^{3/2} {w_1}^{5/2}}{\bar{U}} \qquad \text{Eq. 4-12}$$

This expression is obtained after rearranging Eq. 4-10. Here, w_1 is simply the abscissa of the point chosen in the inertial subrange on Figure 4-6. $E(w_1)$ is the ordinate corresponding to the chosen point.

The first length scale calculated is the integral length scale, Λ. Its expression doesn't include the dissipation rate, ε, because the larger eddies are not much affected by the viscous dissipation and are governed by the geometrical parameters. Physically, it represents the largest eddies contained within the flow. It can be calculated from the expression given by Hinze [69]:

$$\Lambda = \frac{\bar{U}}{4} \lim_{w \to 0} \frac{E(w)}{u_{rms}^2} \qquad \text{Eq. 4-13}$$

The spectrum curve (Figure 4-6) has its frequency tending to zero in a fairly flat manner. Therefore, a point can be chosen on this line and the corresponding E(w) can be used to evaluate the integral length scale. However, it should be noted here that there are very few points in this region that contributes to the uncertainty in the calculation of the integral length scale. For this reason, it should be emphasized that the velocity signal must be recorded for a sufficiently long period of time so that enough waves at this low frequency may be captured. Another factor that adds uncertainty to the calculation of integral length scale is that the curve in the low frequency region is not of an "ideal" flat shape which may cause an error in choosing the correct point in this region.

The next length scale which is calculated is the energy length scale, Lu. This represents the mean energy containing eddy size and is given by Ames and Moffat [72]:

$$Lu = 1.5\frac{u_{rms}^3}{\varepsilon} \qquad \text{Eq. 4-14}$$

As the turbulence kinetic energy cascades down from one turbulence length scale to another, it is finally dissipated off into thermal energy by effect of viscosity at the smaller scales of eddies. To characterize the smaller scales where the viscous dissipation is dominant, the Taylor microscale is calculated using the expression given by Hinze [69]:

$$\lambda = \sqrt{\frac{15\nu u_{rms}^2}{\varepsilon}} \qquad \text{Eq. 4-15}$$

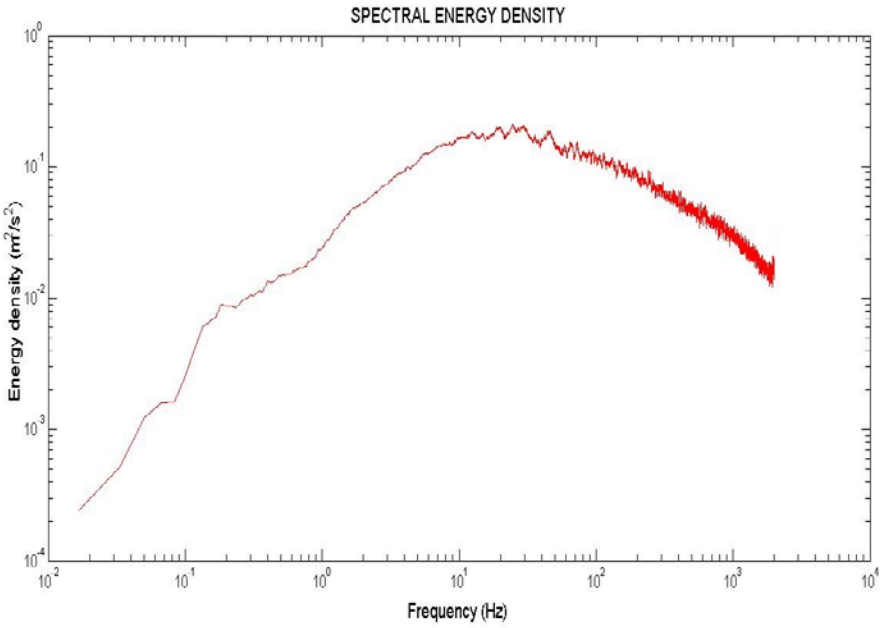

Figure 4-7: Sample spectral energy density distribution

4.3. Pressure Measurement

Measurement of the pressure forms an important part of the present experimental study. It is required while qualifying the test facility and also for the leakage flow mass flow rate to mainstream flow rate documentation. Several pressure measurement devices are used, depending on the application. They are mainly categorized as *manometers* and *pressure transducers*. For surveying various parts of the test facility, a combination of static pressure probes and taps are used. The following sections give a detailed description of these devices/probes.

4.3.1. Pressure Transducers

For the measurement of blade static pressure profile, the pressure transducer is chosen over the manometer in order to capture the data in the turbulent flow more accurately by measuring at a higher frequency followed by averaging the data set. In the present study, variable reluctance type transducers are used. In the following sections, details of the transducer and its calibration procedure are discussed.

4.3.1.1. Instrumentation

The instrument is a Model DP15 variable reluctance type pressure transducer used in conjunction with a CD15 carrier demodulator. Both instruments are manufactured by Validyne Engineering Corporation. The pressure range that the transducer is capable of measuring is ±1400 Pa (±5.5 inches of water) which is considered adequate for the present study. The transducer consists of a diaphragm made of magnetically permeable stainless steel clamped between two blocks of stainless steel. Each block has an embedded inductance coil on an E-shaped core. In absence of any pressure difference on both sides of the diaphragm, an equal gap of about 0.005 inch exists. The transducer has two ports to connect to the lines for the two pressures that must be measured. On application of a pressure difference, the diaphragm deflects towards the gap with lower

pressure causing the magnetic reluctance to vary, which in turn leads to the variation in inductance of the coil. The transducer forms one half of an AC bridge circuit that senses these changes. The other half of the circuit lies in a *carrier demodulator* which amplifies and rectifies (demodulates) the AC signal and outputs a ± DC voltage (indicates magnitude and polarity) which can be then read by a voltmeter. For the given pressure range, the voltage output is within ±10 volts. The deflection of the diaphragm changes linearly with the applied pressure difference, which makes the voltage output vary linearly with the pressure difference.

4.3.1.2. Pressure Transducer Calibration

To be able to use the transducer, it is necessary to obtain the relationship between the pressure difference applied and the voltage read. This is achieved by means of calibration, the detailed connections for which are shown in Figure 4-8. The procedure requires an instrument that can generate a known pressure difference. For this purpose, the calibration jet facility discussed in section 4.1.1.2 is used. First, the transducer is connected to the carrier demodulator CD15 using the Validyne's 4-pin transducer cable. The output terminals of the CD15 on its front panel are connected to an Agilent 34970A data acquisition unit and also to a digital voltmeter. The next step is to set the ZERO of CD15's potentiometer before beginning any measurements. This is done by leaving both the ports of transducer open to the atmosphere and reading the voltmeter. The ZERO knob is turned until the voltmeter reads 0 volts DC. Now, the highest voltage corresponding to the highest pressure, i.e. 5.5 inches of water, must be set so that the measuring range can be defined. To do this, the static pressure tap of the calibration jet facility is connected to the high pressure port of the transducer. Using about the same length of plastic tubing, the high pressure port is simultaneously connected to the manometer. The building supply is opened until the manometer reads 5.5" water. Now on the CD15 front panel, the SPAN

knob is turned until the output on voltmeter reads +10 volts DC. The calibration jet is turned off and the reading on the voltmeter is again checked. If it is not 0 volts (corresponding to a pressure difference of 0), then the ZERO knob must be again properly adjusted.

The throttle valve of the calibration jet is now opened beginning from ΔP = 0, in increments of 0.5 inches of water, until 5.5 inches of water is reached. Corresponding values of voltage are acquired by the Agilent unit, each reading for a period of 30 seconds. The same procedure is followed going back from 5.5 inches of water to ΔP = 0 to confirm repeatability of the transducers. The pressure tubing is now reversed with the tubing from calibration jet connected to the low pressure port of transducer. Again the same procedure

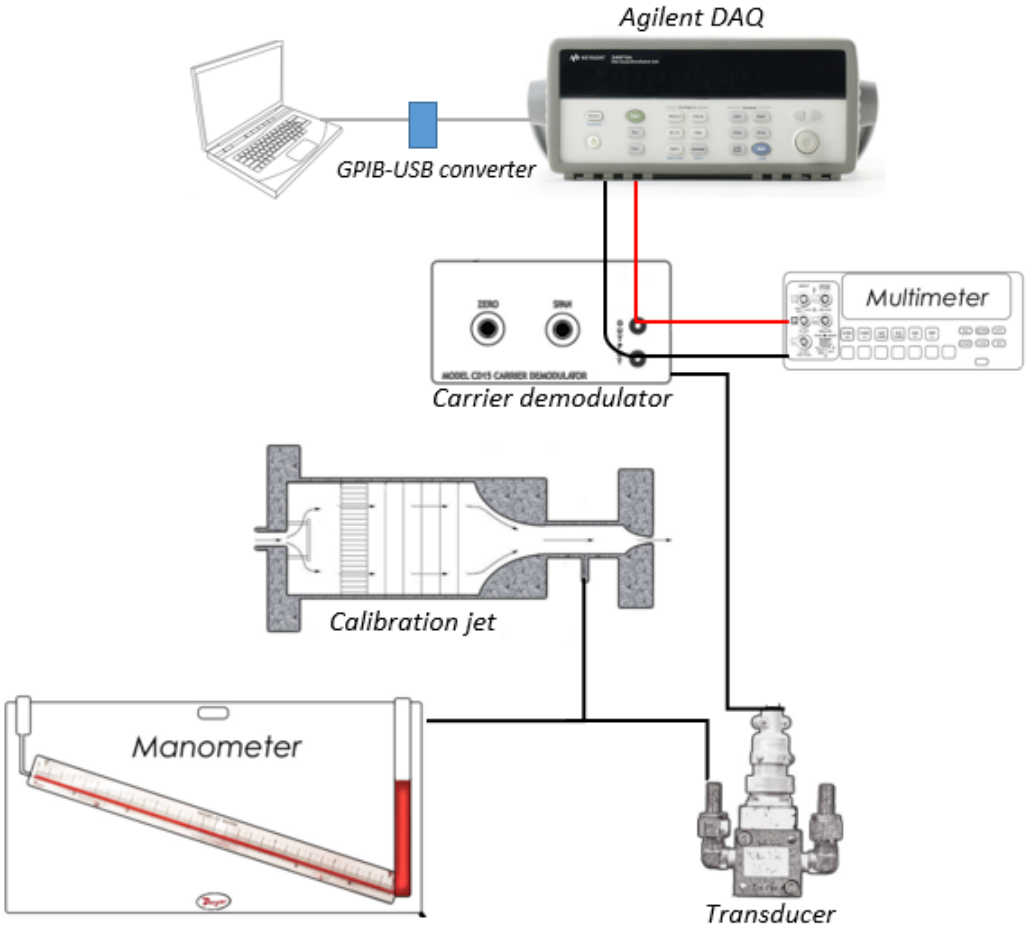

Figure 4-8: Pressure transducer calibration set-up

is repeated noting that the voltage read is now negative with same magnitude. This exercise is necessary to check for hysteresis indicating that the diaphragm has been over-stretched (beyond its pressure range) and damaged. If magnitudes are not the same then the diaphragm must be replaced.

4.3.1.3. Pressure Transducer Calibration Results

The measured voltage is plotted against the pressure difference. Each voltage value has been taken for a period of 30 seconds, therefore a mean value is calculated corresponding to each pressure difference value. Two pressure transducers were used in the present study. Their calibration results are shown in Figure 4-9. A least square fit is performed for each case. The coefficient of determination, R^2, for both curves are quite close to 1 indicating the quality of the fit. A cubic polynomial is fit to be as accurate as possible, but it can be seen that the coefficient of third degree of 'x' variable is quite small. Therefore, voltage variation with ΔP is fairly linear with the same magnitudes (only sign reversed) for reversed ΔP. This indicates that diaphragms for both transducers are in good shape and do not need replacement.

Errors in measurement: The reported accuracy of the DP15 transducer as given by manufacturer is 0.25% of full scale pressure range which includes the effects of non-linearity, hysteresis and non-repeatability [73]. Some precautions may help make the measurements even more accurate. It is advised that before each cycle of measurements, the ZERO of the potentiometer must be checked corresponding to ΔP = 0. It should be adjusted if required because DC voltage output from the transducer system seems to drift with time and temperature changes. If one notices erratic or excessive ZERO shifts then a check should be made for leaks in the system, loose body bolts or damaged diaphragm. Care must be taken that the diaphragm is not subjected to excessive pressure (beyond its

prescribed range) during the course of the experiment as it may over-stretch and damage the diaphragm.

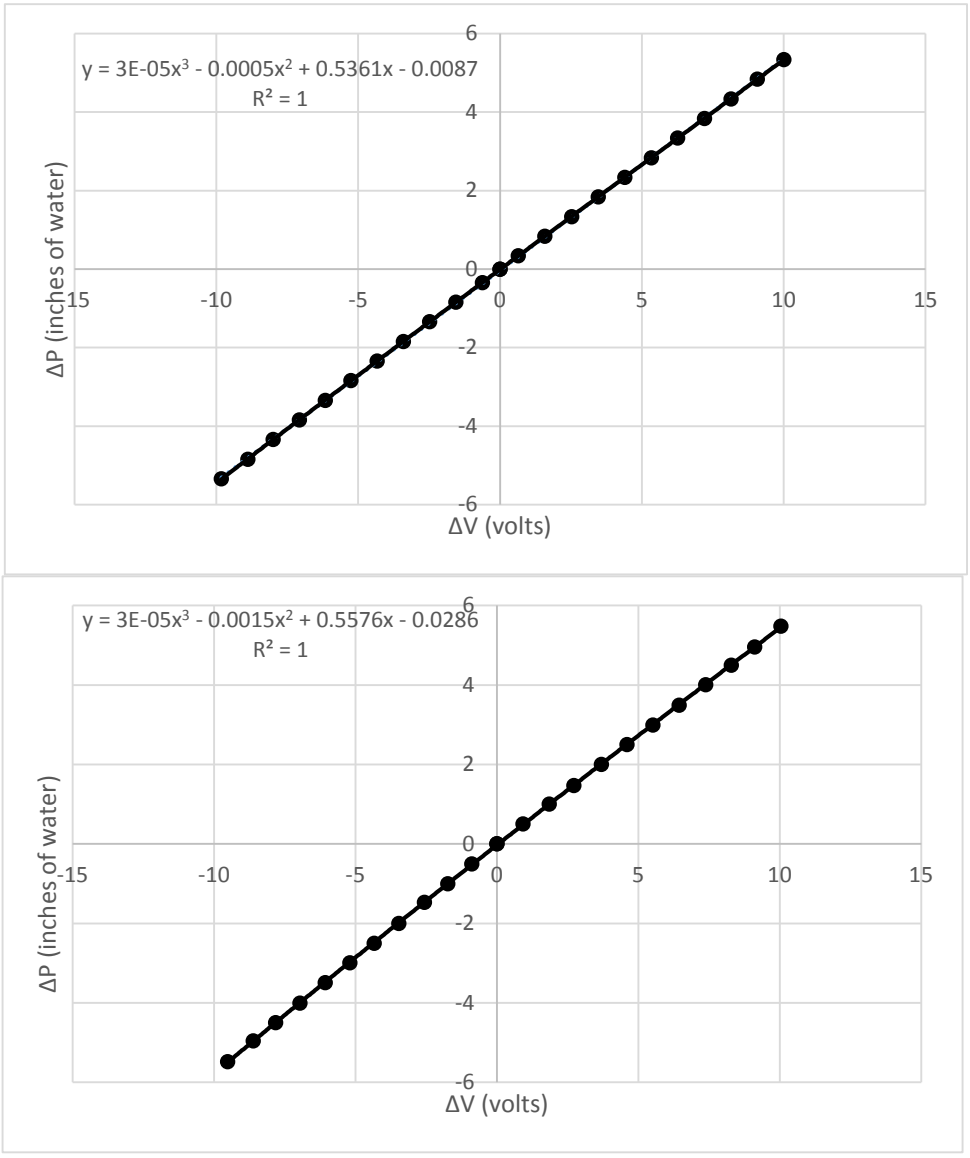

Figure 4-9: Calibration curves for Transducer 1 (top) and Transducer 2 (bottom)

4.3.2. Manometer

Manometers are simple devices based on the principle of changes in fluid elevation due to hydrostatic pressure difference. They are used in the present study in calibration of

various instruments (hot wire and transducers). Two types of manometers are used, which are described below.

4.3.2.1. U-Tube Micro-Manometer

A Dwyer Microtector Model 1430 Electronic Point Gage is a U-tube manometer used to measure pressure differences ranging 0-2 inches of water (0-500Pa). The manometer gage fluid is a mixture of distilled water and Dwyer A126 fluorescein liquid. As shown in the Figure 4-10, the manometer is equipped with a NIST traceable micrometer which is mounted on one of the U-tube legs. It reads half of the displaced pressure. This manometer has an in-built circuitry which is used to improve repeatability and resolution. When the Microtector point comes in contact with the gage fluid, the circuit is completed and a D.C. signal is generated which can be read on the front panel ammeter.

Errors in Measurement: Although an accuracy of ± 0.00025 inches water is given by the manufacturer, after experimental use the accuracy of the manometer is recommended to be ± 0.001 inches of water (±0.25 Pa) [54]. Also, the temperature must be noted while taking measurements since the manometer gage fluid is designed to operate at 277 K

Figure 4-10: Dwyer micro-manometer

(4˚C). Therefore at room temperature of 298 K (25˚C), the density variation may result in an error of approximately 0.6%.

4.3.2.2. Inclined Manometer

The inclined manometer (Figure 4-11) is used to measure pressure differences over the range 0-6 inches of water (0-1500 Pa). The manometer model 246 used is built by Dwyer Co. and contains the Dwyer red gage oil of specific gravity 1.0. If a gage oil with different specific gravity is used then appropriate modifications to the read value must be made. This manometer is used for calibration purposes and leakage flow mass flow rate measurements.

Errors in Measurement: Parallax error may occur while reading the scale on the manometer. For all the measurements made using this manometer, to maintain consistency the reading corresponding to the location of midpoint between upper end and lower end of meniscus is chosen. The manometer has a reported accuracy of ±0.01 inches of water (±2.5 Pa).

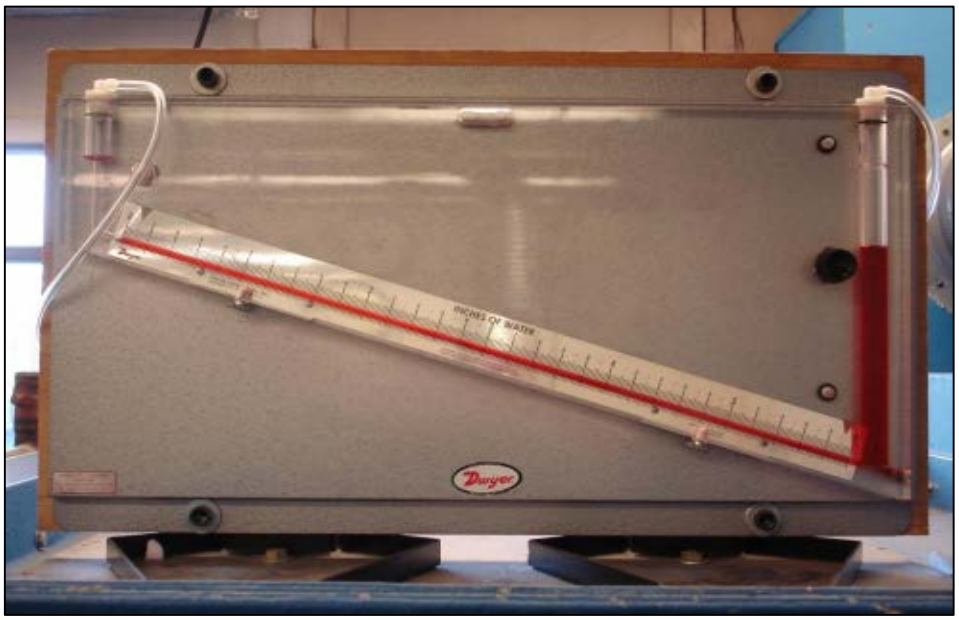

Figure 4-11: Dwyer inclined manometer

4.3.3. Static Pressure Taps, Total Pressure Probes, Pitot-Static Probes

The instruments described in the preceding sections are different ways to measure the pressure during the experiment. They measure the pressure that is sensed by total pressure tubes, Pitot-static tubes and static pressure taps. All these pressure sensing probes and taps are used in the present study for the purpose of calibration of various instruments and qualification of the test facility. Description of the static pressure tap and Pitot static tube is given in Section 3.2.1.2 and Section 4.1.2, respectively. The total pressure tube also works on the same principle as the total pressure conduit in a Pitot-static tube. The choice and design of these pressure sensors are based on the recommendations of Goldstein [60] and Schetz and Fuhs [67]. The main sources of error while using the total pressure sensors can be from the misalignment of the probe (small error for incidence angles up to 20˚ for square tipped probes), turbulence causing rise in indicated mean total pressure (although in the present study U_{rms} is about 11% of mean velocity so the associated error is very small), flow distortion due to wall proximity effect and viscous shear causing higher total pressure due to low Reynolds number effect (although for present study high probe radius based Reynolds number Re_r=2500 eliminates this error). The main sources of error while using the static pressure sensors (probes and taps) can be from the influence of probe tip region on the downstream static ports, blockage of flow path due to large probe body size, pressure sensing tap hole length-diameter ratio, tap nose geometry and burrs on tap/probe tip.

4.4. Temperature Measurement

Temperature measurement is an important part of the present experimental study as it is used to compute the approach flow temperature profile, passage thermal fields and endwall adiabatic effectiveness values. For this purpose, thermocouple is used as the instrument for measuring temperature. Thermocouples operate on the principle of the

"Seebeck Effect." When two wires of dissimilar metals are joined together to form a junction and exposed to a common temperature, T_1 while the other end of both wires are exposed to temperature T_2, an electromotive force is generated which can be measured using a voltmeter. This is because of the different potentials created across dissimilar wires exposed to same temperature difference. The voltage read can be then related to the temperature of the unknown junction with the temperature of other reference junction known. This is the principle which thermocouples employ to measure the temperature. In the present study, the thermocouples used are exposed-to-air type, made of material Type E (chromel-constantan) with an allowable 3-1150 K temperature range, which is considered well within the required range for the present purpose. The reference junction is usually located in an ice bath making the reference temperature 0˚C. In the present study, the Agilent 34970A unit is used, which has its own cold junction compensation. It has a built-in voltage-to-temperature conversion based upon N.I.S.T. data from Burns et al. [74]. For the present study, where only temperature differences are being measured, this method is considered acceptable. However, for measurement of accurate absolute temperatures, this method may add large uncertainty. The choice of using the hardware's internal conversion functionality is considered adequate based on a prior calibration check performed on the Agilent 34970A unit by comparison with a precision mercury thermometer with the reported accuracy of 0.024˚C in ΔT and 0.1˚C in absolute temperature as suggested by Erickson [54]. It is ensured that every time the measurement is taken, a low value of NPLC (number of power line cycles) in the Agilent unit is chosen (equal to 0.02) for a faster measurement rate.

Errors in Measurement: One of the problems associated with thermocouple is the small voltage output (usually in few millivolts per ˚C) which makes noise in the signal affect the

accuracy. A poorly welded or soldered junction of an exposed thermocouple probe may also cause error in measurement. Therefore, it is necessary to check the tip of the probe before use for any damage or external particle contamination to the integrity of the electrical junction. Introduction of thermocouple in the flow may cause slight thermal disruption especially conduction losses through the wire at the endwall, although the outer sheath diameter is smaller than 0.32 cm, which makes this disruption insignificant.

4.5. Flow Rate Measurement

Another important requirement of the experiment is to monitor the mass flow rate of leakage flow. For metering the flow, a Meriam Instruments Laminar Flow Meter (Model 50MC2-4) is used. It is installed in the supply line of the leakage flow to the leakage plenum chamber as discussed in Section 3.1.1.3. It works on the principle of volumetric flow rate of laminar flow being directly proportional to pressure drop (Poiseuille flow). The flow meter has pressure taps located at the inlet and exit for measuring the pressure drop across the meter. Flow is passed through several capillary elements within the flow meter in order to make the flow more constrained and laminar. Practically, the flow doesn't have ideal laminar characteristics (non-linearity due to additional pressure drop mainly caused by entrance effects) as a result of which the flow rate is expressed as a quadratic function of ΔP instead of linear variation as one would expect in an ideal laminar Poiseuille flow.

The laminar flow meter used in the present study is calibrated against a National Institute of Standards and Technology (NIST) traceable master flowmeter by the manufacturer. The reported calibration accuracy of the flow metering device is ±0.72%. Calibration constants are provided by the manufacturer for the model used. It should be noted here that the calibration is standardized to an equivalent dry gas flow rate at 70˚F (21.1˚C) and 101.3 kPa. Therefore the expression for volumetric flow rate must be adjusted according

to experiment test conditions of temperature, pressure and humidity. The expression to be used is given by the following equation:

$$Q = (50.0651\Delta P - 0.0692834\Delta P^2)\frac{\mu_{std}}{\mu_f}\frac{P_f}{P_{std}} \qquad \text{Eq. 4-16}$$

where

Q = Volumetric flow rate (ft^3/min)
ΔP = Pressure drop across the flow meter (inches of H_2O)
μ_{std} = Dynamic viscosity of air at 70˚F
μ_f = Dynamic viscosity of air at test temperature and relative humidity
$\frac{P_f}{P_{std}}$ = Pressure correction factor, read from manufacturer's table [75]

The viscosity μ_f is based on the conditions of fluid during the experiment which takes into account the effects of temperature and humidity. A HH311 Humidity Temperature Meter sold by Omega Engineering Inc. is used to measure the temperature and relative humidity. The quantity $\frac{P_f}{P_{std}}$ is a correction factor for accommodating pressure conditions during the test that are different from calibration conditions, although the correction value is very close to 1. The pressure drop across the meter is measured by connecting the static pressure taps on its inlet and exit to the inclined manometer using 0.25" plastic tubing.

Chapter 5 Qualification of Approach Flow

Before the measurement of the passage thermal fields and endwall adiabatic effectiveness, it is essential to qualify the approach flow entering the test section. This includes matching the blade static pressure profile for both passages of the cascade, measuring inlet plane velocity distribution, determination of the Reynolds number, the turbulence characteristics of the approach flow and development of an engine representative temperature profile. This chapter describes the procedure and the results obtained and gives a detailed discussion of the various approach flow characteristics.

5.1. Blade Static Pressure Profile

The first step towards the qualification of the approach flow is to match the blade static pressure profile for the upper and lower passages. The test section has only three blades and two passages bounded above and below with walls that can create differences in the pressure and velocity distributions of both the passages. This issue needs to be addressed by setting similar pressure profiles as it ensures equal amount of flow going into both passages. The static pressure taps on the suction and pressure surfaces of the blades (Section 3.2.1.2) measure the mid-span static pressure which is then used to compute pressure loss coefficients (C_p) with respect to pressure at the inlet of the blade assembly. It is given by the following equation:

$$C_p = \frac{P_s - P_{s,o}}{\frac{1}{2}\rho U_o^2} \qquad \text{Eq. 5-1}$$

Where P_s = Static pressure measured from blade static pressure tap
$P_{s,o}$ = Static pressured at inlet
$\frac{1}{2}\rho U_o^2$= Inlet velocity head

The inlet velocity head and static pressure are not directly obtained due to the high intensity and scales of turbulence which may make the aligning of the pitot-tube with the flow difficult resulting in erroneous values. By using conservation of mass flow rate from inlet to exit and assuming total pressure losses to be very low especially in the central part of the passage, these quantities can be calculated using the exit plane total pressure and static pressure measurements.

5.1.1. Procedure

The pressure profiles are set by adjusting the tailboards (discussed in Section 3.5.2) that strongly influence the velocity distributions in the two passages. The bleed slot (between the top blade's leading edge and top wall of the test section) is only slightly sealed so that a little gap remains for the approach flow boundary layer on top wall to bleed off. The procedure begins by first making the desired connections of the static pressure taps with the pressure transducers. The instrumentation used remains the same as discussed for pressure transducer calibration (Section 4.3.1). Pressure Tygon tubing is used to connect each pressure tap with two-way pneumatic valves (model TV-2S) made by Clippard Minimatics which are mounted on a switchboard. It is recommended that instead of measuring pressure with respect to atmosphere by the transducer, it should be measured with reference to a fixed (or equivalently variable) pressure source within the test facility. In this case, it was chosen to be a static pressure tap on the blade itself. This eliminates the uncertainty associated with measuring $\Delta P = P_s - P_{atm}$ because of the variability of P_{atm} and no link with the variations occurring within the test facility.

Measurement for each tap is taken for a period of 15 seconds and then averaged to get one value for each pressure tap. The switchboard mentioned above is a convenient way to switch from one pressure tap to another but care must be taken to ensure that only one

valve is actuated at any given point of time. Several trial runs are performed and tailboards are adjusted until matching pressure loss coefficients are obtained between the two passages.

5.1.2. Static Pressure Loss Coefficients Results

It turns out that matching flow distribution between both passages is quite sensitive to the positioning of the tailboards. Their slight movement may cause the pressure to deviate from one passage to another on an average by 20-30%. The suction sides of both passages were found to be particularly difficult to match. Initially, starting from x/C_{ax} = -0.6, the disagreement was significant, based on the pressure read from a few selected taps. The C_p values on the suction side of center blade were quite susceptible to changes in the longer tailboard which was more frequently adjusted than the shorter tailboard. The pressure side was overall more convenient with less sensitivity to tailboard position but

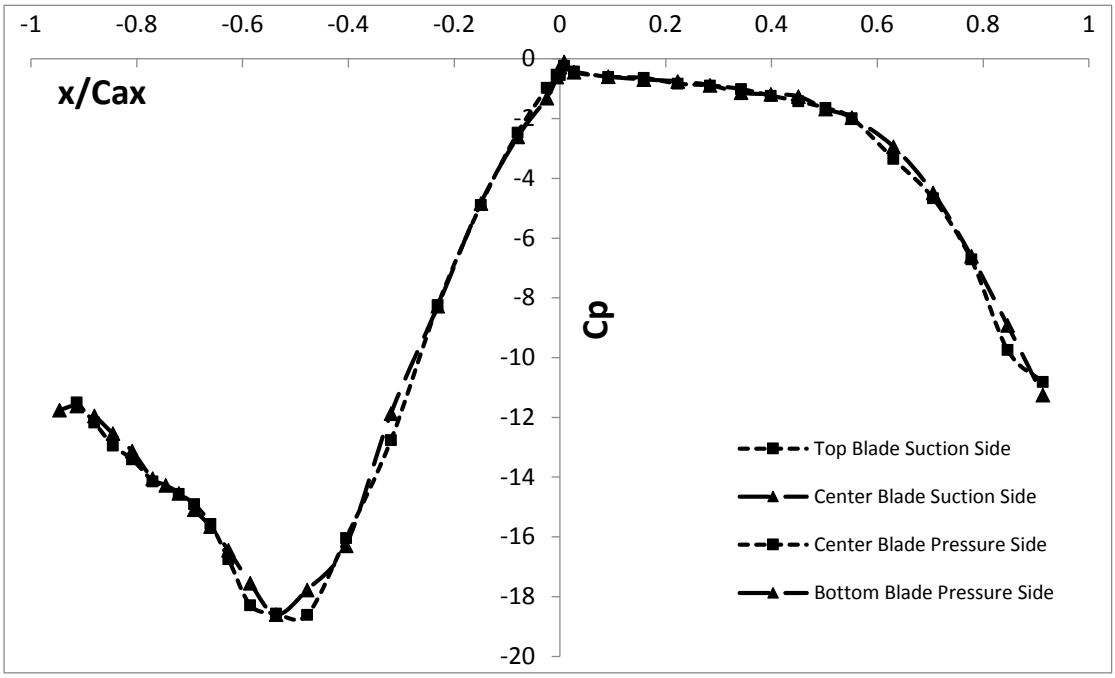

Figure 5-1: Blade mid-span static pressure profile for both passages

more dependent on suction side pressure distribution. A very small gap between the longer tailboard and the wall on which it rested was formed due to frequent moving of the

tailboard. This created a wall jet with cooler atmospheric air at higher pressure shooting into the passage through this gap where low pressure existed due to high velocity. This leakage into the test section is not significant to impact the pressure profiles but, as it was found later after taking endwall adiabatic effectiveness values, it caused the region of the endwall near the tailboard and downstream of the trailing edge to be slightly cooler (due to ingression of cooler atmospheric air). However, since the region affected is not of interest, this wall jet may be tolerated.

The final profiles obtained are shown in Figure 5-1. Top passage corresponds to the 'top blade suction side' and 'center blade pressure side'. The bottom passage corresponds to the 'center blade suction side' and 'bottom blade pressure side'. The suction side and pressure side are plotted on the left and right sides of the figure, respectively. Overall, both the pressure side and suction side agree quite well from one passage to another. However, some differences exist around x/C_{ax}= -0.5 on the suction side and on the trailing end of pressure side around x/C_{ax}=0.85, which are considered satisfactory with an understanding that the flow characteristics may not be completely similar for the two passages. The pressure loss profile not only establishes the periodicity of the flow entering both the passages, but also points to some important characteristics of the cascade. As expected, higher pressures are observed on the pressure side than on the suction side at any given axial location (x/C_{ax}) indicating the existence of a cross-stream pressure gradient within the passage. On the suction side, the flow undergoes strong acceleration (till x/C_{ax}~0.45) marked by a steep drop of C_p (indicating a drop in static pressure). In regions from x/C_{ax}~0.45 until the trailing end, the static pressure is recovered as shown by the increasing C_p values. These trends indicate the adverse or favorable pressure gradients occurring within the passage that cause the thickening or thinning of

the boundary layers respectively. On the other hand, the pressure side pressure profile is less steep indicating that the pressure drops at a much slower rate resulting in lower (and more uniform) pressure gradients, although the region from x/C_{ax}~0.6 until the trailing end experiences a steeper drop in pressure.

5.2. Entrance Flow Conditions

5.2.1. Approach Flow Velocity and Turbulence Characteristics

It is essential to characterize the approach flow entering the passage in terms of mean velocity, turbulence intensity and length scales of turbulence. These data can be used as inlet conditions if a related computational study is performed for this test facility. The procedure and the results for the evaluation of these characteristics are discussed in the following sections.

5.2.1.1. Inlet Plane Velocity and Turbulence Level Distribution

Measurements are taken at the inlet plane of the test section (x/C_{ax} = -0.72) using hot wire anemometry to compute the mean velocity and turbulence intensity plots. The instrumentation and the data acquisition system is discussed in the hot wire anemometry Section 4.1.1. A total of 224 measurement data points are chosen within the inlet plane with higher concentration of points near the endwall. At each data point, the velocity signal is captured for a period of 40 seconds at a frequency of 200 Hz (using the Agilent 34970A) which is considered adequate for capturing of mean velocity and turbulence intensity. It should be noted that the velocity signal captured at this frequency is not sufficient to generate the energy density spectrum; instead a much higher frequency is needed so that most of the fluctuation frequencies may be recorded. The post-processing of the data is done using Tecplot360 software.

The turbulence level, that is the root mean square velocity fluctuation, is calculated using:

$$U_{rms} = \sqrt{\frac{1}{N}\sum_{t=1}^{N}(u(t) - \overline{U})^2}$$

$$\overline{U} = \frac{1}{N}\sum_{t=1}^{N} u(t)$$

The results for the mean velocity distribution and root mean square fluctuations of velocity are plotted in Figure 5-2. The ordinate and abscissa are normalized distances over the pitch (P) and inlet passage width (W) with z/W=0 being the contoured endwall side.

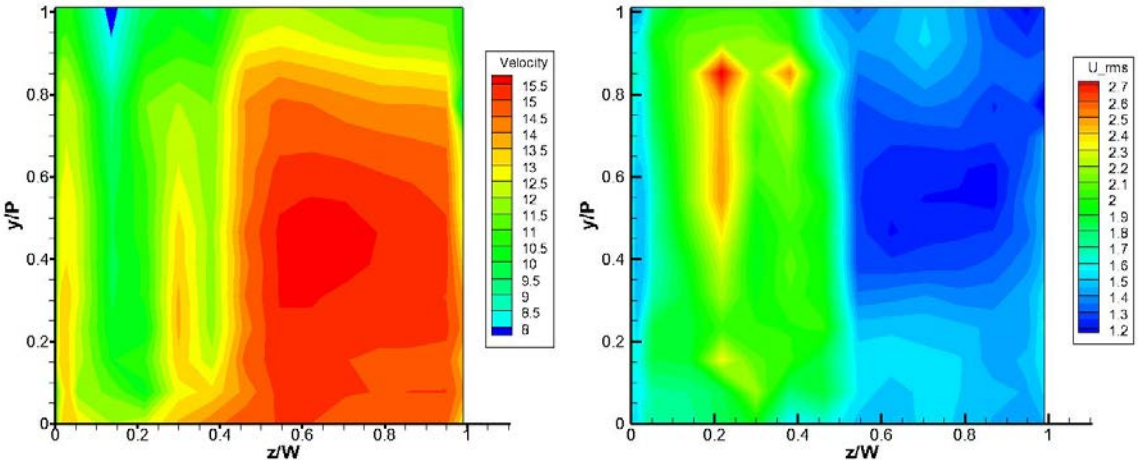

Figure 5-2: (Left) Inlet plane velocity distribution [m/s]; (Right) Inlet plane turbulence level distribution [m/s]

As can be seen in the inlet velocity distribution plot, there exists a region of lower velocities (z/W ~ 0 to 0.45) and a high velocity region (with core velocity ~15.5 m/s) from z/W ~ 0.45 to 1. This is due to the set-up conditions of the experiment where, while taking the measurements of the velocity, flow actually enters the upstream slot (the one used for creating the thermal profile) instead of flow being injected out of it. This is due to the slot flow fan running at a very low RPM generating a mass flow rate of the upstream slot flow

not sufficient to counter the mainstream flow entering into the slot. To support this hypothesis, the amount of ingression of mainstream flow into the slot is calculated. This is done by first calculating the mainstream mass flow rate based on exit plane velocity measurement for 'no leakage slot flow' case, followed by calculation of mass flow rate based on area averaged velocity as obtained in the velocity contour plot. It is found from the difference of the two calculations that there is around 12% ingression of the mainstream flow through the upstream slot which is quite significant. By performing scaling of the lower velocities based on these data and then again finding the area averaged inlet plane velocity, it is found that a more uniform velocity distribution is obtained with an average velocity of 15 m/s, which is closer to the high velocity region in the given velocity contour plot (Figure 5-2). This calculation shows that if the ingression of flow into upstream slot is eliminated (by running upstream slot flow fan at a higher RPM), the velocities will increase in the low velocity region and result in a more uniform velocity distribution over the entire plane with an average velocity of 15 m/s. This case was ensured for thermal field experiment set up where no ingression of flow occurs through the upstream slot. Based on this average velocity and blade's true chord length, a Reynolds number of 385,000 can be established. The Reynolds number is also found using Pitot-static tube measurement at the mid-pitch and mid-span position of the exit plane from which, using the exit-to-inlet area ratio, the inlet velocity is found. This is found consistent with the average velocity given above (~15 m/s).

In the inlet plane velocity distribution plot, near the outer endwall region (z/W~1), velocity gradients can be observed that extend up to z/W~0.8, resulting in a high velocity core region. This is due to the wall-damping effect caused by the large eddies that extend their effect further out into the flow. The thickness of the resulting "boundary layer" is found to

be comparable with the large eddy length scale (~8 cm). This “boundary layer” effect is unavoidable, given the large scales of turbulence in this flow. Also, regions of relatively lower velocities can be seen near the pressure side of the passage (y/P~1) due to the upstream effect from the stagnation zones of the blades.

In the turbulence level plot (root mean square velocity distribution), the vortex shedding from the resistance heaters results in the higher values in the region within z/W~ 0.05 to 0.5. The turbulence intensity of the approach flow is computed as 11% based on an average u_{rms} (area-averaged over the inlet plane) and the u_{mean} (based on the discussion above). It may be expected that by the time the flow reaches the blade passage entrance, most of the vorticity shed from the heaters is diffused, resulting in a more uniform turbulent flow. However, higher turbulence levels may be expected near the endwall region (z/W=0).

5.2.1.2. Energy Density Spectrum and Turbulence Length Scales

The characterization of turbulent flow only in terms of turbulence level may not be sufficient, especially for the flow exiting a combustor which contains large eddy length scales. Therefore, in order to compute the length scales of turbulence, the velocity signal is measured at a high frequency (10 kHz) for a period of 60 seconds using the Agilent 34411A unit, according to the procedure mentioned in Sections 4.2.2 and 4.2.3. The equations used are also described in those sections.

The energy density spectrum obtained is shown in Figure 5-3. The length scales namely integral length scale (Λ), energy length scale (Lu) and Taylor microscale (λ) are then computed. The various approach flow characteristics are given in Table 5-1. The spectrum gives information about the distribution of turbulence kinetic energy among various fluctuation frequencies which are essentially an indication of eddies contained within the flow. The ‘energy cascade’ can also be observed. Smaller eddies are affected by the

strain-rate field of larger eddies; as a result, vorticity of smaller eddies increases with an increase in their energy with a decrease in the energy of the larger eddies. Therefore, there is a continuous flux of energy from one tier of eddies to another. For large eddies, the spectrum is not universal because these eddies are influenced by geometry dependent mean flow. Smaller eddies on the other hand may approach isotropy because they are not affected by mean shear and depend only on the energy dissipation rate (equivalent to energy supply rate of the spectrum) and fluid viscosity. There exists an 'inertial subrange' within this energy cascade. The Kolmogorov spectrum law is also plotted on the same graph to show the 'inertial subrange' region. Its existence is also confirmed through the criteria given by Hinze [69] which states that $Re_{Lu}^{3/8}$ >>>1 and $Re_{\lambda}^{3/4}$ >>>1 for the inertial subrange to exist.

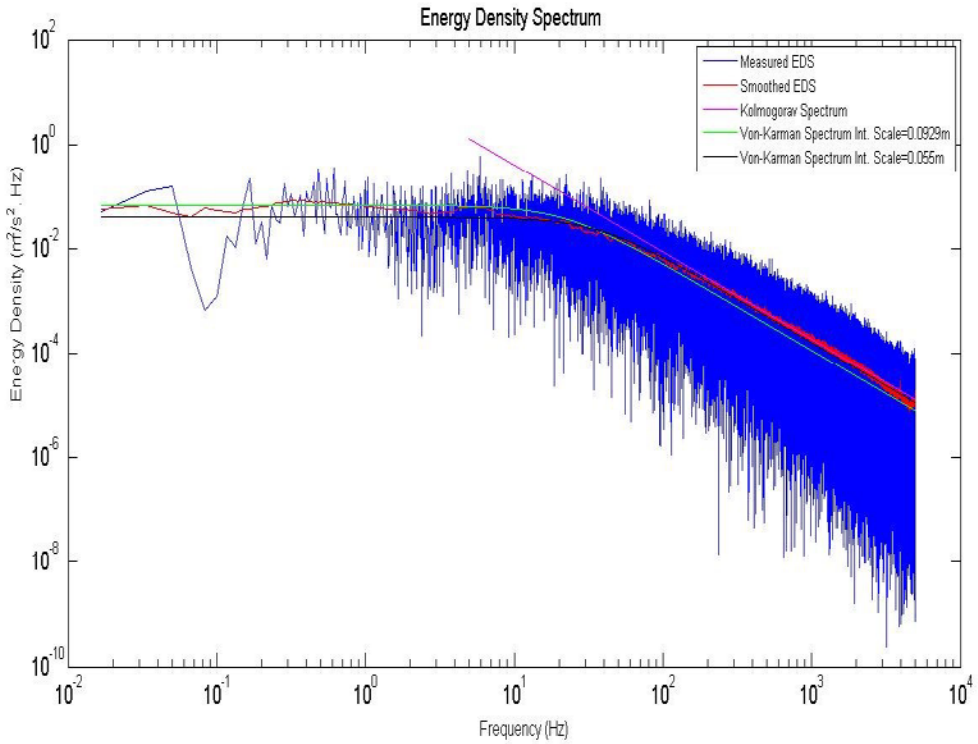

Figure 5-3: Energy density spectrum

The determination of integral length scale is done through the low frequency region where $w \to 0$. However, the uncertainty associated with it can be high due to the presence of very few data points in this region. To demonstrate this, the von Karman interpolation law is used with two different values of integral length scale as shown on the plot (0.0929m and 0.055m). The one with higher integral length scale shows good agreement with the measured EDS in the low frequency region but tends to deviate in the larger frequency region. Since more data points lie in the larger frequency region, the curve showing a better fit in that region can be supposed to be a more accurate fit. Therefore, the curve with lower integral length scale is considered a better approximation. This points to the fact that the actual integral length scale may be lower than the one (0.0929 m) calculated directly from the formula (Eq. 4-13). Therefore, instead of presenting a single value of Λ, an expected range is proposed as given in Table 5-1. As can be seen from the table, both energy and integral length scales indicate the presence of large eddy length scales within the flow.

Table 5-1: Approach flow characteristics

Bulk Inlet Flow Properties		**Turbulence Characteristics**	
U_{mean} [m/s]	15	Λ [m]	0.055 – 0.0929
u_{rms} [m/s]	1.63	Lu [m]	0.104
Tu	11%	λ [m]	0.0032
Re_c	385,000	ε [m^2/s^3]	77.85

5.2.2. Approach Flow Temperature Profile

The approach flow temperature distribution is not uniform; instead there exists a temperature profile extending from the endwall up to the mid-span location. This condition is required to simulate an engine representative temperature profile of the flow leaving the combustor in an actual gas turbine. The apparatus for generating the desired temperature

profile is discussed in Section 3.4. The temperature distribution within the profile is presented as a dimensionless temperature given by:

$$\theta = \frac{T_z - T_M}{T_w - T_M} \qquad \text{Eq. 5-2}$$

where,

T_z = Temperature measured by traversing thermocouple in a direction away from wall
T_M = Mainstream temperature at mid-span (at the inlet axial location)
T_w = Temperature at the endwall

The temperature distribution is measured right at the exit of the leakage flow slot (x/C_{ax} = -0.12) as shown in Figure 5-4. The temperature profile obtained is from the combined effect of upstream coolant and the leakage low. The temperature profiles are generated for each of the cases of MFR 0.5%, 1.0% and 1.5% so that the heating of the leakage slot flow can be set in order to obtain same temperature profile for all the cases since identical approach flow conditions are desired for all the test cases.

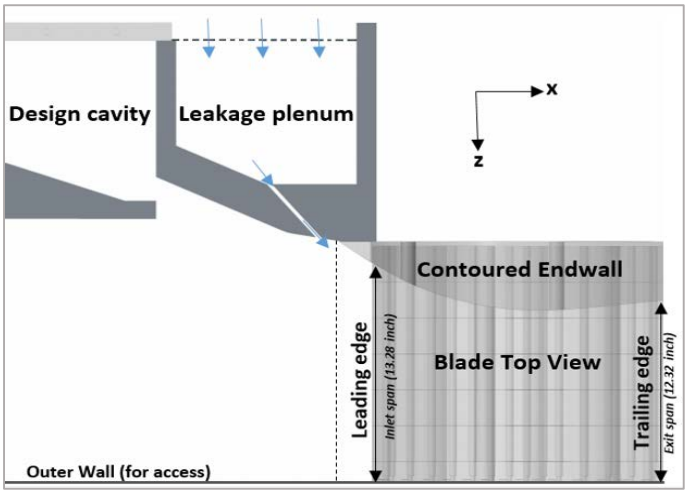

Figure 5-4: Location of approach flow temperature profile measurement (shown with dashed line upstream of leading edge)

The procedure involves several iterations in order to adjust the heating of the upstream slot flow and the leakage slot flow to obtain the desired temperature profile. The final profiles are shown in Figure 5-5. The ordinate is the normalized z coordinate (over the inlet span) and the abscissa is the dimensionless temperature given in the equation above (Eq. 5-2). The near-wall temperature gradient is close to zero for all the cases given the adiabatic conditions of the wall. A slight 'bump' in the profile around z/S~0.15 to 0.3 is

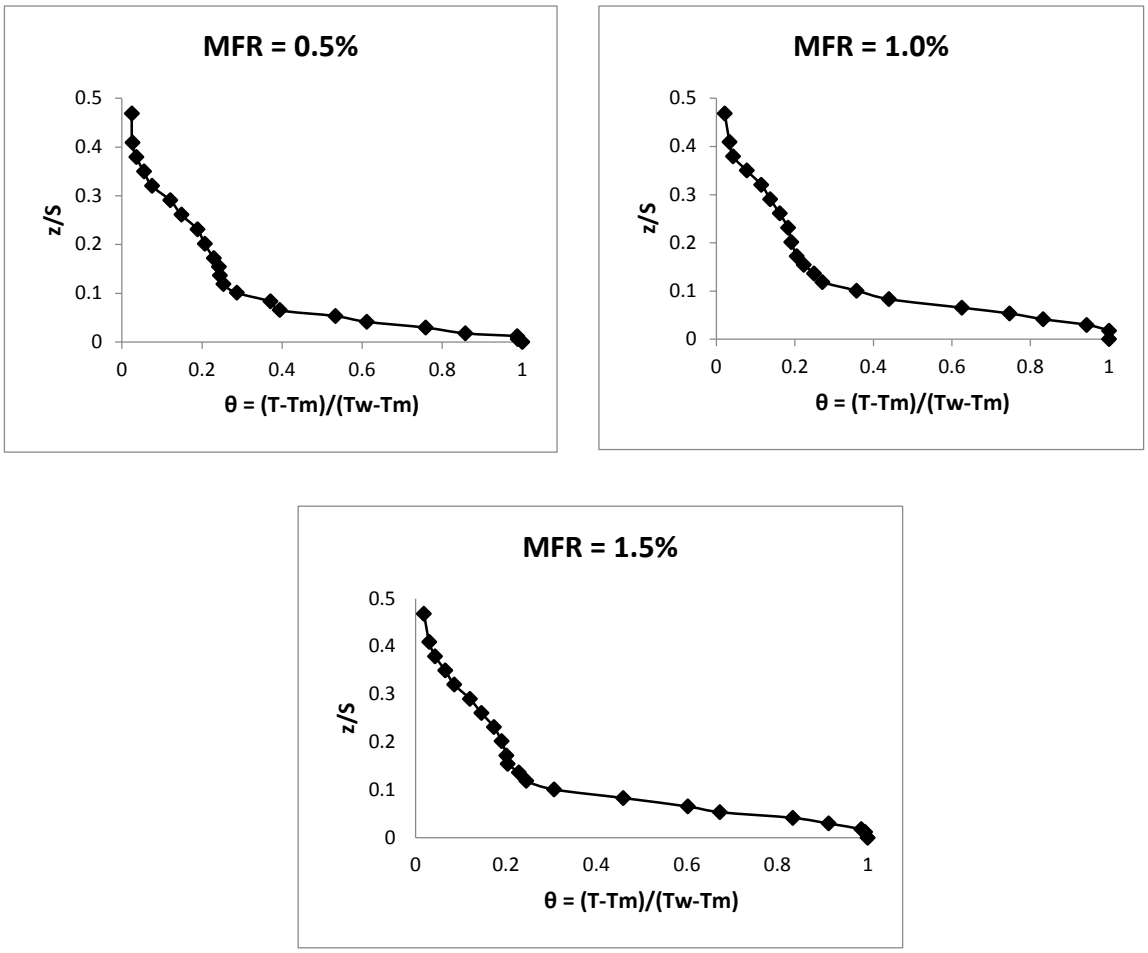

Figure 5-5: Approach flow temperature distribution for MFR 0.5%, 1.0% and 1.5%

attributed to the heating by the upstream resistance heaters. The profile extends until the mid-span as desired. While running the tests case with different MFRs, leakage slot flow heating is set to obtain these temperature distributions in the approach flow.

Chapter 6 Experimental Procedure

After the qualification of the approach flow to the test section, it is now important to discuss the experimental procedure used for measuring the passage thermal fields and endwall adiabatic effectiveness. This chapter describes the background theory and concepts on which these measurements are based and their utility to the overall gas turbine secondary flow knowledge.

6.1. Stator Cascade: Passage Thermal Fields

6.1.1. Background

One of the most complex aspects of a gas turbine is the flow field that exists within the turbine passage. Insufficient knowledge about the flow characteristics cause difficulties in developing methods to protect the endwall region from the extremely hot core gases. The ability to understand this complex flow field is an important step in addressing the issue of endwall film cooling. Measuring the thermal field within the passage is one of the methods to achieve this aim. Analyzing the non-dimensionalized temperature field can give an indication of the mixing and migration of the coolant flow (the upstream slot coolant and leakage slot coolant) and the mainstream flow. In the present study, the coolant flow is at a higher temperature than the mainstream flow using the temperature difference as merely a marker of the migration aspects of the various flows within the passage. Once these flows mix, a dimensionless temperature can be defined to quantify the migration given by:

$$\theta = \frac{T_{x,y,z} - T_O}{T_L - T_O} \qquad \text{Eq. 6-1}$$

where

$T_{x,y,z}$ = Temperature measured at location x, y, z
T_O = Mainstream temperature of approach flow
T_L = Leakage flow temperature (average temperature of flow within the leakage flow plenum)

Since temperatures are measured using thermocouples, given the thermal diffusion, viscous dissipation and conduction effects from the thermocouple probe tip, measured temperature is essentially the '*recovery'* temperature:

$$r = \frac{T_R - T_s}{T_T - T_s}$$

T_R is the measured or 'recovery' temperature, T_S is the static temperature and T_T is the total temperature at the point of measurement. The measured temperature will therefore lie between static temperature and stagnation temperature. The values plotted are essentially dimensionless recovery temperature (with recovery factor ~ 0.68 for thermocouple oriented perpendicular to flow direction). For low velocities, this effect is very small.

Note that the thermal field is normalized over a temperature difference between the leakage flow temperature and the mainstream flow temperature. This is done so that the θ values obtained can be analyzed by referencing them to the leakage flow's contribution as the coolant. The higher the value of θ in a particular region, the closer is the temperature of fluid at that point to the leakage flow temperature. Since differences in temperature (ΔT) are being measured, therefore uncertainty values are low. An uncertainty of $\delta\theta = \pm 0.014$ (based on the partial derivative method by Moffat [76]) is suggested due to the following reasons: variability in atmospheric conditions during the time of conducting the

measurement, unsteadiness in T_L-T_O during the process of taking measurement, insufficient averaging time of temperature and calibration errors of various units of data acquisition system.

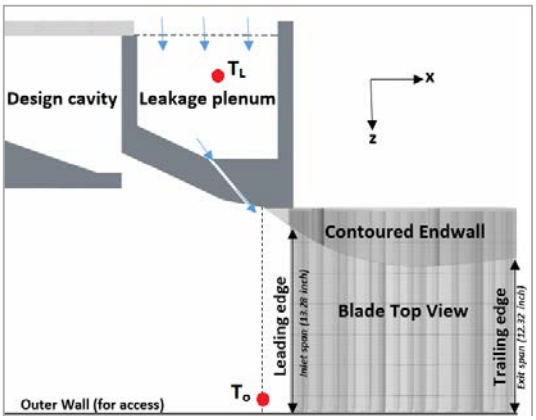

Figure 6-1: Measurement location (shown in red) of leakage flow temperature (T_L) and mainstream flow temperature (T_O)

6.1.2. Procedure

The passage thermal fields are measured for three mass flow rates of leakage, MFR (leakage mass flow rate to mainstream mass flow rate ratio) of 0.5%, 1.0% and 1.5%. The leakage flow rate can be monitored by the laminar flow meter (Section 4.5). Note that these MFR may carry an uncertainty value of 6%. At each MFR value, five planes (x/C_{ax} = -0.104, 0, 0.317, 0.612, 0.990) are selected within the passage to cover the entire passage starting slightly upstream of the leading edge plane and until the trailing edge of the blades as shown in Figure 6-2. In each plane, several measurement locations are chosen to yield detailed capturing of the mixing process. More measurement data points are selected for the upstream planes (Plane 1, 2 and 3) since these regions are critical because of the significant impact of secondary flow structures on the coolant flow. Also, greater concentration of points can be seen near the endwall and the suction side. It should be noted here that measurements are taken in the top passage only since the passages are checked for periodicity by adjusting the blade static pressure profiles.

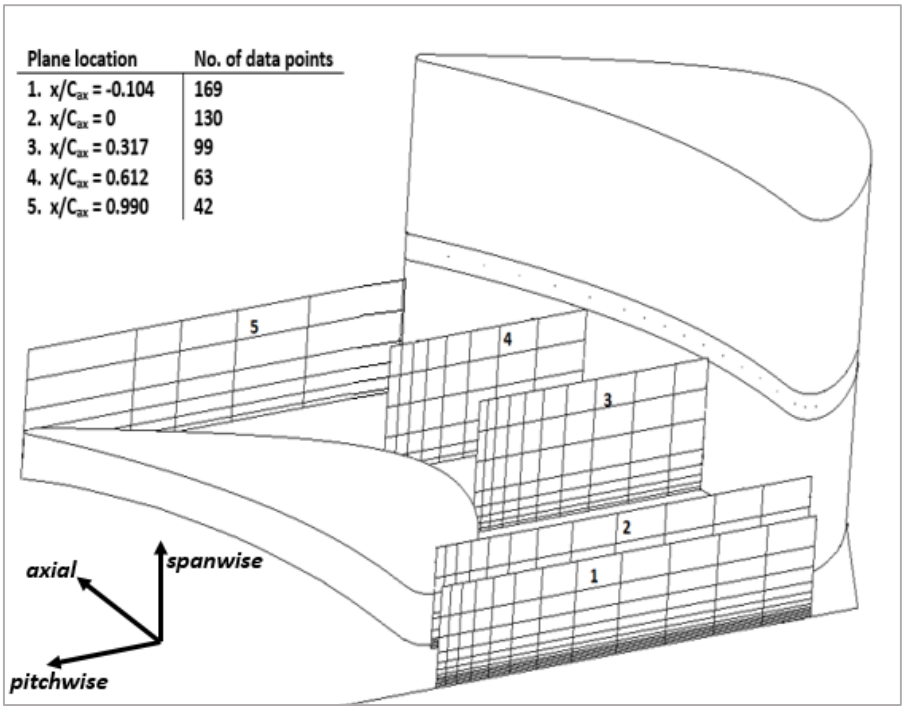

Figure 6-2: Location of measurement planes for passage thermal field measurement

Each run of experiment begins by turning on the wind tunnel fans, leakage flow and upstream slot flow fans, and the heaters. The power from the heaters is adjusted depending on the MFR case being tested. For example, for the MFR 1.0% case, to acquire the desired approach flow temperature profile, the inlet thermal profile slot heater is set at 75% of its maximum power while leakage flow heater is set at 90% of its maximum power (750 Watts) heating the leakage flow 7-9˚C above mainstream flow temperature (~26˚C). Each resistance heater's power (in the flow path) is also set accordingly to what was obtained during the approach flow qualification (discussed in Section 5.2.2). They are left running for around two and a half hours for the flow conditions to reach steady state. Once the desired state is achieved, the thermocouple probe (Type E, chromel-constantan) is positioned using the automated traverse system with the data being acquired using Agilent 34970A unit. Each temperature measurement is carried out at 1 Hz frequency for a period of 20 seconds. The front panels and the movable hole panels on the flat endwall are also

positioned so that the probe is able to reach the desired location. The leakage flow temperature (T_L) is measured by means of a thermocouple placed within the leakage flow plenum inserted from the top wall of the test section. The approach flow temperature (T_O) is measured using a thermocouple placed slightly upstream of leading edge plane at mid-pitch and slightly away from mid-span location (Figure 6-1).

6.2. Stator Cascade: Endwall Adiabatic Effectiveness

6.2.1. Background

Assessing the cooling potential of the leakage flow and the upstream near-wall coolant flow over the endwall is of particular importance in this study. It is quantified by measuring 'endwall adiabatic effectiveness' which is essentially the passage thermal field (θ) (described in the previous section) measured *at* the endwall. It indicates the extent of coverage of the coolant over the endwall which is important because the endwall lies in the vicinity of the hot core gases in a gas turbine and needs to be protected. Evaluation of the adiabatic effectiveness can help analyze the behavior of coolant over the endwall in the presence of the given design and operational characteristics. The dimensionless form of the adiabatic effectiveness is evaluated using the following expression:

$$\eta_L = \frac{T_{x,y,z=0} - T_O}{T_L - T_O} \qquad \text{Eq. 6-2}$$

where

$T_{x,y,z=0}$ = Temperature measured at location at endwall (z=0)
T_O = Mainstream temperature of approach flow
T_L = Leakage flow temperature (average temperature of flow within the leakage flow plenum)

The term ‘adiabatic’ is used because there is no heat transfer at the endwall leading to a zero near-wall temperature gradient ($\frac{dT}{dy}_{(y=0)} = 0$). The choice of endwall as Medium Density Fiberboard with a low thermal conductivity ensures that this condition is achieved.

A higher value of $\boldsymbol{\eta}$ indicates better coolant coverage over the endwall whereas lower values of $\boldsymbol{\eta}$ show that the coolant is depleted from that region. These trends can be related to the secondary flow structures forming within the passage. In an ideal case, $\boldsymbol{\eta}$=1 shows the surface has been completely protected by the coolant film. Any decrease in the value points to the dispersion of coolant with the mainstream flow. It should be pointed out here that in the present study, since the mainstream flow is cooler than the leakage flow and the upstream near-wall coolant flow, the endwall surface will be hotter where the coolant has been able to protect the endwall more efficiently and vice-versa. Based on the effectiveness results, a gas turbine designer acquires knowledge about the regions of the

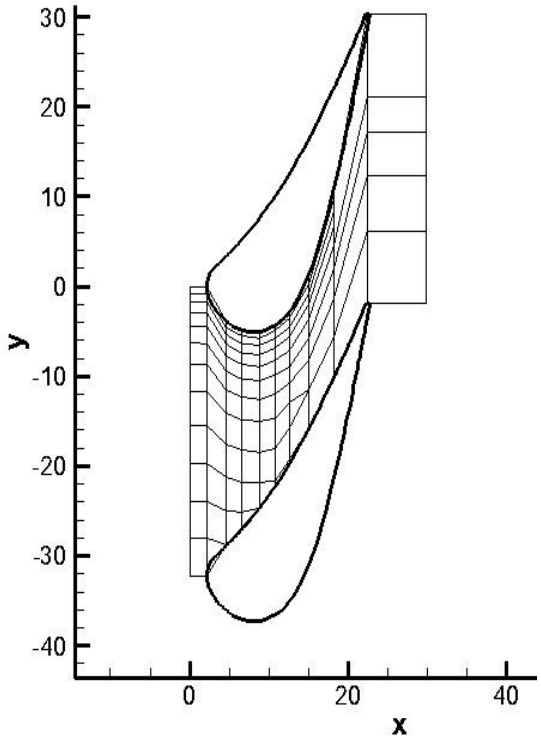

Figure 6-3: Endwall adiabatic effectiveness measurement locations (x and y axes in centimeters)

endwall that need special attention for protection from hot core gases and the extent of coolant coverage over the endwall, and hence develop a better design. The uncertainty associated with the effectiveness values remains the same as that for the passage thermal fields, $\delta\eta = \pm 0.014$.

6.2.2. Procedure

The procedure to measure the endwall effectiveness is essentially similar to that described above for measuring the passage thermal fields. It involves warming up of the test section and achieving the steady state of the wind tunnel, positioning the thermocouple probe (Type E, chromel-constantan) on the endwall and using the same data acquisition unit (Agilent 34970A) as in the case of thermal field measurement. The locations of measurement of T_L and T_O also remain the same.

As shown in Figure 6-3, a total of 113 measurement locations are chosen over the endwall with more points on the suction side of endwall-blade junction and the leading edge region. At each measurement location, the temperature is measured at a frequency of 1 Hz for a period of 20 seconds. Each set of measurement is taken for leakage to mainstream mass flow rate ratios of MFR 0.5%, 1.0% and 1.5%.

It is necessary to ensure that adiabatic conditions exist at the endwall surface. For this purpose, five locations over the endwall are randomly selected. At each location, the thermocouple probe is traversed over z=0.5 cm in steps of 0.05 cm and the results are plotted in terms of the same dimensionless θ. An isothermal zone (with zero or nearly zero temperature gradient) is observed within 1.0 mm of the endwall surface within which the adiabatic effectiveness measurements are taken.

6.3. Rotor Cascade: Leakage Flow Ejection Region

This section describes the procedure for measuring thermal fields within the leakage slot region of the "**Rotor Cascade"** test facility. The design of the leakage slot ahead of the rotor in a gas turbine is large. This region is prone to ingression of mainstream gases into the slot causing undesirable mixing processes and subsequent reduction of cooling effectiveness within the passage. Also, the manner of ejection of the leakage flow into the passage may alter the boundary layer of the approach flow, which in turn, may affect the strength and size of the secondary flow structures subsequently formed. Therefore, it is interesting to analyze the thermal fields in planes located *within* the leakage slot at different mass flow rates of leakage. These results when compared with those obtained for the *stator* cascade test facility can help in assessing the effect of the leakage slot geometry on the mixing phenomenon of leakage 'coolant' flow within the passage. The details of the "Rotor" experimental test facility and its flow characteristics are given in the Appendix. For a better understanding, it is recommended that these details be read first before going through the experimental procedure described in the following paragraphs.

Documentation of the leakage flow temperature distribution is achieved by thermal field measurements in the region where leakage flow is ejected, as shown in Figure 6-5. The endwall used in this study is referred to as the 'dolphin nose' contoured endwall (details described in Appendix). Leakage to mainstream mass flow rate ratios of MFR 0%, 0.5%, 1.5% are considered. The baseline case of MFR 0% (with only upstream near-wall coolant) is added to appreciate the effects of absence of leakage flow. Four measurement planes are chosen such that the entire region from the suction side to the pressure side is covered. Each plane contains 48 measurement locations with more points concentrated near the endwall (z/S = 0). The dimensionless temperature field and the root mean square

deviation of temperature (a measure of unsteadiness) at each measurement location are given by:

$$\theta = 1 - \frac{T_{x,y,z} - T_O}{T_L - T_O} \quad \text{Eq. 6-3}$$

$$RMS_\theta = \frac{RMS_{T_{x,y,z}}}{T_L - T_O} \quad \text{Eq. 6-4}$$

where

$T_{x,y,z}$ = Temperature at measurement location x,y,z

T_L = Average leakage flow temperature measured just after the rim-seal gap (Figure 6-4)

T_O = Mainstream temperature (at mid-span and mid-pitch location upstream of leading edge plane)

$RMS_{T_{x,y,z}}$ = Root mean square temperature fluctuation at measurement location x,y,z

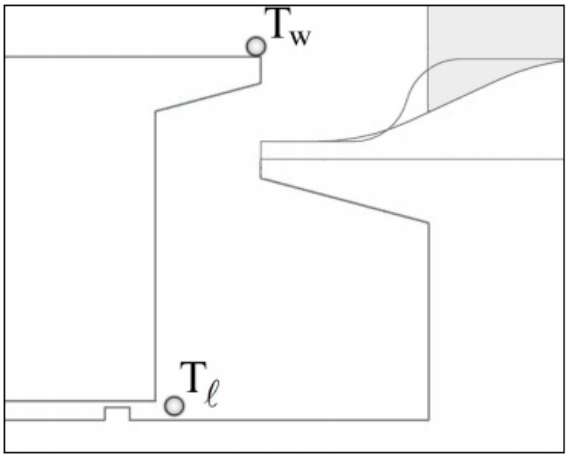

Figure 6-4: Measurement location of wall temperature, T_W and leakage flow temperature, T_L in the rotor cascade test facility

Regions with higher θ values have less coolant, indicating dominance of the hotter core gases. It should be noted that the 'coolant' is ~10˚C hotter than the mainstream flow and

that the temperature is merely a marker of mixing and migration of the ‘coolant’. The instrumentation used for measuring temperature is the same as used in the stator cascade test facility, i.e. Type-E thermocouple measuring temperature at 1 Hz for 20 seconds at each measurement location using the Agilent 34970A unit. Since differences in temperature (ΔT) are being measured, the associated uncertainties are low (close to 5%).

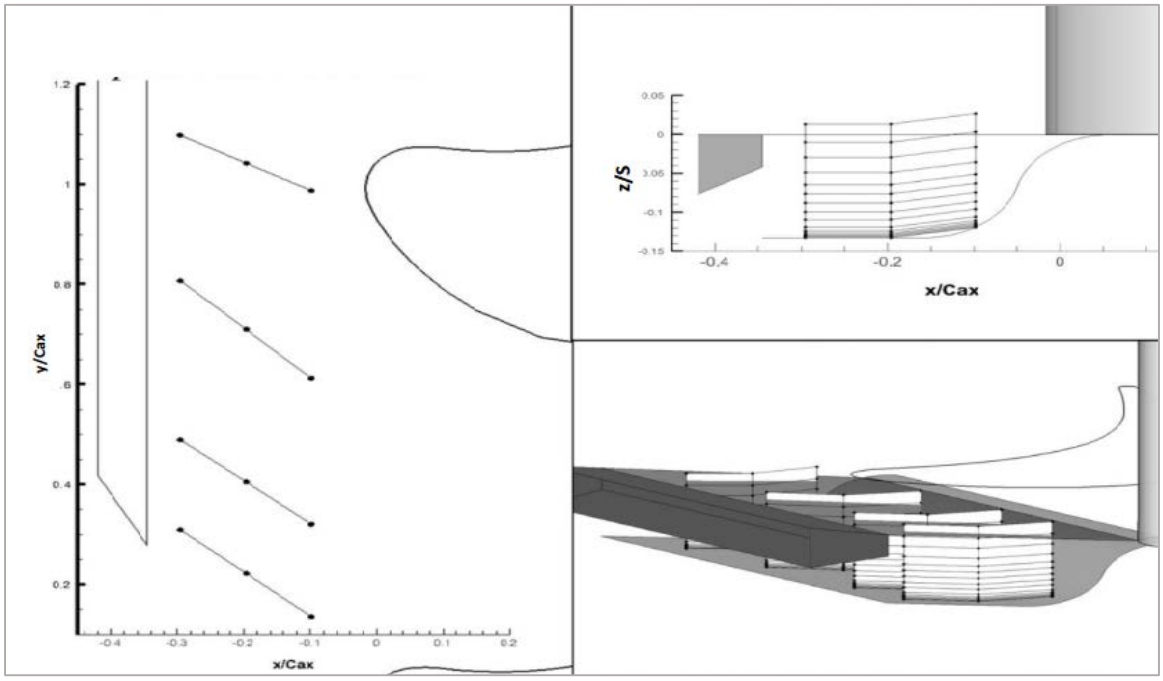

Figure 6-5: Measurement locations of planes within the ejection region of leakage flow from the leakage slot in rotor cascade test facility

Chapter 7 Stator Cascade: Results and Discussion

This chapter discusses the results obtained in the form of passage thermal fields and endwall adiabatic effectiveness values for the **stator cascade** test facility. It is important to first verify the adiabatic conditions of the endwall surface which is done in accordance with the procedure described in Section 6.2.2. Dimensionless temperature is plotted against endwall-normal distance as shown in Figure 7-1. An isothermal zone (with nearly zero temperature gradient) is observed within 1 mm of the endwall surface within which the adiabatic effectiveness measurements are taken.

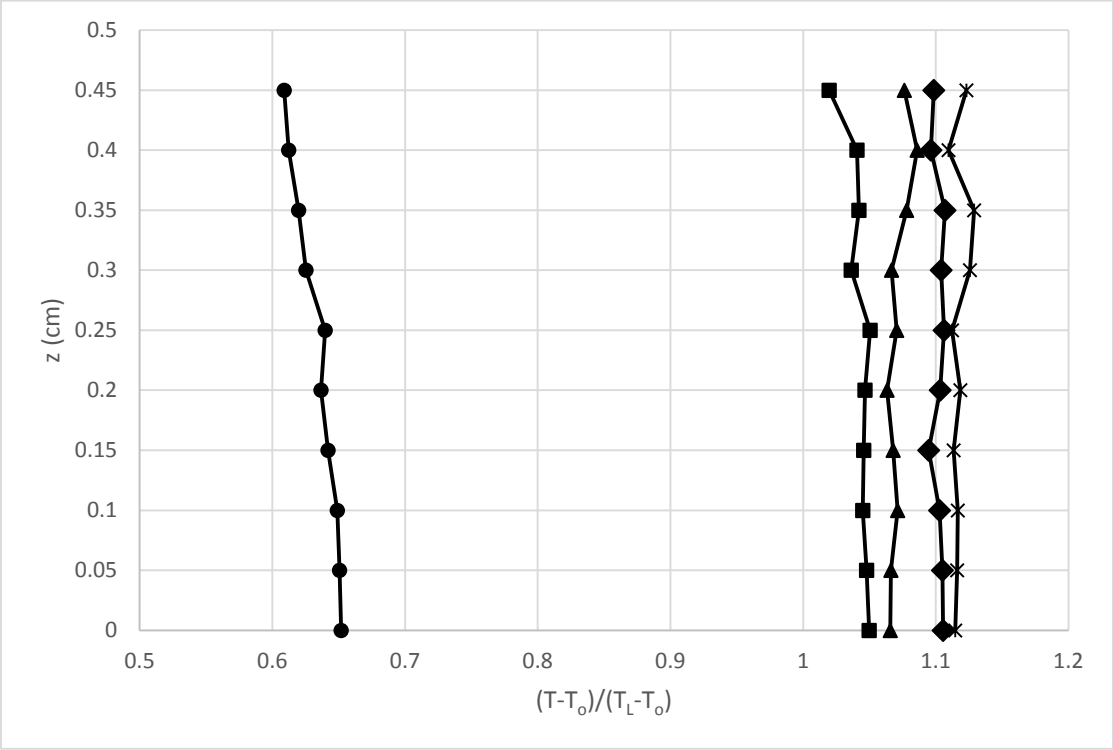

Figure 7-1: Endwall normal temperature profiles at randomly selected locations on endwall surface

7.1. Passage Thermal Fields

Results for the passage thermal fields are given in this section for three leakage to mass flow rate ratios (MFR) of 0.5%, 1.0% and 1.5%. The plotted values are based on the definition provided by Eq. 6-1 which normalizes the traversing probe's temperature with respect to the leakage flow temperature, T_L. It is important to analyze the results in this form as it points directly towards the utility of the leakage flow as a coolant and shows the mixing trends as observed for different mass flow rates of leakage.

The results are shown in Figure 7-2, Figure 7-3 and Figure 7-4. The abscissa is the normalized distance along the pitch with the right side of each plot representing the suction side and the left side representing the pressure side. The ordinate is the normalized distance along the spanwise direction with endwall at z/Inlet_Span=0.

It should be noted that the value of θ is greater than 1 at some locations for all the MFR cases. This is because at those locations the temperature sensed is more than the leakage flow temperature, caused by the heated fluid approaching the passage from the upstream slot. This upstream slot delivers coolant flow that is intended to simulate the combustor liner coolant. The upstream fluid and the leakage flow mix together with the mainstream flow to yield temperatures at certain spanwise locations that are greater than the assigned leakage flow temperature. It should also be noted that the plane upstream of leading edge (i.e. x/C_{ax}= -0.104) has non-uniform distribution along the pitchwise direction (from pressure side to suction side). It can be that some mainstream flow ingression into the leakage slot occurs due to high endwall static pressure at the blade stagnation regions. In addition to it, the flow seems to be already skewed due to the cross-stream pressure gradient that causes the emerging coolant from the slot to be swept towards the suction side. It can be expected that if the leakage slot were located further upstream, the impact

of this strong cross-stream pressure gradient would be lesser resulting in a more uniform distribution of coolant from the slot.

First let us consider the variations in the thermal fields as one moves downstream in the passage. The cross stream pressure gradient is evident marked by the coolant being washed towards the suction side from the pressure side resulting in higher θ values near the suction side. Going from plane x/C_{ax} = -0.104 to x/C_{ax} = 0, one sees that the coolant core size reduces indicating the mixing of coolant due to the stagnation region's secondary flow structures with major influence from the horseshoe vortex. Contouring of the endwall begins upstream of the stagnation zone that results in thinning of the approach flow boundary layer, hence weakening of secondary flow structures that form in this region. Nevertheless, the horseshoe vortex along with the leading edge corner vortices still form, a consequence of which is a reduction of the coolant core size, although the extent to which this happens varies from one MFR case to another. Moving further downstream, one sees that some of the coolant gets mixed out in the highly turbulent mainstream flow with most of the high θ core region vanishing. However, it is important to note that the coolant remains nearer the surface and covers the endwall surface for most of the passage, unlike the *rotor cascade* passage as will be seen in the next chapter. The leakage slot flow geometry enables this trend. Due to the thin geometry of the slot, the coolant is ejected with high momentum flux with a more 'focused' fluid stream. Also, with its exit aligned with the shape of the contoured endwall, coolant tends to remain nearer to the endwall surface due to the low injection angle. This corroborates the findings of Thrift et al. [43] for a similar turbine vane cascade.

For planes in the upstream locations, an ingression of mainstream flow (equivalently, the mixing out of coolant in that region) is observed near the suction side. As already

mentioned, due to the existence of endwall cross flows, the coolant is swept towards the suction side and an upwash is seen on the suction side wall of the blade. There is also present a downwash region slightly away from the suction side wall of the blade marked with the ingression of the mainstream flow. This indicates to the presence of a vortex possibly formed as a result of the upstream of horseshoe vortex. The formation of this vortex may cause rapid mixing of coolant as seen in the upstream planes. Once this happens in the leading edge, the effect persists for most of the passage as indicated by a similar trend up to plane $x/C_{ax} = 0.612$ for all the MFR cases. The existence of the suction side leg of the horseshoe vortex may also contribute to some of the mixing in this region, although this vortex is much smaller in size.

Now, comparing one MFR case with another, it can be observed that the coolant spread is greater in the case of MFR 1.0% as compared with other two cases. It is interesting to study these trends using the concept of mass flux ratio and momentum flux ratios of the leakage flow with respect to the mainstream flow. With the given thin geometry of the leakage slot, these flux ratios particularly the momentum flux ratio, are important considerations while analyzing the cases of various leakage mass flow rates. Also, the experiment uses the condition of passage flow to coolant flow density ratio of almost 1 (density variation of the two flows within 3%). However, in real gas turbines there is usually a significant difference in the density of the hot core flow and the cooler compressor air (usually with a coolant to core flow density ratio of 2). Therefore, the momentum flux ratio becomes a more indicative quantity while applying the experimental results to the actual gas turbine environment. The momentum flux ratio, I, and mass flux ratio, mfr, can be defined as follows:

$$I = \frac{\rho_c {v_c}^2}{\rho_m {v_m}^2} = MFR^2 \frac{{A_m}^2}{{A_c}^2} \frac{\rho_m}{\rho_c} \quad \text{Eq. 7-1}$$

$$mfr = \frac{\rho_c v_c}{\rho_m v_m} = MFR \frac{A_m}{A_c} \quad \text{Eq. 7-2}$$

where,

$\frac{v_c}{v_m}$ = Coolant to mainstream flow velocity ratio
$\frac{A_m}{A_c}$ = Ratio of mainstream flow exit area to leakage slot exit area (=102.2 for the test facility)
$\frac{\rho_m}{\rho_c}$ = Mainstream flow to coolant density ratio (~1.027 for the test conditions)

The ratios are presented in the following table:

Table 7-1: Velocity Ratio, Mass Flux Ratio and Momentum Flux Ratio

MFR	Velocity Ratio ($\frac{v_c}{v_m}$)	Mass Flux Ratio	Momentum Flux Ratio
0.5%	0.52	0.51	0.27
1.0%	1.05	1.02	1.07
1.5%	1.57	1.53	2.41

As seen in Table 7-1, the momentum flux ratio, I, increases at a rate that is more than the rate of increase of mass flux ratio, mfr, with given increase in MFR value. As a result, the MFR case of 1.5% has higher mass flux of leakage but with its much higher momentum flux of leakage (~2.2 times the momentum flux ratio in MFR 1.0% case), the coolant actually 'shoots' into the mainstream flow and mixes with it. This leads to lowered coolant coverage and spread at all axial locations as compared with the MFR 1.0% case. The lower θ values for the case of MFR of 0.5% are expected due to the lower mass and momentum flux of coolant (mass flux ratio half of MFR 1.0% case and momentum flux ratio one-fourth of MFR 1.0% case). The low momentum-fluid fed to the approach flow

boundary layer increases its thickness and results in stronger secondary flow structures, which cause a reduction in coolant spread seen in downstream parts of the passage.

7.2. Endwall Adiabatic Effectiveness

Results for the endwall adiabatic effectiveness are shown in Figure 7-5, Figure 7-6 and Figure 7-7. As with the passage thermal fields, some locations have η>1 that can be explained in a similar manner as done in the preceding section on passage thermal fields. Another point to be noted is the non-similar behavior seen in the stagnation regions of the blades which is a limitation of using a two passage cascade with only three blades. Also, it should be noticed that the suction side region upstream of the leading edge plane has higher effectiveness values, near unity as compared to about 0.5 immediately near the pressure side. As expected, the skewing of the flow caused by the varying pressure field from pressure side to suction side seems to be already happening upstream of the passage. Although the leakage slot has a slender geometry, some mainstream ingression into the slot results in further skewing of the coolant distribution as it is ejected out of the slot. This, combined with the impact of cross stream pressure gradient within the passage, causes an unequal distribution of coolant from the pressure to suction side in the upstream regions.

Within the passage, the coolant coverage is much more effective near the suction side due to the cross-stream pressure gradient from the pressure side to suction side. The pressure side has reduced coolant coverage which makes this region more sensitive to the hot mainstream fluid. With a thinner geometry of the leakage slot, the coolant stream shoots in a much more ‘focused’ manner onto the endwall surface resulting in the higher coolant spread. The contoured endwall provides acceleration to the flow providing momentum to counter the strong secondary flow structures and yield higher effectiveness

values even in the trailing edge region. In the middle regions of the passage for all the MFR cases, coolant coverage appears to reduce on the blade suction side-endwall corner (for example, for the MFR 0.5% case, effectiveness drops from 95% to 80%), which may be attributed to the suction side corner vortex or a wall vortex induced by passage vortex causing the coolant to mix out.

Now comparing one MFR case with another, for the MFR 0.5% the coolant coverage seems to break off to a large extent in the leading edge region of the passage. On the other hand, for the MFR 1.0 and 1.5% cases, coolant with higher momentum flux persists in this zone, hence less impact can be seen. Maximum coolant coverage is observed in the case of MFR of 1.0%. Using the concepts of mass and momentum flux ratios described in the preceding section, coolant in the MFR 1.5% case with its high momentum flux penetrates into the flow showing less efficient film cooling characteristics than the MFR 1.0% case. The MFR case of 0.5% results in quite a discontinuous coolant coverage due to its insufficient mass flux ratio and momentum flux ratio.

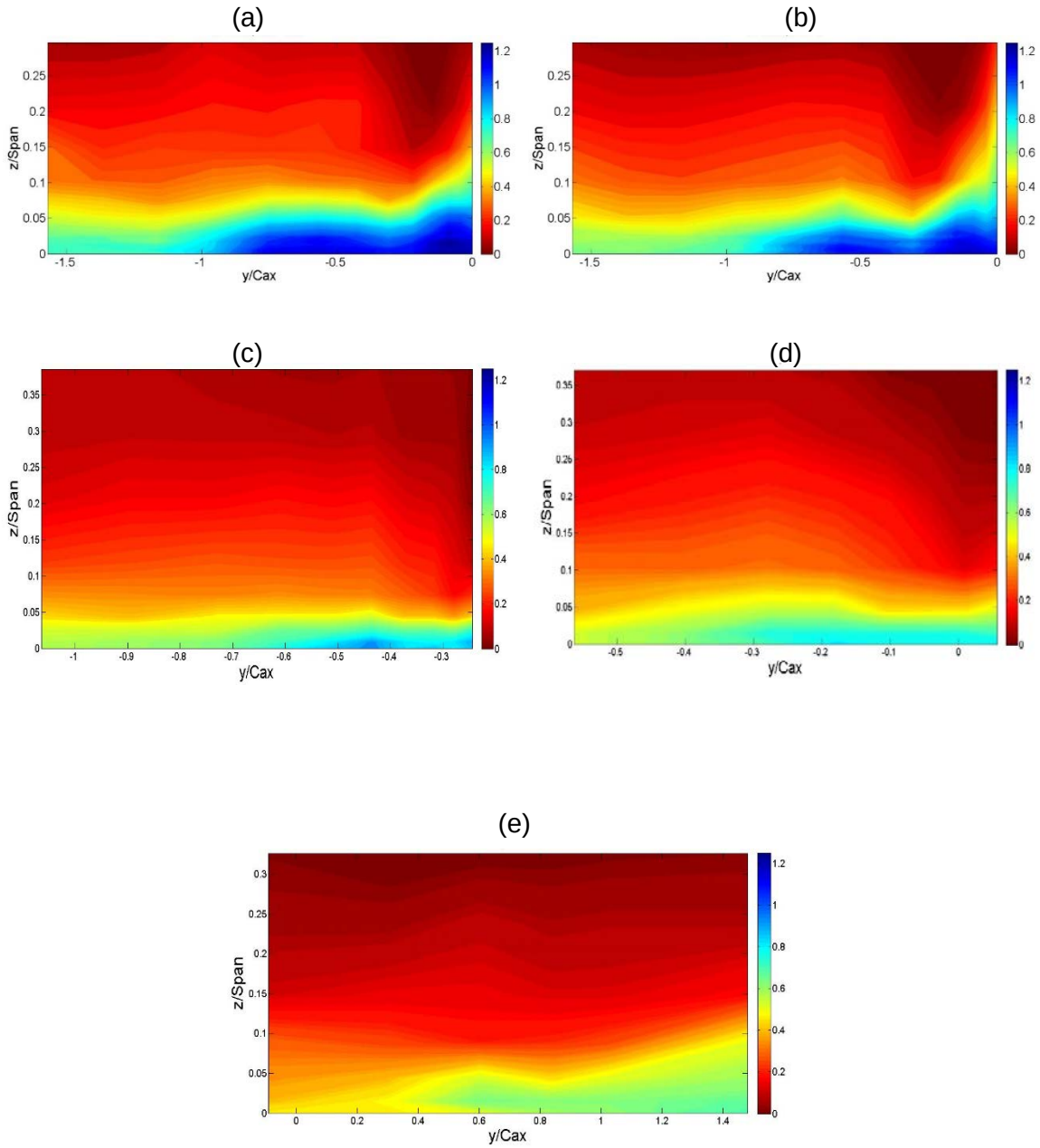

Figure 7-2: Passage thermal fields for MFR 0.5% (a) x/C_{ax} = -0.104 (b) x/C_{ax} = 0 (c) x/C_{ax} = 0.317 (d) x/C_{ax} = 0.612 (e) x/C_{ax} = 0.99

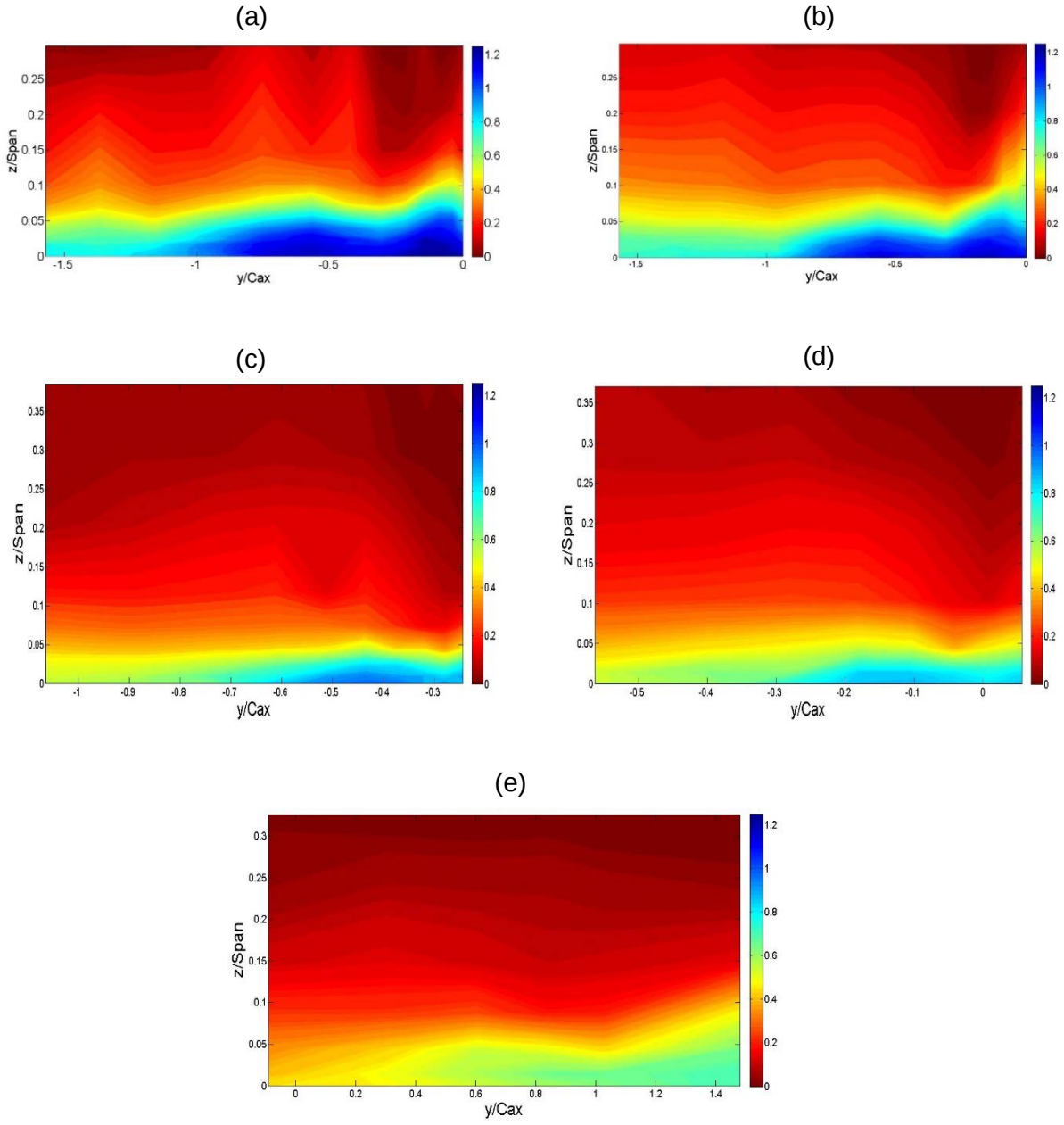

Figure 7-3: Passage thermal fields for MFR 1.0% (a) x/C_{ax} = -0.104 (b) x/C_{ax} = 0 (c) x/C_{ax} = 0.317 (d) x/C_{ax} = 0.612 (e) x/C_{ax} = 0.99

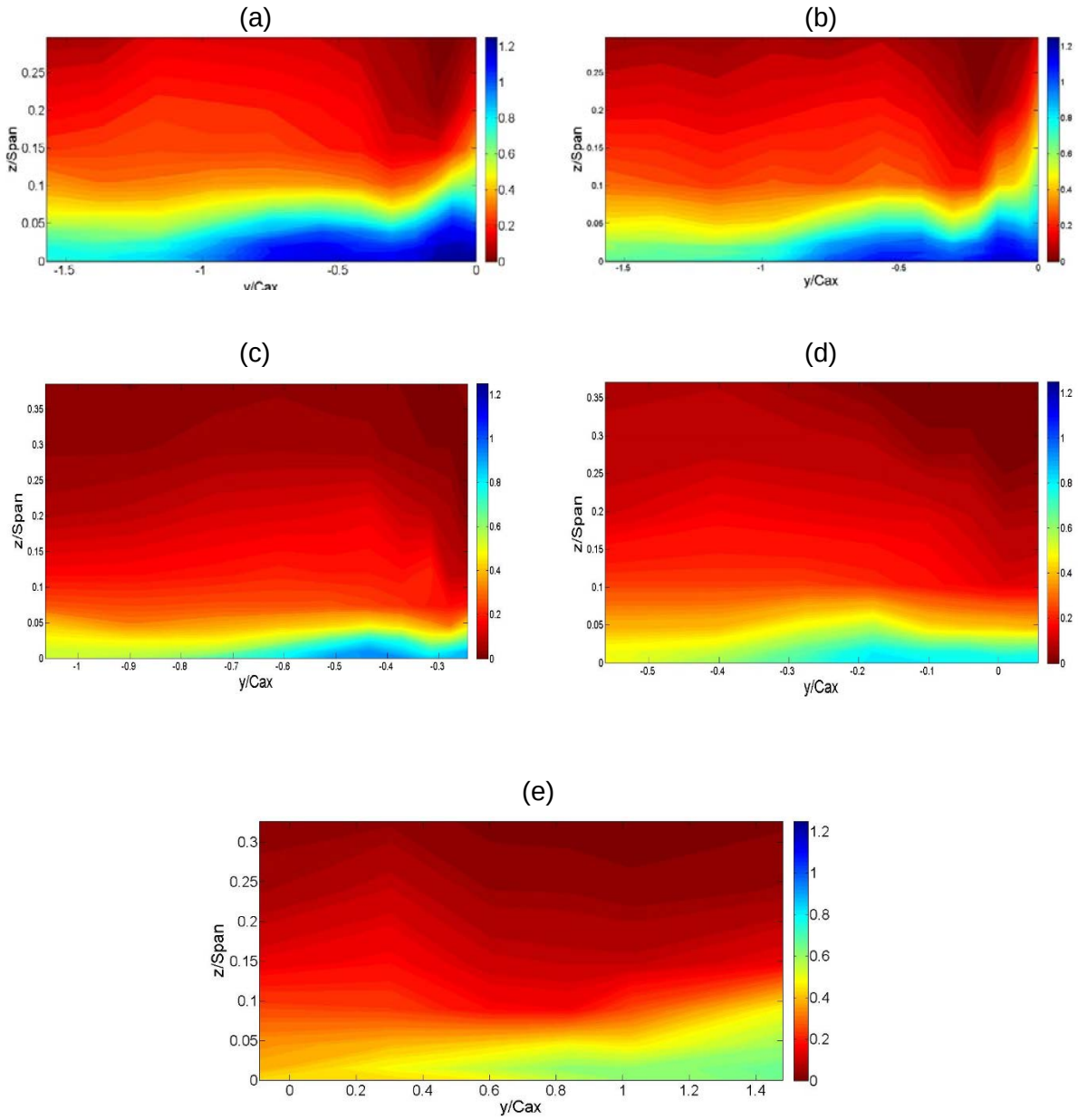

Figure 7-4: Passage thermal fields for MFR 1.5% (a) x/C_{ax} = -0.104 (b) x/C_{ax} = 0 (c) x/C_{ax} = 0.317 (d) x/C_{ax} = 0.612 (e) x/C_{ax} = 0.99

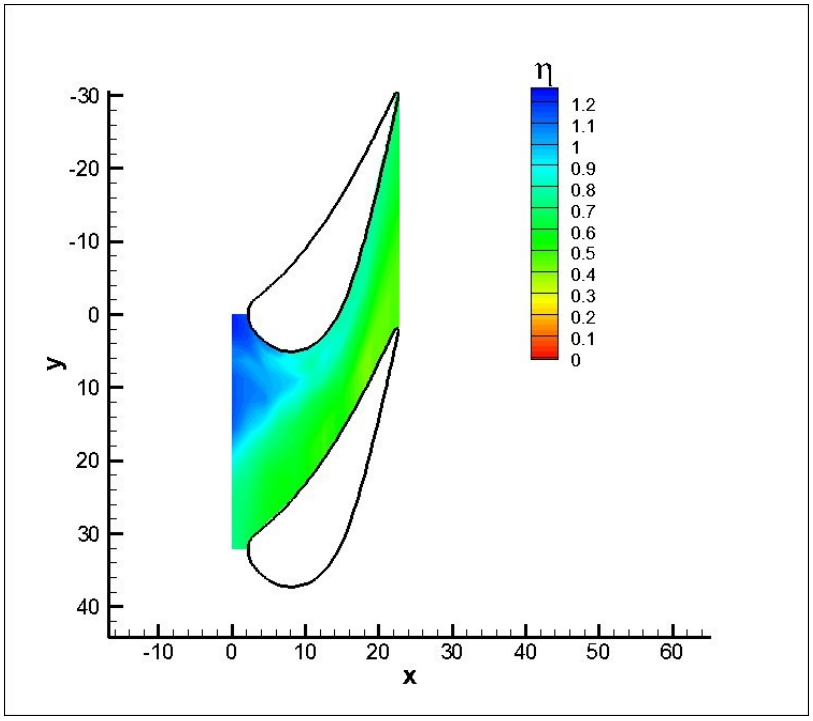

Figure 7-5: Endwall adiabatic effectiveness for MFR 0.5% (axes coordinates in cm)

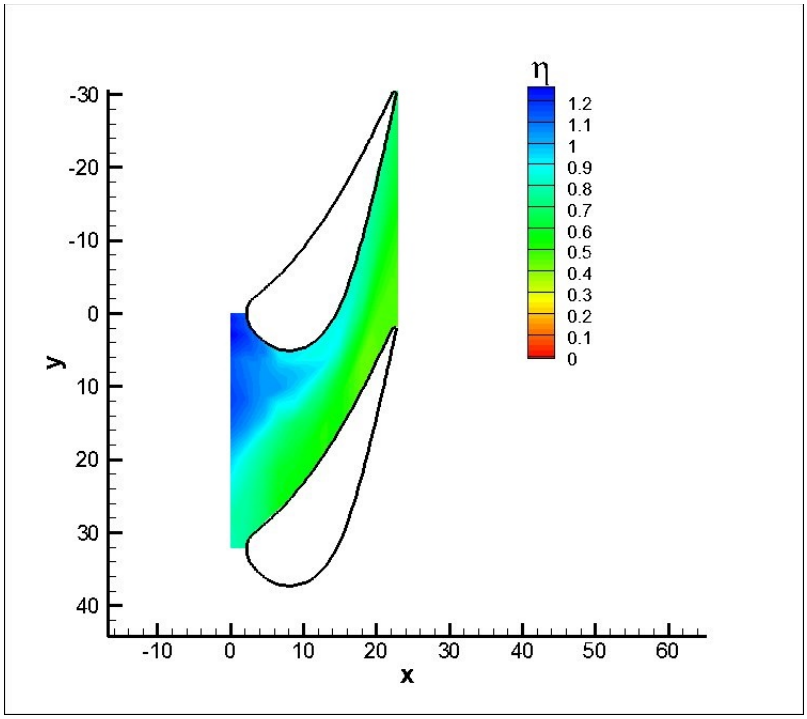

Figure 7-6: Endwall adiabatic effectiveness for MFR 1.0% (axes coordinates in cm)

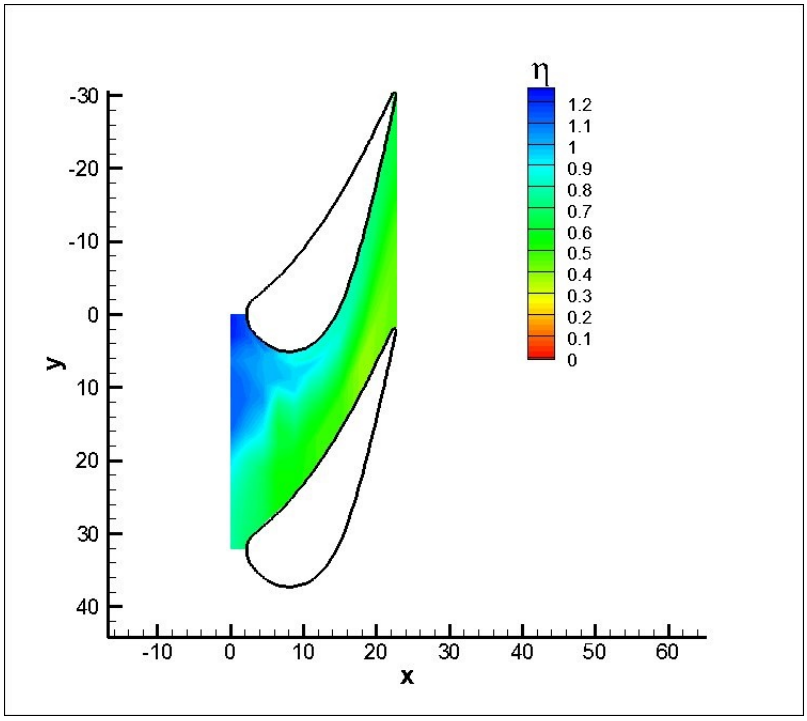

Figure 7-7: Endwall adiabatic effectiveness for MFR 1.5% (axes coordinates in cm)

7.3. Thermal Fields and Endwall Adiabatic Effectiveness based on Passage Inlet Temperature

The plots presented in the preceding sections are based on temperature fields normalized over differences between leakage flow temperature and mainstream flow temperature (T_L-T_O). Of particular importance to the gas turbine designer can be the thermal fields and adiabatic effectiveness which are based on the following definition:

$$\theta = \frac{\theta_{x,y,z}}{\theta_{max,inlet}} \qquad \text{Eq. 7-3}$$

$$\eta = \frac{\eta_{x,y,z=0}}{\eta_{max,inlet}} \qquad \text{Eq. 7-4}$$

where,

$\theta_{x,y,z}$ = Dimensionless field measured at any location x, y, z (Eq. 6-1)
$\theta_{max,inlet}$ = Maximum θ value at inlet plane (x/C_{ax} = -0.104)
$\eta_{x,y,z=0}$ = Endwall effectiveness at any location x,y, z=0 (Eq. 6-2)
$\eta_{max,inlet}$ = Maximum effectiveness value at inlet plane (x/C_{ax} = -0.104)

This form of data processing can show how the coolant (from leakage flow and near-wall coolant) migrates and mixes within the passage beginning from the inlet plane of the passage somewhat separated from the upstream mixing region of leakage flow and approach flow. However, these effects cannot be completely separated from this upstream effect since this mixing determines how the coolant distributes itself over the inlet plane which is being chosen as the reference for the above definition. Nevertheless, some isolation of the upstream effects can be made by analyzing the resulting plots. Another usefulness of these results lies in the possibility of comparison between the *rotor cascade* and the *stator cascade* thermal fields (discussed in detail in the next Chapter) as the various flows mix and migrate within the passage.

The thermal field results are presented in Figure 7-8, Figure 7-9 and Figure 7-10. Endwall adiabatic effectiveness results are presented in Figure 7-11. To aid in analyzing the data, simple two dimensional plots are also generated for the endwall effectiveness for the five locations as shown in Figure 7-12. The trends in migration and mixing within the passage essentially remain the same as discussed in the preceding sections. In addition to those discussions, these results present information about the drop in effectiveness/thermal field values relative to the inlet plane (x/C_{ax}= -0.104). For all the three MFR cases i.e. 0.5%, 1.0% and 1.5%, it can be observed that the coolant remains near to the endwall providing coolant coverage over the endwall surface. The manner of introduction of leakage flow through the upstream leakage slot results in the coolant remaining nearer to the endwall surface as seen in the first plane. Further down that plane, the coolant continues to cover the endwall surface, with better coverage near the suction side due to the cross-stream pressure gradient. Relative to the inlet plane (x/C_{ax}= -0.104), the coolant 'blue' core size reduces in the leading edge plane (x/C_{ax}=0) due to the leading edge vortices that form ahead of the stagnation point resulting in some of the mixing, although the effectiveness values do not appear to reduce much for the MFR 1.0% case as compared to other MFR cases as can be seen from the line plots (Figure 7-12).

An interesting observation is that the effectiveness values on the suction side and in the middle portion of the passage are lower for MFR 0.5% and 1.5% cases as compared with the MFR 1.0% case (as discussed already). However, the pressure side effectiveness values for *all* MFR cases seem to be quite similar slightly downstream of leading edge region, planes starting from x/C_{ax}=0.317 (refer to Figure 7-12). These results corroborate the findings of Burd et al. [77] and Oke et al. [78] who performed passage thermal field measurements on cascades of similar configurations. They found the suction side coolant

accumulation to reduce when increasing the leakage blowing ratio while the pressure side did not change significantly. It has been already discussed how the contoured endwall contributes by thinning the flow boundary layer and weakening the secondary flow structures formed subsequently. The higher MFR coolant also ‘energizes’ the boundary layer to some extent by adding streamwise momentum. But this effect persists mainly in the leading edge region. Further downstream, the effect is not very significant possibly due to the strong sweeping action of endwall cross flows that tend to push the coolant away from the pressure side to the suction side. Hence, it seems that the main contribution in enhancement of coolant coverage near the pressure side is by the contoured endwall which tends to be similar for all the cases of MFR. This results in a significant difference in effectiveness values in the pressure side region only near the leading edge for various MFR cases but an insignificant difference in downstream locations.

It is recalled that a ‘thick’ approach flow temperature profile is used in the present study. It extends up to the mid-span location which allows some coolant to be away from the endwall. This protects some part of the coolant from getting entrained into the horseshoe vortex in the leading edge region and the passage vortex that begins to develop in the early portions of the passage. This coolant, later in the downstream portions of passage, impinges on the pressure wall of the blade, sweeps down the blade wall and along the endwall surface in the downstream portions of the passage. This coolant along with the coolant that is approaching these portions from the upstream locations yields high effectiveness values even in the trailing edge plane (~60% of inlet plane maximum effectiveness near suction side for MFR 1.5% case).

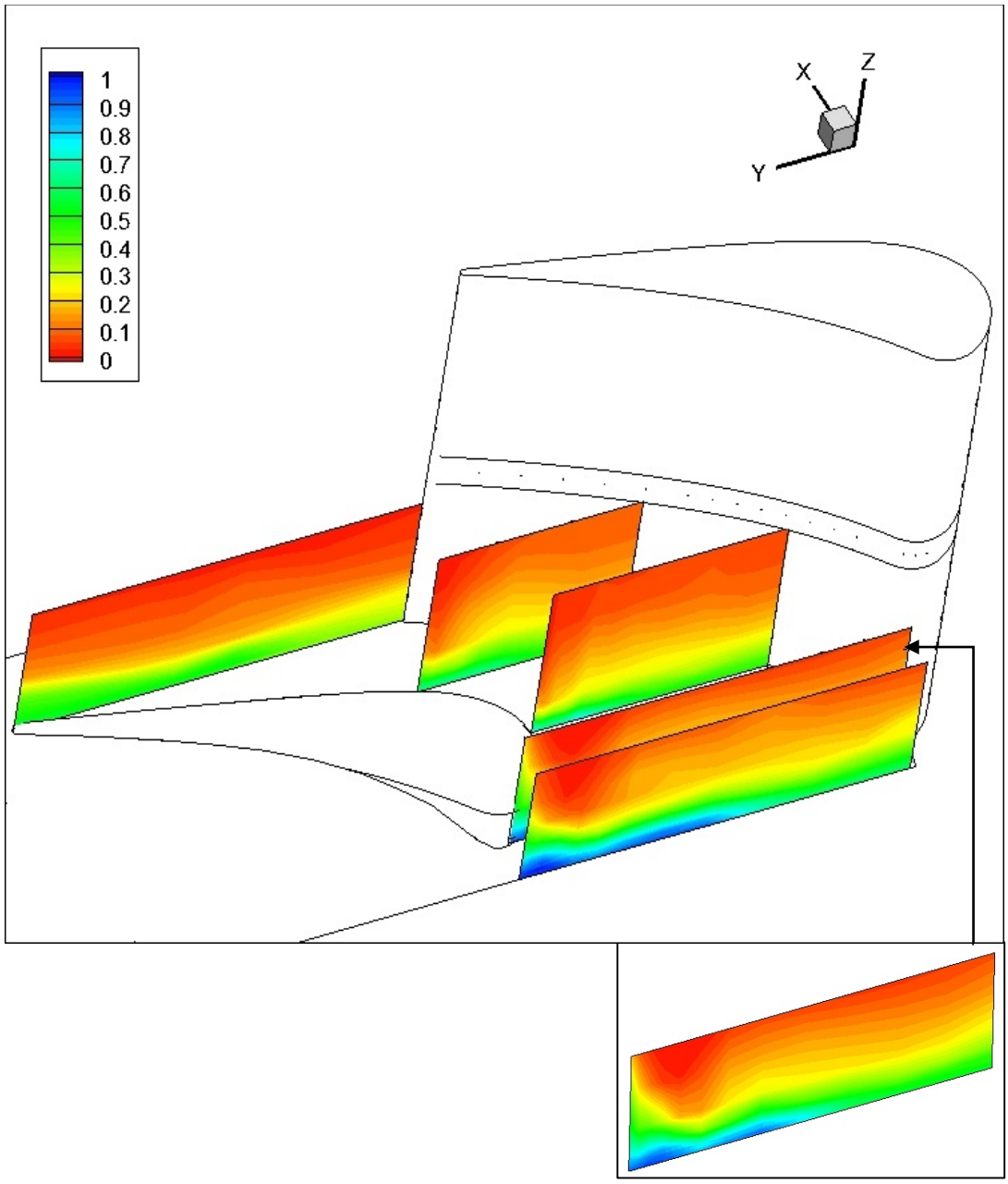

Figure 7-8: Passage thermal field based on maximum passage entry temperature for MFR 0.5% (Inset: Plane at leading edge $x/C_{ax}=0$)

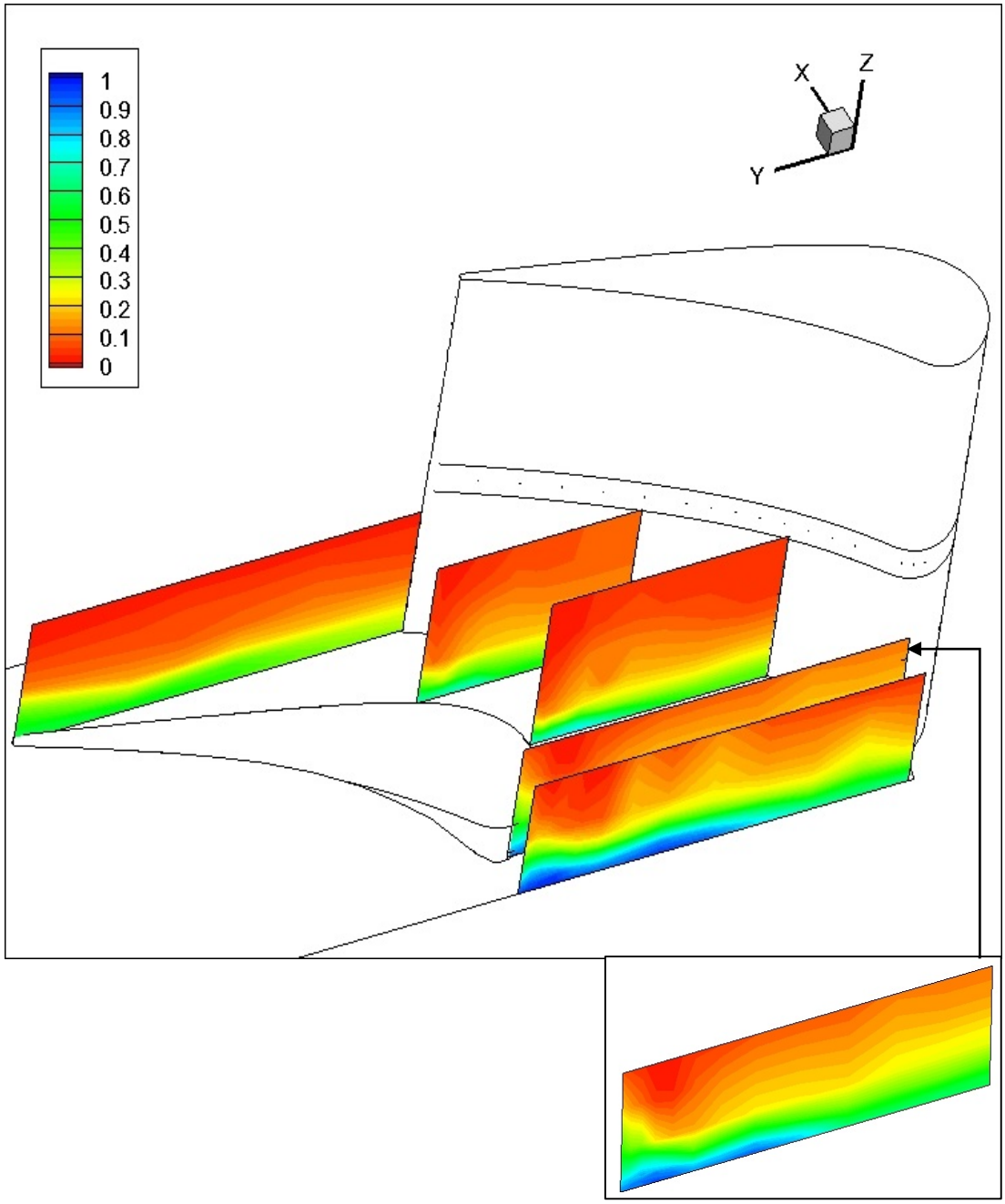

Figure 7-9: Passage thermal field based on maximum passage entry temperature for MFR 1.0% (Inset: Plane at leading edge $x/C_{ax}=0$)

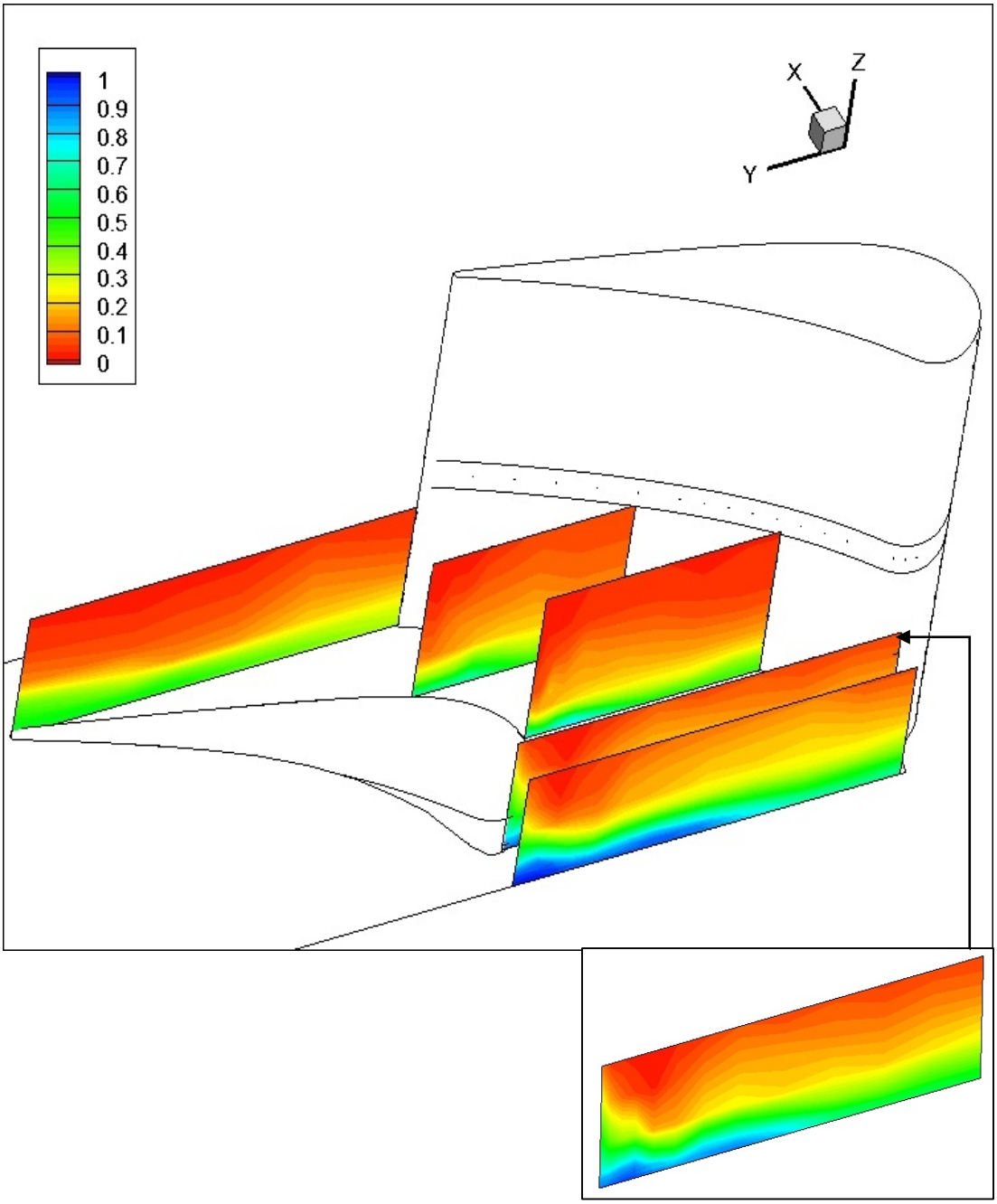

Figure 7-10: Passage thermal field based on maximum passage entry temperature for MFR 1.5% (Inset: Plane at leading edge $x/C_{ax}=0$)

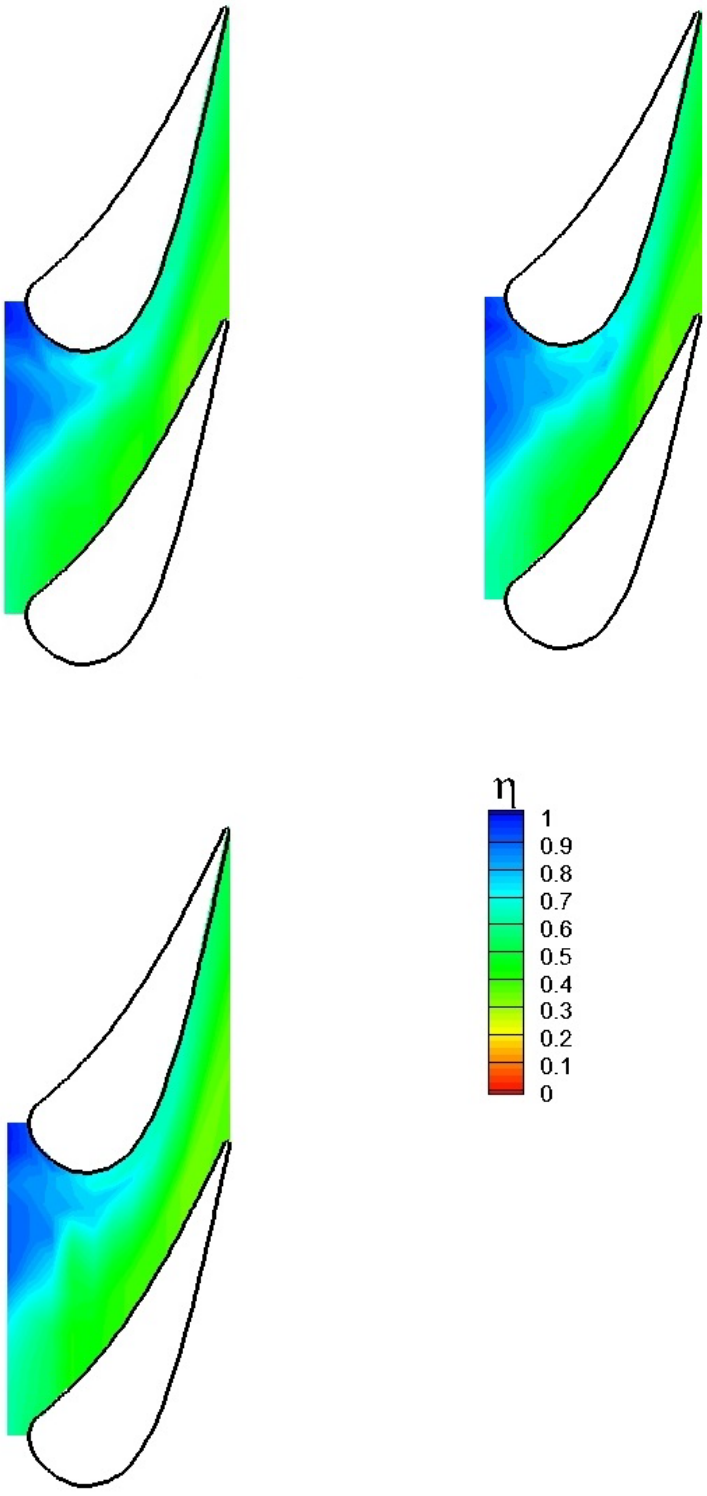

Figure 7-11: Endwall adiabatic effectiveness based on passage maximum inlet temperature for (Top Left) MFR 0.5%, (Top Right) MFR 1.0% and (Bottom) MFR 1.5%

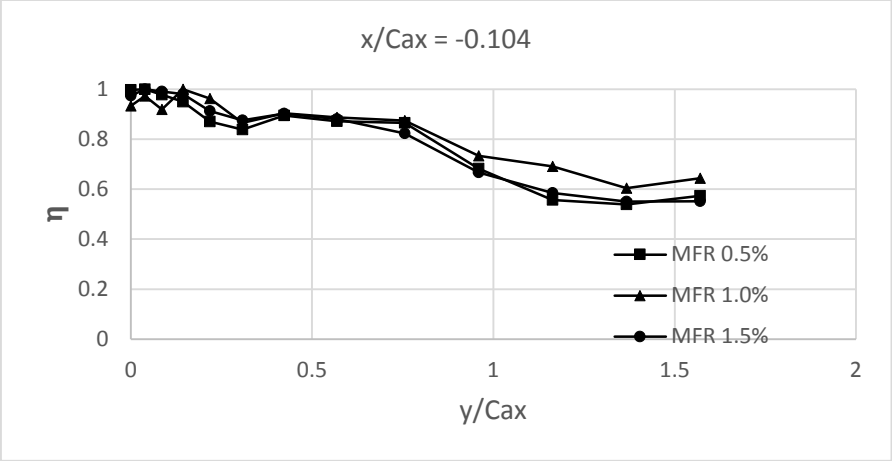
x/Cax = -0.104
η
y/Cax
MFR 0.5%
MFR 1.0%
MFR 1.5%
0
0.2
0.4
0.6
0.8
1
0
0.5
1
1.5
2

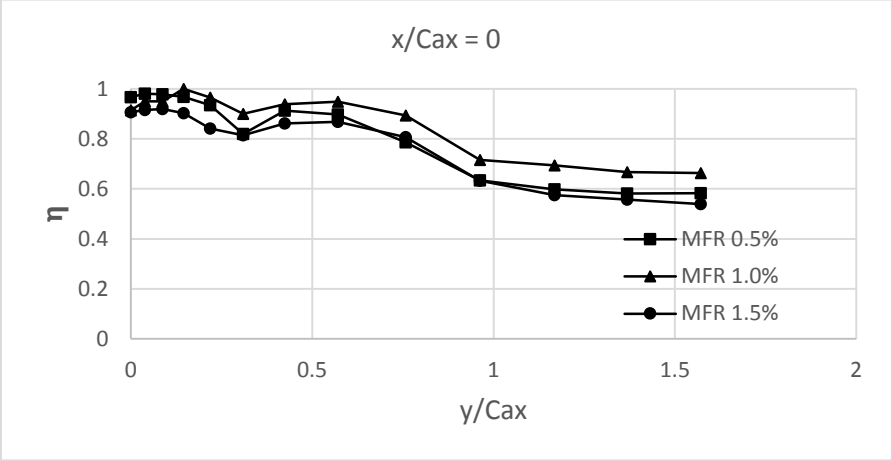
x/Cax = 0
η
y/Cax
MFR 0.5%
MFR 1.0%
MFR 1.5%
0
0.2
0.4
0.6
0.8
1
0
0.5
1
1.5
2

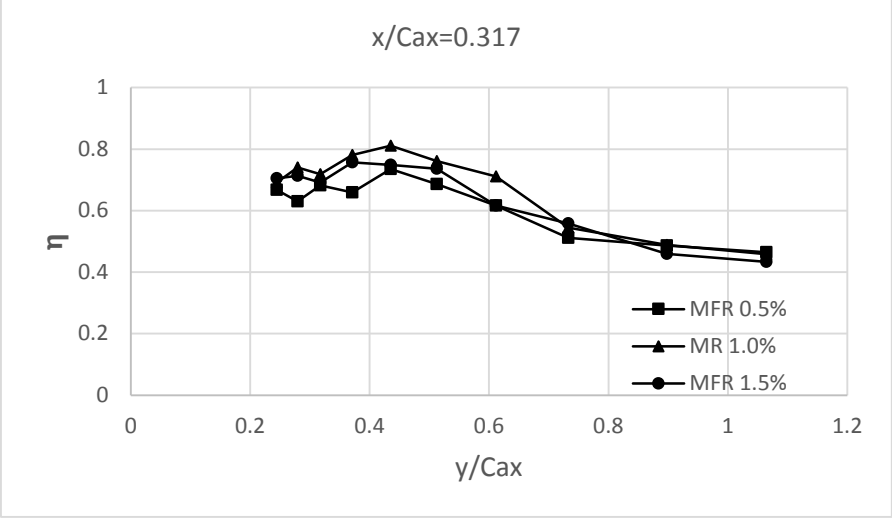
x/Cax=0.317
η
y/Cax
MFR 0.5%
MR 1.0%
MFR 1.5%
0
0.2
0.4
0.6
0.8
1
0
0.2
0.4
0.6
0.8
1
1.2

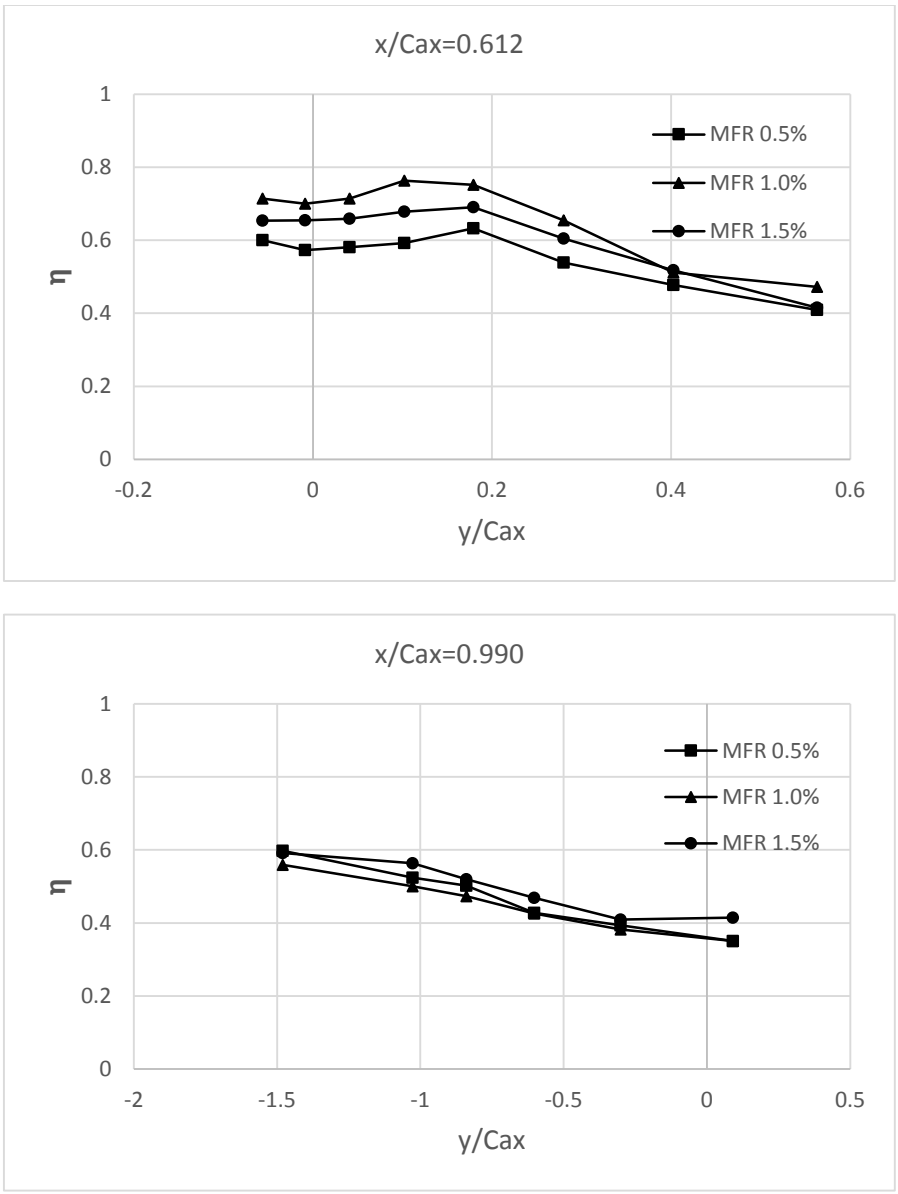

Figure 7-12: Maximum passage entry temperature based effectiveness values for MFR 0.5%, 1.0% and 1.5% at axial locations x/C_{ax}= -0.104, x/C_{ax}=0, x/C_{ax}=0.317, x/C_{ax}=0.612 and x/C_{ax}=0.99. Left and right sides of plots represent suction side and pressure side respectively

Chapter 8 Rotor Cascade: Results and Discussion

This chapter presents the results for the *rotor cascade* test facility (detailed description of experimental test facility and procedure given in the Appendix and Section 6.3 respectively). The aim is to present results in the form of thermal fields within the leakage flow ejection region (essentially the leakage slot) and then compare the performance of the *rotor* stage cascade to that of the *stator* stage cascade. These discussions can help the gas turbine designer in assessing the effect of the leakage slot geometry on the migration and mixing of leakage 'coolant' flow within the passage in the presence of different mass flow rates of leakage. A general understanding of how the cooling effectiveness varies as one moves from first stage stator to the first stage rotor in a gas turbine and the possible reasons associated with such changes, can be obtained from these discussions. However, it should be kept into consideration while using these comparisons that in the case of the rotor cascade test facility, the effects of an upstream stator vane row of an actual gas turbine are absent.

8.1. Leakage Flow Ejection Region

Results for the thermal fields within the leakage flow ejection region are given in Figure 8-1, Figure 8-2 and Figure 8-3. The dimensionless values as described by Eq. 6-3 and Eq. 6-4 are plotted. Higher values of θ and RMS_θ represent less amount of coolant and higher unsteadiness values, respectively. On each plot, the left side represents the suction side and right side represents the pressure side. The approach flow has near-wall coolant up to 45% of span, as shown by the approach flow temperature profile in Figure 0-5 (see Appendix).

First, let us consider the dimensionless temperature field plots. It is clear from the previous discussions that there exists within the cascade passage, a cross-stream pressure gradient from the pressure to the suction sides. The coolant flow emitting out of the leakage slot redistributes itself along the pitchwise direction as it 'sees' the varying pressure within the passage, with more coolant near the suction side than near the pressure side as is evident from the plots where the planes near to the suction side show higher amount of coolant (lower θ values). The leakage slot dimensions are quite large (as compared to the thin leakage slot geometry in the stator cascade). This gives the mainstream flow opportunity to ingress into this slot that causes the coolant to mix to some extent, further adding to the uneven distribution of coolant along the pitchwise direction (from pressure side to suction side). This, in turn, yields lowering of the film cooling effectiveness of the leakage flow as observed within the cascade passage. Note that the MFR 0% case shows presence of some coolant which is essentially the near-wall fluid in the approach flow to the cascade; the simulated combustor liner coolant. This makes evident the ingression of mainstream flow into the leakage slot. Due to the mainstream flow entering the leakage slot, the near-wall coolant present within the mainstream flow also enters the slot which is observed in the form of 'blue' (lower θ value) regions. Here also, the coolant coming from the mainstream flow ingression, is swept toward the suction side as marked by lower θ values.

Now comparing MFR cases 0% and 1.5%, one can see that more coolant is present at all plane locations for the higher leakage mass flow rate case which is expected due to presence of greater mass flux of overall coolant spread at all pitchwise locations. These MFR cases, if compared with the MFR 0.5% case, show better performance with greater spread of coolant at all plane locations. A larger red core can be seen for the MFR 0.5%

case suggesting ingression of mainstream flow. This behavior can be explained in terms of momentum flux ratio which increases as the square of MFR value (shown by Eq. 7-1). The test cases with MFRs of 0%, 0.5% and 1.5% correspond to momentum flux ratios of 0%, 0.025% and 0.23%, respectively and mass flux ratios of 0%, 1.59% and 4.77%, respectively. Lower leakage mass flow rate due to its lower momentum flux causes greater sloshing and mixing of the coolant within the leakage slot resulting in such trends. With the MFR 0% case, this sloshing is apparently reduced as marked with lower θ values in the pressure side planes as compared with those of MFR 0.5% case. On the other hand, leakage flow in the MFR 1.5% case, has higher momentum flux helping it to counter the ingression of mainstream fluid and cross-stream pressure gradient, hence resulting in lesser mixing of the coolant and subsequently better endwall effectiveness values within the passage (observed in next section). The 'green core' region in the plane nearest to the suction side in the MFR 0.5% case may be due to the stagnation region flow reversal, more pronounced in the lower leakage mass flow rate case.

The root mean square fluctuations for all cases of MFR are shown in Figure 8-4, Figure 8-5 and Figure 8-6. It is observed that unsteadiness is greater near the pressure side than the suction side for each MFR case. The fluid is being swept from the pressure side influenced by the cross stream pressure gradient resulting in higher unsteadiness. For MFR 1.5%, RMS fluctuations are lower than the other two cases implying lower unsteadiness. However, for the same case, on the planes nearer to pressure side on the endwall surface (z/S=0), the unsteadiness appears to be more, which is due to the mixing region resulting from merging of the leakage flow with mainstream flow.

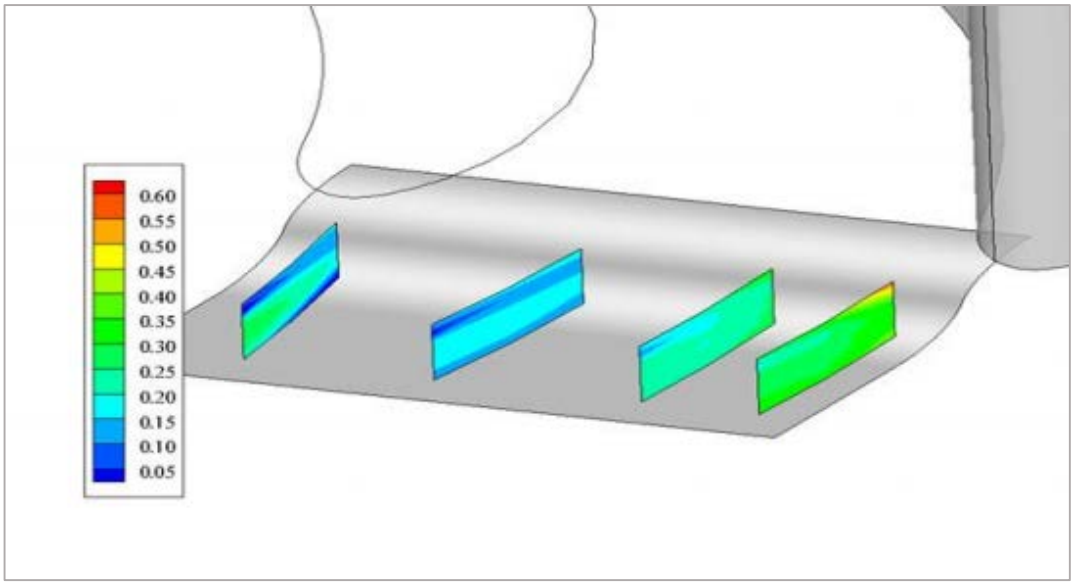

Figure 8-1: Thermal field plot for MFR 0% (no leakage flow; only upstream coolant in near-wall region)

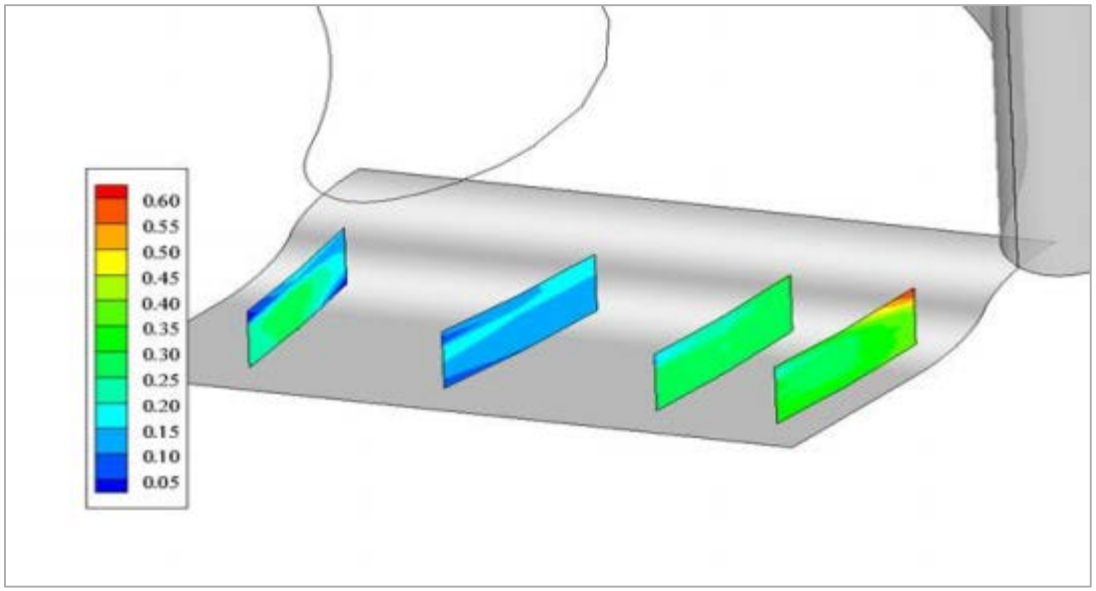

Figure 8-2: Thermal field plot for MFR 0.5% (containing leakage flow and upstream near-wall coolant)

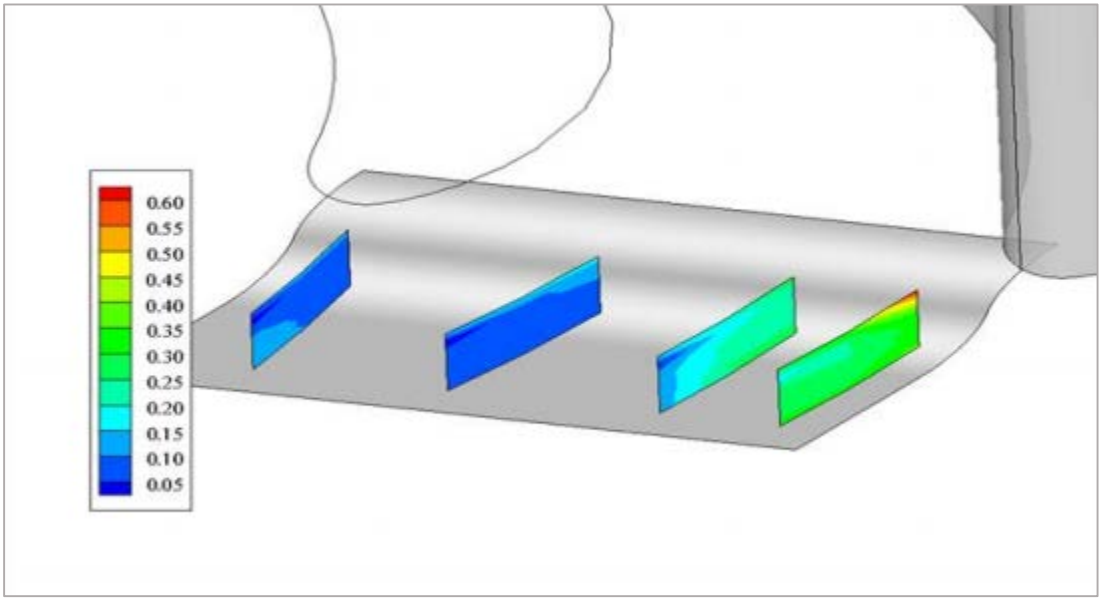

Figure 8-3: Thermal field plot for MFR 1.5% (containing leakage flow and upstream near-wall coolant)

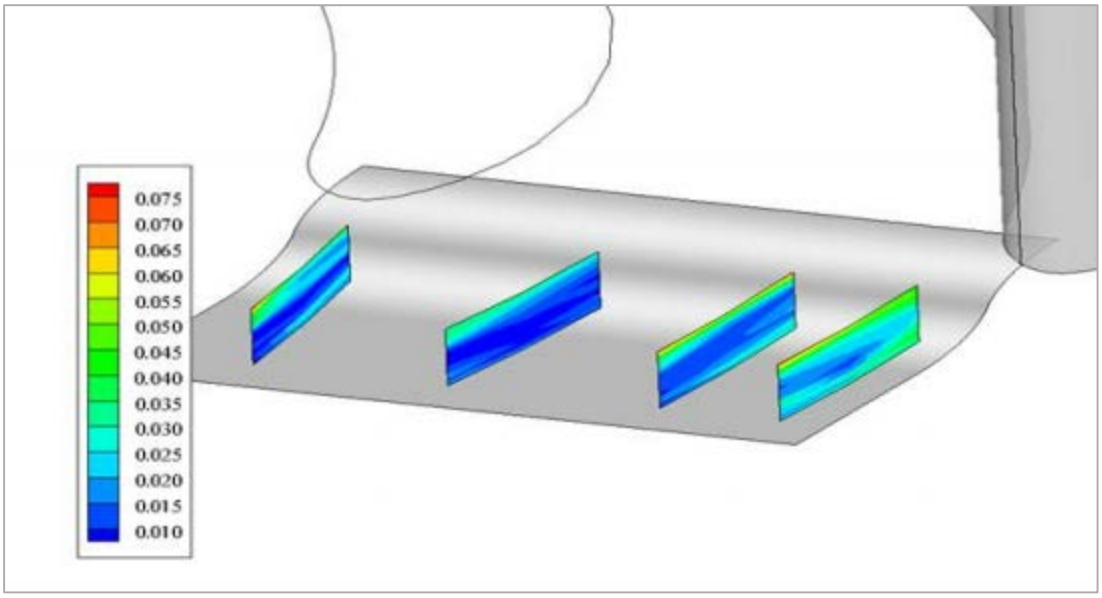

Figure 8-4: Thermal field root mean square temperature fluctuations for MFR 0%

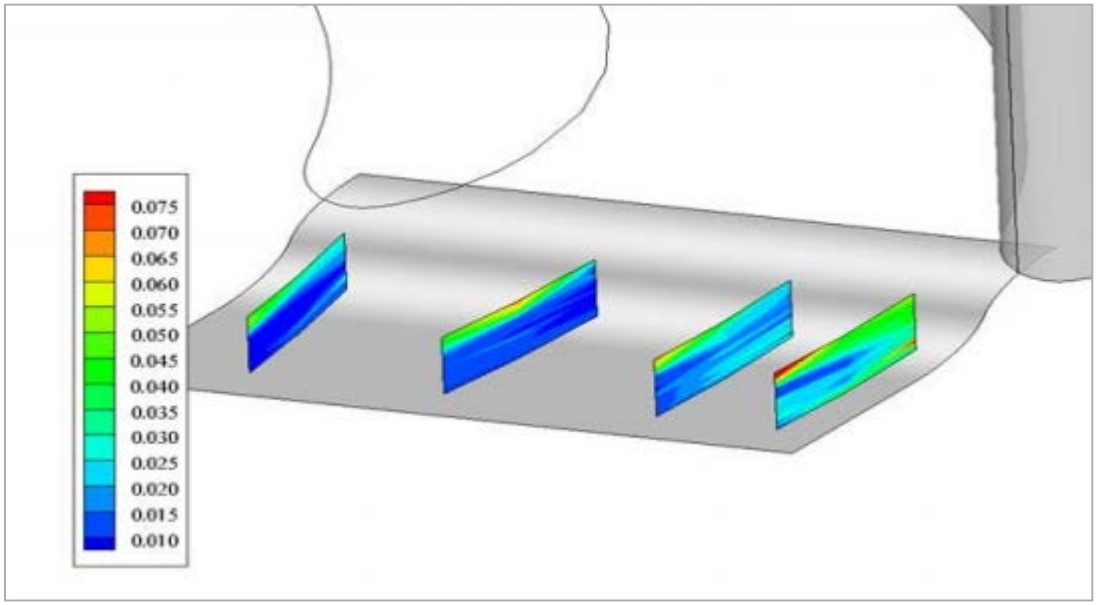

Figure 8-5: Thermal field root mean square temperature fluctuations for MFR 0.5%

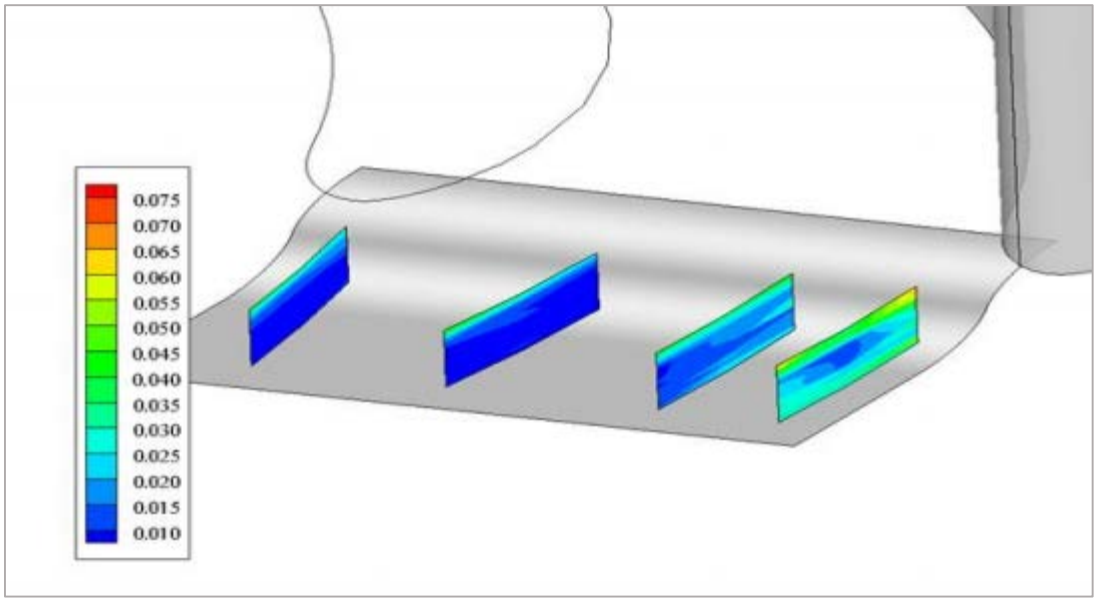

Figure 8-6: Thermal field root mean square temperature fluctuations for MFR 1.5%

8.2. Comparison with Stator Performance

It is useful to compare the performance of the *stator stage* cascade with the *rotor stage* cascade by comparing thermal fields and endwall adiabatic effectiveness values measured within the respective passages. A general understanding of how the cooling effectiveness varies from first stage stator to the first stage rotor and the possible reasons for such changes can be derived from these discussions. The comparison will allow to study the effects of characteristics that are uncommon to both cascades, for example geometrical features including cascade layout, leakage slot geometry and endwall contour shape.

Before comparing the results from the two test sections, it is important to ensure that the flow features and operational characteristics (free stream turbulence, Reynolds number, approach flow temperature profile, leakage mass flow rates) of both experiments are similar for such discussions to be meaningful as these factors are known to have their own significant effects on endwall heat transfer. Since both test facilities have been designed in such a manner that their flow characteristics are representative of actual gas turbine conditions, the above requirements are satisfied. Next, in any experimental cascade, blade spacing-chord ratio is of particular importance. If the blade spacing is low (higher solidity), then the flow is guided more efficiently through the cascade passage but frictional losses increase. If blade spacing is high, then flow with its poor guidance may be subjected to flow separation and associated losses. Usually, ‘Zweifel criterion’ is employed in determining an optimum blade space-chord ratio to minimize these losses. It states that the actual to ideal tangential blade loading ratio should be close to 0.8 for minimum losses. This criterion provides a ‘scalar’ to compare both cascades and determines whether the discussion on the comparison of the passage thermal fields for both cascades should

include effect from the geometrical differences and secondary flow structures, or should the impact from these additional losses also be considered. The Zweifel coefficient is defined as [79]:

$$Z = 2\frac{s}{b}cos^2\alpha_2(tan\alpha_1 + tan\alpha_2) \qquad \text{Eq. 8-1}$$

where

s = Blade spacing (=pitch)
b = Axial chord length
α_1 = Inlet flow angle (for stator = 0˚ and rotor = 40˚)
α_2 = Outlet flow angle (for the present calculation, blade camber line exit angle is used rather than actual outlet flow angle; for stator = 72˚ and rotor = 70˚)

Based on the definitions above, the Zweifel coefficient is found to be 0.82 and 0.91 for the rotor and stator cascade, respectively. This shows that the stator cascade is more heavily loaded than the rotor cascade. However, the difference is not very significant which implies that the major effect causing the dissimilarity in performances of the two cascades is mainly due to the geometrical features. It should be noted that since the definition of the Zweifel coefficient has dependence on the blade camber line exit angle instead of the outlet flow angle, these calculated values may change, somewhat, due to the different flow guidance abilities of the cascade passages, which tend to drop with increases in Zweifel coefficient.

Another important condition for the comparison study to be meaningful is to ensure that consistent/equivalent definitions of passage thermal fields for both test facilities are used. For this purpose, thermal fields based on Eq. 7-3 and Eq. 7-4 are used which show how the temperature at the ‘hottest’ point in the inlet plane propagates further into the passage by mixing with the turbulent mainstream flow and being affected by the secondary flow

structures. It should be noted here that the reference 'inlet plane', unlike in the description for these equations in Section 7.3, is chosen as $x/C_{ax}=0$ (instead of $x/C_{ax}= -0.104$).

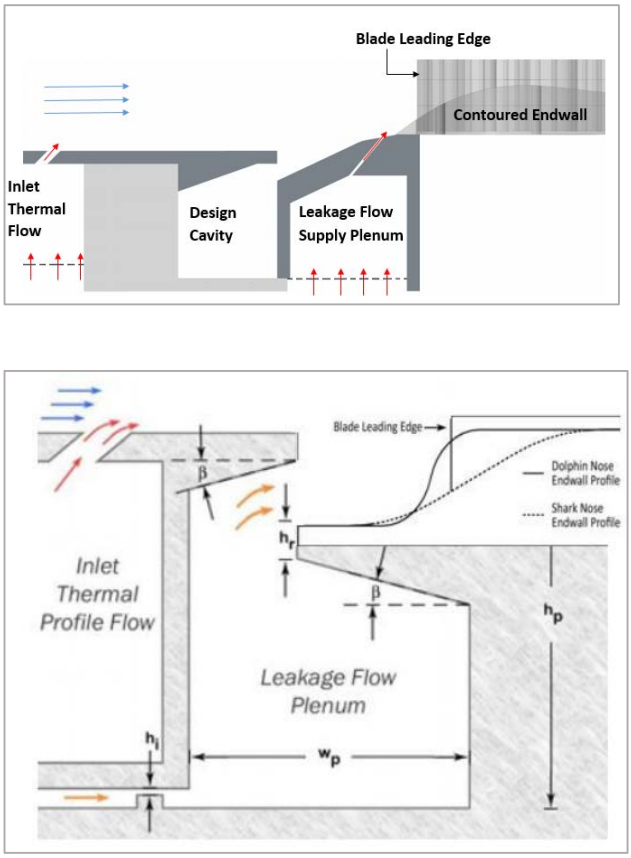

Figure 8-7: Geometry of leakage slot and contoured endwall for (Top) Stator cascade and (Bottom) Rotor Cascade[54]

8.2.1. Passage Thermal Fields

The plots are presented in Figure 8-8, Figure 8-9 and Figure 8-10. For both stator and rotor cascade, mass flow ratio (MFR) is the ratio of leakage mass flow rate to the mainstream mass flow rate, taken for the present purpose of comparison as 0.5%, 1.0% and 1.5%. In all cases for both cascades, coolant is swept across the endwall towards the suction side due to the endwall cross flows created by the cross-stream pressure gradient.

The first striking feature that differentiates the rotor cascade flow from the stator cascade flow is the carrying (advection) pattern of coolant throughout the passage. First we take a look at the rotor cascade fluid mechanics. The development of the passage vortex is easily observable since coolant has been entrained into the vortex. The passage vortex is predominantly the pressure side leg of the horseshoe vortex that forms at the stagnation point ahead of the blade. It is joined by the endwall cross flows that strengthen its effect. It grows in size and strengthens as it traverses through the passage (refer model proposed by Wang et al. depicted in Figure 2-3). The coolant that lies near to endwall (in a region which is occupied by the vortex) gets 'trapped' within this rising vortex and is lifted off the endwall as seen in downstream planes of rotor cascade plot. This leaves very little coolant to actually contribute to endwall protection. The thick approach flow temperature profile containing coolant from the combustor liner contributes to enhancing the endwall coolant coverage especially in the downstream regions. This occurs when coolant that is away from the reach of the passage vortex returns in the downstream portions of the passage, down the pressure wall of the blade and across the endwall to provide better coolant coverage [3]. Now, looking at the stator cascade plots, this entrainment of coolant is not observed. In fact, the coolant from the very beginning of the passage, remains near to the endwall with a more uniform distribution of coolant from pressure side to suction side, although still providing better coverage to suction side. The coolant is ejected with a sufficiently high momentum to penetrate the developing secondary flow structures in the upstream regions of the cascade, which enables it to remain nearer to the endwall. The passage vortex still develops as it is a characteristic of the flow field in a turbine passage. Its effect is visible in the region near the suction side of the leading edge plane where coolant appears to have mixed out, resulting in little or no coolant as compared to the neighboring regions within that plane. The existence of a suction side leg of the horseshoe

vortex may also add to the mixing occurring in this region and, hence, weakening of the cooling effect. Therefore, the different patterns of coolant migration and mixing create the major differences in the performance of the two stages (rotor and stator) in terms of passage thermal fields.

The drop in the magnitude of the dimensionless temperature (θ) is seen more in the rotor cascade than the stator cascade, as one goes downstream within the passage. The pressure side region of the stator cascade gets much less coolant than the pressure side region of stator cascade. It can be understood from the manner in which the leakage flow is delivered to the passage. Given in Figure 8-7 are the geometries of the leakage flow supply systems. The rotor test facility has a much larger slot geometry than the one used in stator test facility, as governed by the high pressure gas turbine design features. The ratio of areas corresponding to mainstream flow entrance area and leakage flow exit area is calculated as 3.189 (much less than that of stator cascade test facility ~102). These large features allow more sloshing of the coolant within the slot itself that not only causes undesirable pitchwise mixing but also lowers the streamwise momentum of the coolant being ejected out of the slot. This process disables, to some extent, the ability of the coolant to 'compete' with the strong secondary flow structures (including the passage vortex) which makes some of the coolant to get entrained within the passage vortex. On the other hand, in the stator test facility, the leakage slot geometry with its thin design, allows less mixing of the coolant within the slot itself and ejects the coolant with sufficiently high momentum to counter the secondary flow structures. Consequently, the coolant remains nearer to the endwall throughout the passage, with some mixing of the coolant with the mainstream flow in the outer parts of coolant core region. Additionally, the larger slot geometry allows a huge amount of mainstream flow ingression (as discussed in

preceding Section 8.1) which results in a pitchwise variation in temperature and also the lowering of θ values, which in turn further yields lower θ values within the passage. The slot geometries are governed by the design requirements of the high pressure turbine for its rotor stage and stator stage, separately. These comparisons give an overall understanding of how the coolant migrates within the passage as one moves from stator to rotor in the turbine. Some ideas on design changes may also be derived from these discussions.

Another important feature that contributes to the observed performances is the contoured endwall. The contouring schemes for both cascades can be seen in Figure 8-7. Clearly, the endwall is contoured with a gradual slope all the way through the passage in the stator cascade whereas in the rotor cascade, it is present as a steep slope in the leading edge region ('Dolphin nose'). One important reason behind the presence of rotor endwall contouring only in the leading edge region lies in the purpose it is expected to fulfill. As mentioned before, there is a great deal of mixing occurring in the pitchwise direction of the leakage slot that sloshes around the coolant with the mainstream flow resulting in an undesirable lowering of the θ values. It is necessary that the coolant flow is ejected out with sufficient momentum to compete with the secondary flow structures. The 'dolphin' nose endwall helps in this regard by providing acceleration to the flow in this region, which in turn causes thinning of boundary layer of the approach flow, and a weakening of the secondary flow structures. The effects of contouring reduce, however, as one moves further downstream. The pressure side θ values drop significantly from the leading edge region to the downstream regions. On the other hand, the contouring scheme in the stator facility accelerates the flow even within the passage giving additional momentum to the near-wall coolant fluid to counter the strong endwall cross flows. This can also be the

reason of relatively higher coolant coverage even on the pressure side of the passage where this ‘energized’ near-wall coolant fluid may resist the strong pressure gradient to some extent. In addition to this, the contoured endwall shape in the stator cascade reduces the leakage injection angle with lesser penetration into the mainstream flow.

After looking at patterns of flow migration and mixing for both cascades, it is interesting to study the effects of leakage mass flow rate on passage thermal fields for both cases. For the stator cascade, most of the variations occur near the endwall. Due to the 3D view of presentation, differences in passage thermal fields may not be very apparent (for better viewing, refer Figure 7-2, Figure 7-3 and Figure 7-4). It is clear that the effect of MFR is much more pronounced in the rotor cascade. Here, on increasing the MFR, the coolant core size increases significantly, mainly at planes downstream of the leading edge plane. This is expected since as MFR is increased, the mass and momentum flux increase making the coolant flow eject out from the leakage slot and ‘compete’ with the strong secondary flow structures. Thus, relative to the maximum thermal field value on the leading edge plane, the downstream planes show a higher percentage of this maximum value indicating greater sustenance of coolant further downstream of the passage. On the other hand, in the stator cascade, the coolant spread increases going from MFR 0.5% to 1.0% but decreases for MFR 1.5%. This phenomenon again can be explained from the context of the momentum flux of the coolant flow ejecting out of the leakage slot. With higher MFR, momentum flux increases which results in some of the coolant from actually penetrating the mainstream flow rather than providing coverage to the endwall. In the trailing edge plane, insignificant changes occur for different MFR cases. Whereas for rotor cascade, the differences are significant since the coolant core entrained within the passage vortex is larger for the MFR 1.5% case. However, for the purpose of endwall

cooling, the exit plane effectiveness values are similar for all leakage mass flow rate cases even for the rotor cascade, as seen in the following sections on endwall adiabatic effectiveness.

8.2.2. Endwall Adiabatic Effectiveness

The adiabatic endwall effectiveness plots for both rotor and stator cascades are given in Figure 8-11, Figure 8-12 and Figure 8-13. It should be remembered that the values being plotted are effectiveness values normalized over the maximum effectiveness at the leading edge plane.

Comparing the plots for any MFR case, it can be observed that in both cascades, as expected, the coolant is swept towards the suction side due to endwall cross flows. A striking difference is the effectiveness values on the pressure side of the passage. In the rotor cascade, the effectiveness values on the trailing edge drops to almost 10% of its maximum value at the leading edge plane as compared to 40% in the stator cascade passage. Also, the pressure side throughout the rotor passage experiences rapid reduction of effectiveness. On the other hand, the stator passage pressure side is seen to be covered with coolant more uniformly. Now, as with the passage thermal fields, the manner of coolant flow ejection, endwall geometry and cascade passage geometry serve to explain these phenomena. First consider the rotor passage. The leakage flow is ejected from the large leakage slot that results in sloshing around of the fluid within the slot, which, in turn, delivers this fluid into the mainstream flow with less ‘control’. There is some ingression of the mainstream flow into the slot which further mixes out the coolant that is ejected out of the slot causing the unequal distribution of coolant on the leading edge plane. Additionally, some of the coolant gets entrained within the passage vortex, as seen from the thermal fields in the preceding section. Also, the coolant with lower momentum

is unable to ‘compete’ with the strong endwall cross flows and is easily swept towards the suction side. These factors lead to lowering of the coolant coverage on the pressure side. Now consider the stator passage. Coolant is delivered into the passage by a much thinner leakage slot. As a consequence, the flow is well directed towards the endwall. Also, the exit of the leakage slot is aligned with the shape of the contoured endwall, which lowers the injection angle and hence makes the coolant stay nearer to the endwall. The momentum flux ratio of the exiting coolant to mainstream flow is much higher for a given MFR for the stator cascade than for the rotor cascade due to the differences in design. Thus, this high momentum coolant is able to resist, to some extent the cross-stream pressure gradient and covers the pressure side in a better manner.

It has been found in previous studies performed on the rotor cascade in the same laboratory that a thick approach flow temperature profile (simulating combustor liner coolant) is useful in supplying coolant that is above the passage vortex [3], [80]. This coolant that is sufficiently away from the endwall (or the region where the passage vortex begins to develop near the leading edge), comes down the pressure wall of the blade and across the endwall to cool the downstream portions of the passage and hence yield higher effectiveness values. One may expect downstream portions of the rotor passage to have lower values of effectiveness in case of a thinner approach flow temperature profile.

Another factor that may significantly contribute to the performance of the cascades is the endwall contour shape and overall passage geometry. For the rotor passage, the endwall contouring is steep and is present in the leading edge region, whereas for the stator passage the gradual contour shape extends throughout the passage. Although the contour shape in the rotor stage supplies more momentum to the coolant by means of acceleration in the leading edge region, these effects are lost further downstream. Therefore, slightly

better coolant coverage can be observed in the leading edge region for the rotor passage than that of the stator passage. The gradual contouring scheme of the stator passage accelerates the flow further helping the near-wall fluid to sustain the strong endwall cross flows and other secondary flows. Additionally, the flow through the stator passage is highly accelerated due to the functional requirement of the gas turbine stator, as can be determined by comparing the static pressure loss coefficients around the blade mid-span for both passages (Figure 5-1 and Figure 0-2). However, the low aspect ratio of the stator cascade makes the effect of secondary flows more pronounced on the overall flow field.

After looking into the general trend differences for both cascades, it is interesting to study the effects of leakage mass flow rates on the endwall effectiveness. Clearly, on changing the MFR from one value to another, the rotor passage shows much more sensitivity than shown in the stator passage. The coolant core in the upstream region increases considerably as the MFR goes from 0.5% to 1.0% for the rotor passage. The pressure side effectiveness values of the stator passage are very similar for different MFR cases while the pressure side effectiveness values of the rotor passage increase (mostly in first half of the passage) as the MFR is increased. However, the exit plane effectiveness values become similar for the rotor passage also.

In the rotor cascade, as the MFR increases, not only does the coolant eject out with greater momentum that helps it to counter the strong secondary flow structures forming in the stagnation region, but also within the leakage slot the ingression of the mainstream flow is reduced (refer Figure 8-3). Thus, varying the MFR has a significant effect on the adiabatic effectiveness values. In the stator cascade, on the other hand, even at a lower MFR, significantly higher effectiveness values are observed due to higher momentum flux

and resultant ability to compete with endwall cross flows and other secondary flows. Therefore, on changing the MFR, huge differences are not observed.

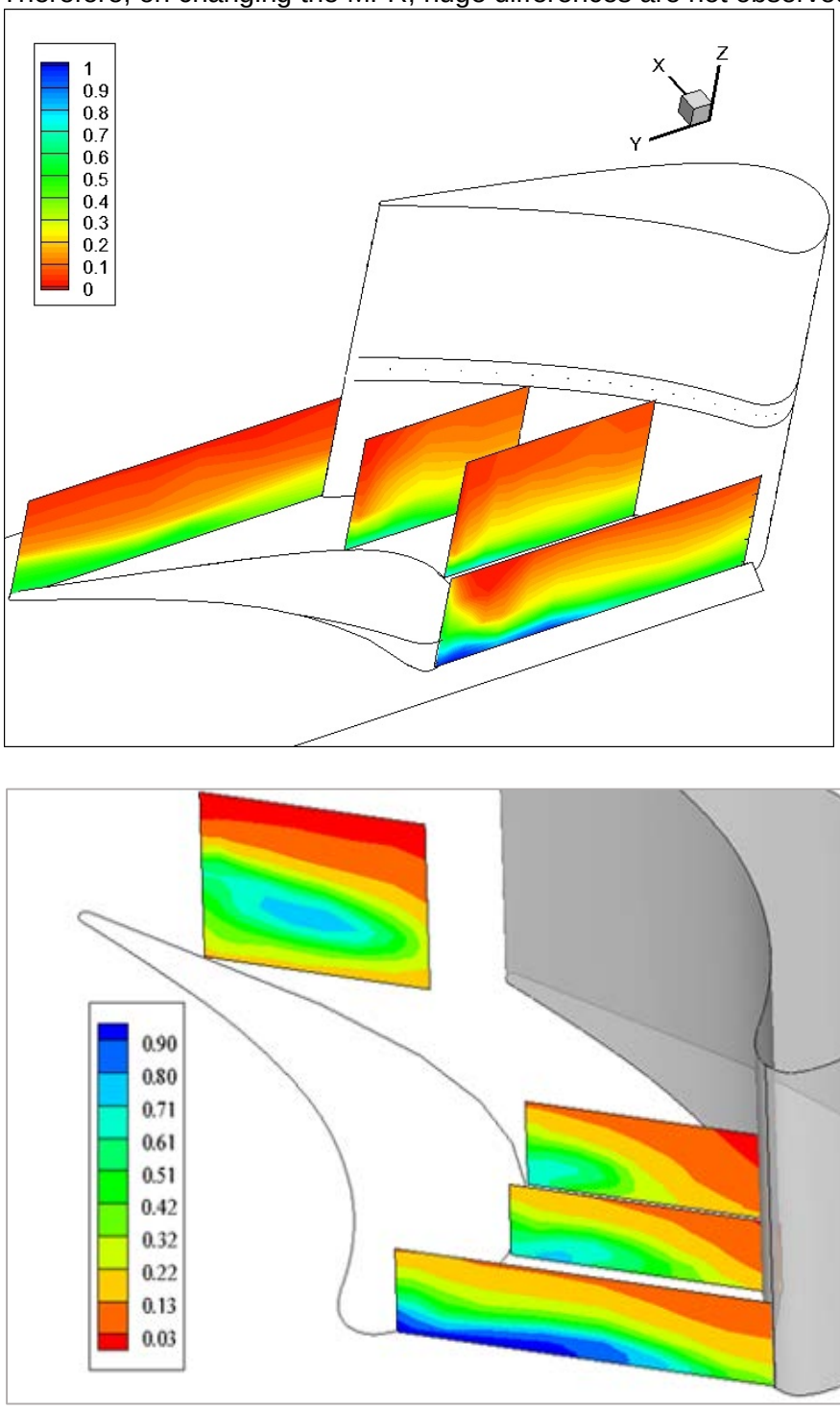

Figure 8-8: Passage thermal fields based on passage maximum inlet temperature at MFR 0.5% for (Top) Stator cascade and (Bottom) Rotor cascade

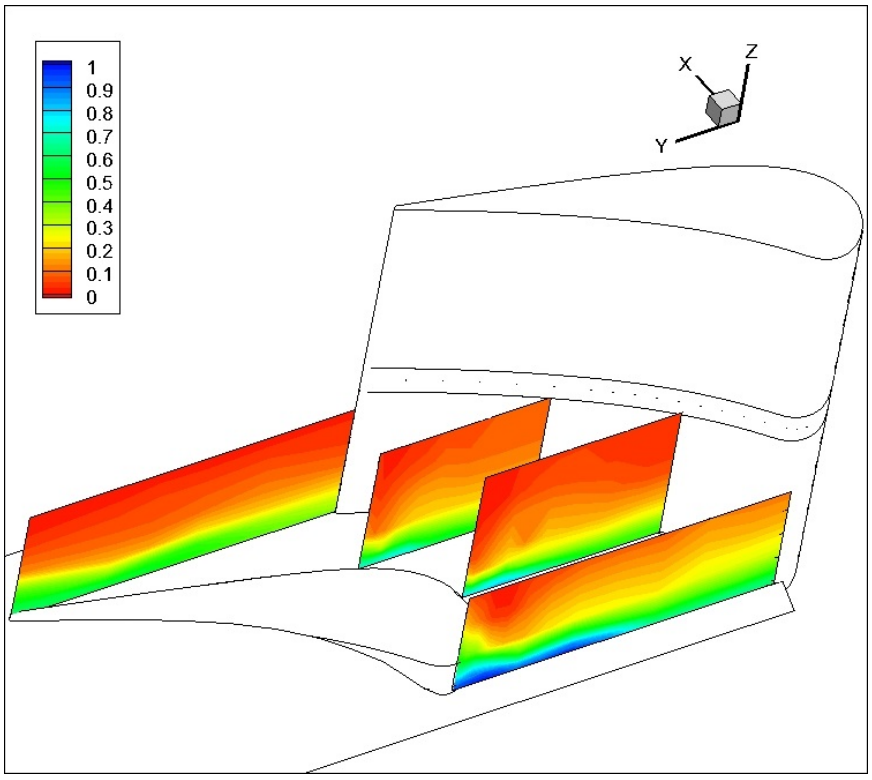

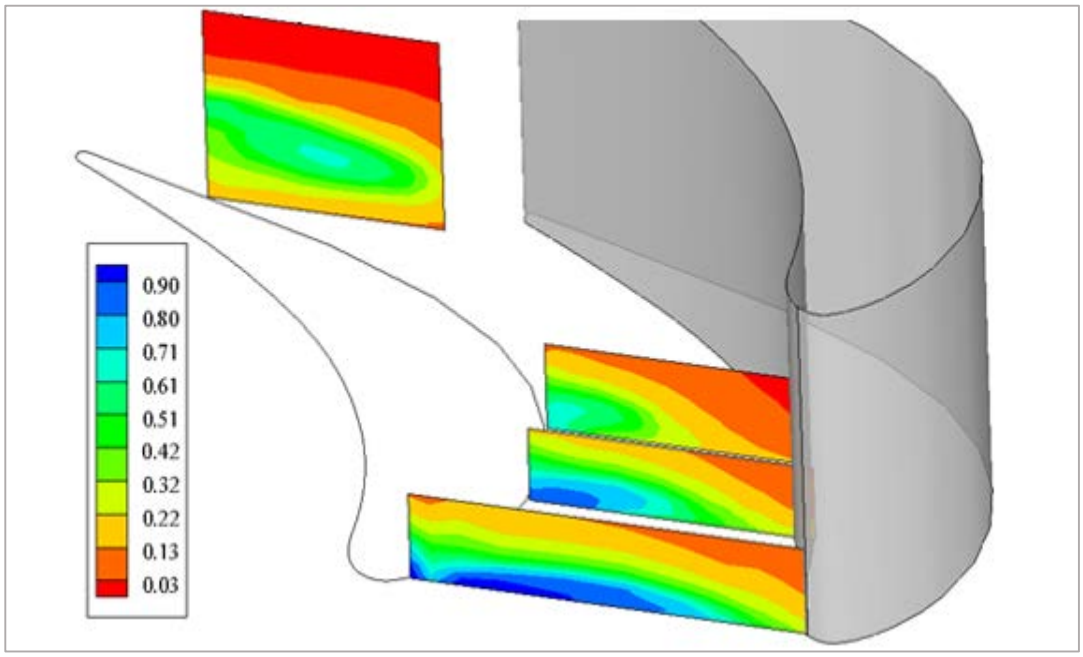

Figure 8-9: Passage thermal fields based on passage maximum inlet temperature at MFR 1.0% for (Top) Stator cascade and (Bottom) Rotor cascade

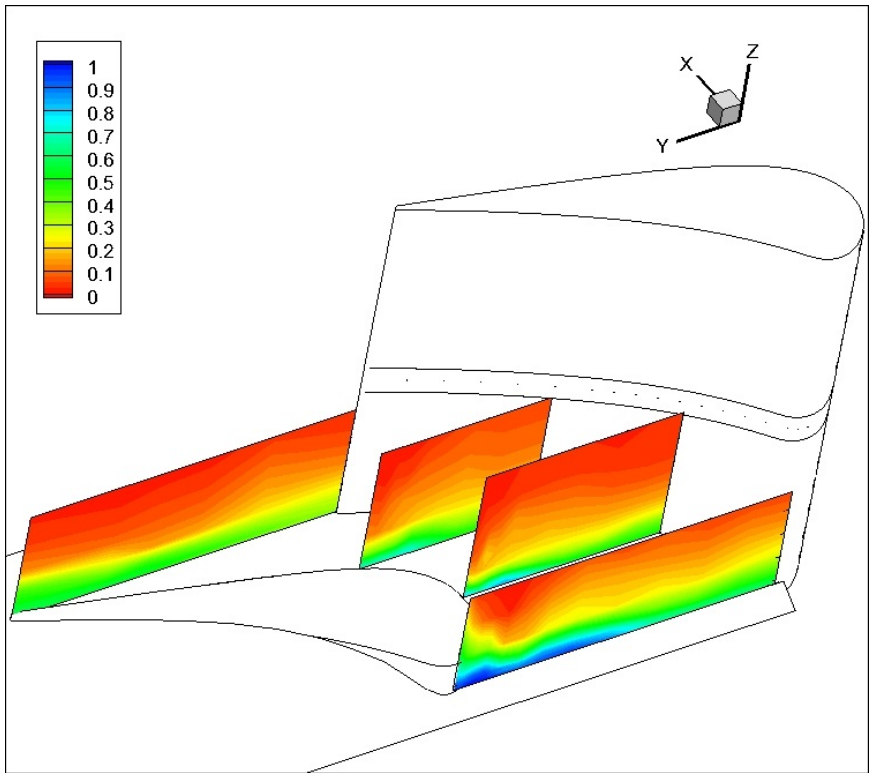

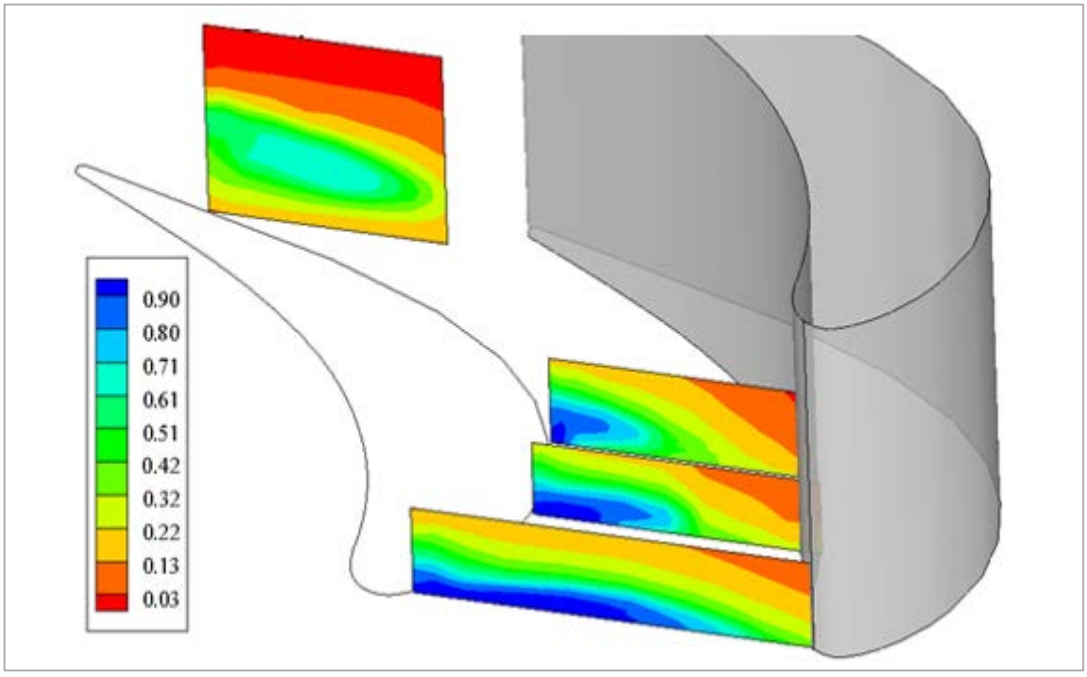

Figure 8-10: Passage thermal fields based on passage maximum inlet temperature at MFR 1.5% for (Top) Stator cascade and (Bottom) Rotor cascade

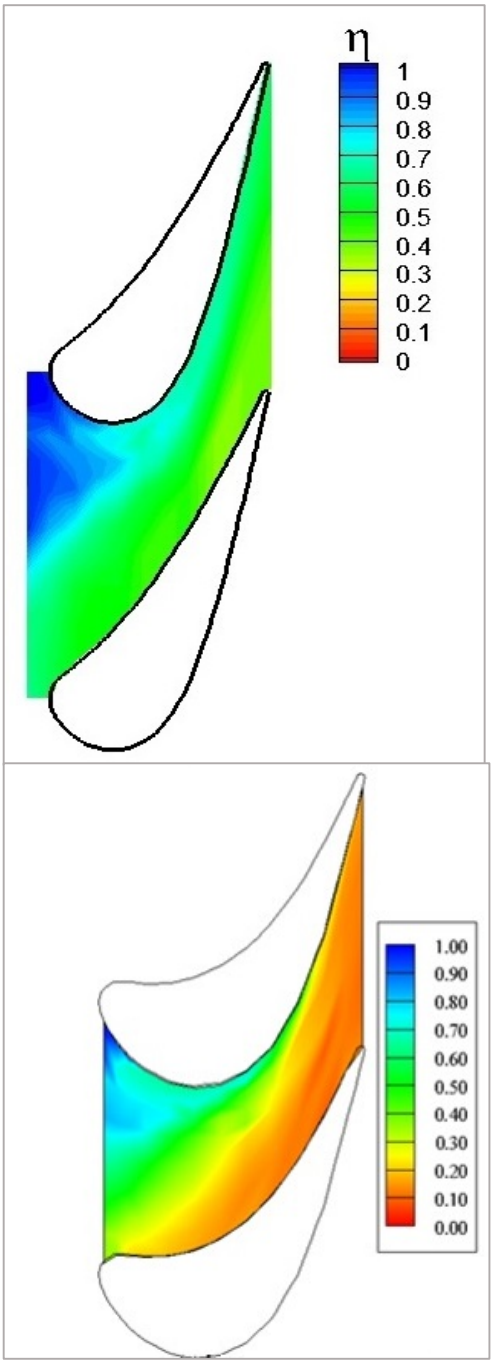

Figure 8-11: Endwall adiabatic effectiveness based on passage maximum inlet temperature at MFR 0.5% for (Top) Stator cascade and (Bottom) Rotor cascade

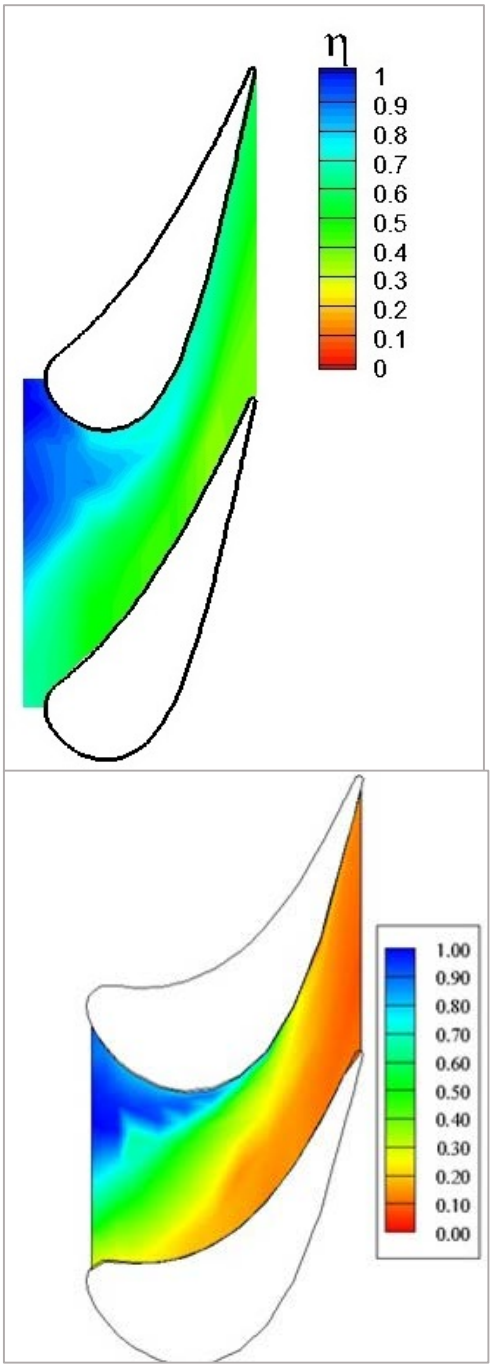

Figure 8-12: Endwall adiabatic effectiveness based on passage maximum inlet temperature at MFR 1.0% for (Top) Stator cascade and (Bottom) Rotor cascade

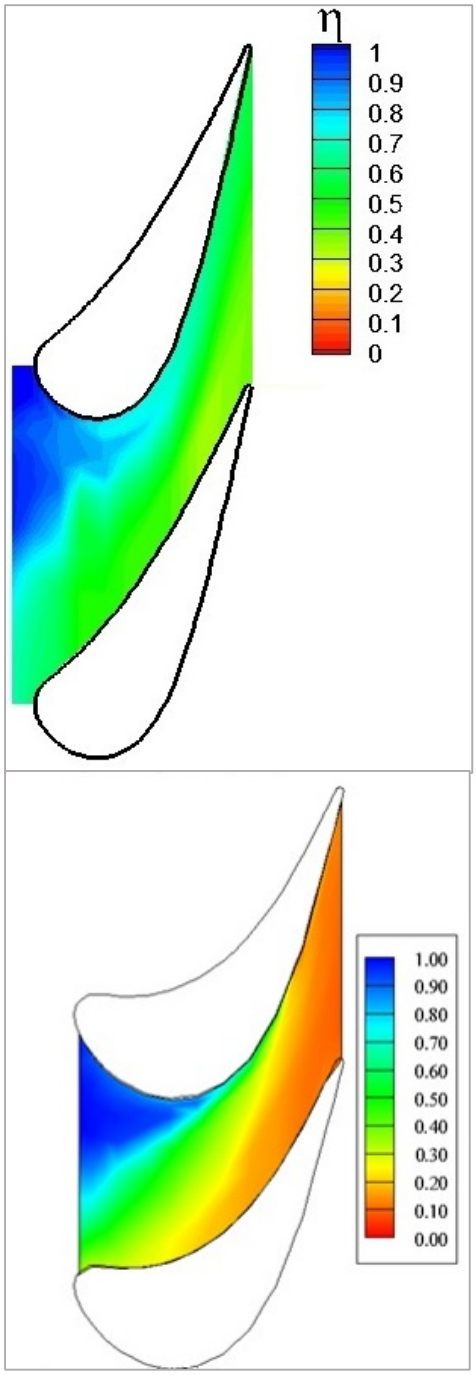

Figure 8-13: Endwall adiabatic effectiveness based on passage maximum inlet temperature at MFR 1.5% for (Top) Stator cascade and (Bottom) Rotor cascade

Chapter 9 Conclusion

An experimental study is performed on a linear, stationary two-passage cascade that represents a first stage high pressure turbine stator of a modern industrial gas turbine. The aim is to develop an understanding of the flow physics of coolant migration and mixing with the mainstream flow within the passage. This knowledge is essential for a gas turbine designer in developing efficient cooling management techniques for the hub endwall region that lies in extremely high temperature conditions. The cooling potential of *leakage* flow and *combustor liner coolant* in the approach flow is explored. The cascade passage is equipped with a *contoured* endwall to assess its role in enhancing the cooling flow effectiveness. The leakage slot geometry simulates the thin interfacial gap between the combustor exit and the first stage stator. Passage thermal fields and endwall adiabatic effectiveness values are measured at leakage mass flow rates of 0.5%, 1.0% and 1.5% of the mainstream mass flow rate. The effect of combustor liner coolant is included in the form of a non-uniform, *engine representative* approach flow temperature profile to the test section. The major approach flow characteristics include high turbulence levels (11%), large eddy length scales (~9 cm) and high Reynolds number (385,000) which are representative of real combustor exit conditions.

Another test facility under consideration in the present study is an experimental cascade representing a first stage rotor of a high pressure gas turbine. The approach flow characteristics remain the same and the test conditions involve leakage mass flow ratios of 0.5%, 1.0% and 1.5% and an engine representative approach flow temperature profile. The major differences between the stator cascade and the rotor cascade are the geometries of the leakage slot, the contouring of the endwall and the overall cascade

layout (vane vs rotor). Detailed measurements of thermal fields within the leakage slot of the rotor cascade are performed. Also, comparisons of passage thermal fields and endwall adiabatic effectiveness values are made for both test facilities to understand the differences in performance of the two cascades. The comparison allows assessing the varying coolant flow migrations patterns for both cascades under different design and operational conditions.

From the results obtained in the stator cascade test facility, for any leakage mass flow ratio, it is observed that the coolant coverage is much more near the suction side of the passage than the pressure side due to the cross-stream pressure gradient and resulting endwall cross flows. As one moves to downstream portions of passage, the coolant coverage reduces due to mixing out with the turbulent mainstream flow and secondary vortex structures. In the leading edge region, the effects of the horseshoe vortex are quite visible as it mixes out the coolant ejected from the upstream slot and reduces the coolant core magnitude and size. This makes the leading edge region cooling very difficult and in a real gas turbine must be further cooled with additional forms of cooling such as impingement cooling. The thin leakage slot geometry in the stator cascade test facility supplies the leakage coolant flow with high momentum flux, which enables the coolant to remain nearer to the endwall region and provide enhanced coolant coverage. The contoured endwall also contributes by accelerating the flow, thinning the inlet boundary layer and consequently weakening vortices forming in that region. Also, endwall contouring extends throughout the passage which provides momentum to the near-wall coolant fluid within the passage to resist endwall cross flows and other corner vortices to provide better coverage even on the pressure side and downstream regions.

It is interesting to analyze the effect of varying leakage mass flow ratios (MFR) on the endwall adiabatic effectiveness. For the stator cascade test facility, as MFR increases, the coolant coverage increases as expected due to higher mass and momentum flux ratios. However, on further increasing the MFR (from 1.0% to 1.5%) the coverage reduces. This is attributed to the high momentum flux of leakage flow that makes it 'shoot' into the mainstream flow resulting in lowered magnitudes and coverage.

Useful information can be gained by performing a comparison study between the stator cascade test facility and the rotor cascade test facility. On measuring thermal fields within the *large* leakage slot of the rotor cascade, it is found that there is a loss of two-dimensionality along the pitchwise direction marked by mixing and sloshing of the fluid in the slot itself. It is accompanied by ingression of mainstream flow that only makes the leakage flow distribution more non-uniform. Consequently, the effectiveness magnitudes are lowered when the coolant is actually ejected out of the slot because of this in-slot mixing. This marks a major difference between the stator cascade and the rotor cascade performance in this study where in the stator cascade, higher effectiveness values (relative to inlet plane) are observed. Also, the coolant flow migration patterns differ for both cases. While in the rotor, the coolant is easily carried off by the passage vortex, in the stator cascade the coolant is ejected out with high momentum due to the shape of leakage slot, and remains nearer to the endwall. Therefore, a strong dependence of the combined effects of leakage slot geometry, endwall profile shape and leakage mass and momentum flux ratios on the film cooling effectiveness is identified.

It is clear that interaction between cooling flows and secondary flows is quite complex and highly dependent on various geometrical and operational parameters. In order to assist gas turbine designers in developing efficient gas turbines or correlations for robust CFD

models, it is important to provide more detailed physical explanations of the flow patterns. Therefore, this study is an attempt in that direction. Detailed flow visualization measurements of the mixing region and effect of varying approach flow temperature profiles can be useful additions to the present study.

Bibliography

[1] F. Haselbach and H.-P. Schiffer, “AITEB — An european research project on aero-thermodynamics of turbine endwalls and blades,” *J. Therm. Sci.*, vol. 13, no. 2, pp. 97–108, May 2004.

[2] S. P. Lynch and K. A. Thole, “The Effect of the Combustor-Turbine Slot and Midpassage Gap on Vane Endwall Heat Transfer,” *J. Turbomach.*, vol. 133, no. 4, p. 041002, Oct. 2011.

[3] Y. Y. Seah, R. Erickson, and T. Simon, “Effects of Combustor Exit Temperature Profile on Adiabatic Effectiveness of Leakage Flow Film Cooling over an Axisymmetric Endwall,” in *ASME Turbo Expo, GT2013-96032*, 2013.

[4] S. W. Burd and T. W. Simon, “Flow Measurements in a Nozzle Guide Vane Passage With a Low Aspect Ratio and Endwall Contouring,” *J. Turbomach.*, vol. 122, no. 4, p. 659, Oct. 2000.

[5] I. Miyoshi, S. Higuchi, and T. Kishibe, “Improving the Performance of a High Pressure Gas Turbine Stage Using a Profiled Endwall,” in *Volume 6A: Turbomachinery*, 2013, p. V06AT36A027.

[6] W. A. Eckerle and L. S. Langston, “Horseshoe Vortex Formation Around a Cylinder,” *J. Turbomach.*, vol. 109, no. 2, p. 278, 1987.

[7] H. Z. Herzig, A. Hansen, and G. R. Costello, “A Visualization Study Of Secondary Flows in Cascades,” 1954.

[8] W. A. Eckerle and L. S. Langston, “Horseshoe Vortex Formation Around a Cylinder,” *J. Turbomach.*, vol. 109, no. 2, p. 278, Apr. 1987.

[9] F. J. Pierce and J. Shin, “The Development of a Turbulent Junction Vortex System (Data Bank Contribution),” *J. Fluids Eng.*, vol. 114, no. 4, p. 559, Dec. 1992.

[10] R. J. Goldstein and J. Karni, “The Effect of a Wall Boundary Layer on Local Mass Transfer From a Cylinder in Crossflow,” *J. Heat Transfer*, vol. 106, no. 2, p. 260, May 1984.

[11] T. W. Simon and J. D. Piggush, “Turbine endwall aerodynamics and heat transfer,” *J. Propuls. Power*, vol. 22, no. 2, pp. 301–312, 2006.

[12] L. S. Langston, “Crossflows in a Turbine Cascade Passage,” *J. Eng. Power*, vol. 102, no. 4, p. 866, Oct. 1980.

[13] L. S. Langston, M. L. Nice, and R. M. Hooper, “Three-Dimensional Flow Within a Turbine Cascade Passage,” *J. Eng. Power*, vol. 99, no. 1, p. 21, Jan. 1977.

[14] C. H. Sieverding and P. Van den Bosche, “The use of coloured smoke to visualize secondary flows in a turbine-blade cascade,” *J. Fluid Mech.*, vol. 134, p. 85, 1983.

[15] T. Kawai, S. Shinoki, and T. Adachi, “Visualization Study of Three-Dimensional Flows in a Turbine Cascade Endwall Region,” *JSME Int. journal. Ser. 2, Fluids Eng. heat Transf. power, Combust. Thermophys. Prop.*, vol. 33, no. 2, pp. 256–264, May 1990.

[16] J. T. Chung and T. W. Simon, “Three-dimensional flow near the blade/endwall junction of a gas turbine. Visualization in a large-scale cascade simulator,” in *American Society of Mechanical Engineers (Paper)*, 1990.

[17] H. P. Wang, S. J. Olson, R. J. Goldstein, and E. R. G. Eckert, “Flow Visualization in a Linear Turbine Cascade of High Performance Turbine Blades,” *J. Turbomach.*, vol. 119, no. 1, p. 1, Jan. 1997.

[18] F. C. Kopper, R. Milanot, and M. Vancot, “Experimental Investigation of Endwall Profiling in a Turbine Vane Cascade,” *AIAA J.*, vol. 19, no. 8, pp. 1033–1040, Aug. 1981.

[19] G. Brennan, N. W. Harvey, M. G. Rose, N. Fomison, and M. D. Taylor, “Improving the Efficiency of the Trent 500-HP Turbine Using Nonaxisymmetric End Walls—Part I: Turbine Design,” *J. Turbomach.*, vol. 125, no. 3, p. 497, Jul. 2003.

[20] M. G. Rose, N. W. Harvey, P. Seaman, D. A. Newman, and D. McManus, “Improving the Efficiency of the Trent 500 HP Turbine Using Non-Axisymmetric End Walls: Part II — Experimental Validation,” in *Volume 1: Aircraft Engine; Marine; Turbomachinery; Microturbines and Small Turbomachinery*, 2001, p. V001T03A081.

[21] M. T. Schobeiri and K. Lu, “Endwall Contouring Using Continuous Diffusion: A New Method and its Application to a Three-Stage High Pressure Turbine,” *J. Turbomach.*, vol. 136, p. 011006, 2013.

[22] J. T. Chung and T. W. Simon, “Effectiveness of the gas turbine endwall fences in secondary flow control at elevated freestream turbulence levels,” in *American Society of Mechanical Engineers (Paper)*, 1993, pp. 1–8.

[23] T. Kawai, S. Shinoki, and T. Adachi, “Secondary Flow Control and Loss Reduction in a Turbine Cascade Using Endwall Fences,” *JSME Int. journal. Ser. 2, Fluids Eng. heat Transf. power, Combust. Thermophys. Prop.*, vol. 32, no. 3, pp. 375–387, Aug. 1989.

[24] N. V. Aunapu, R. J. Volino, K. A. Flack, and R. M. Stoddard, “Secondary Flow Measurements in a Turbine Passage With Endwall Flow Modification,” *J. Turbomach.*, vol. 122, no. 4, p. 651, Oct. 2000.

[25] M. F. Blair, “An Experimental Study of Heat Transfer and Film Cooling on Large-Scale Turbine Endwalls,” *J. Heat Transfer*, vol. 96, no. 4, p. 524, Nov. 1974.

[26] R. A. Graziani, M. F. Blair, J. R. Taylor, and R. E. Mayle, “An Experimental Study of Endwall and Airfoil Surface Heat Transfer in a Large Scale Turbine Blade Cascade,” *J. Eng. Power*, vol. 102, no. 2, p. 257, Apr. 1980.

[27] G. N. Kumar, R. M. Jenkins, and U. Sahu, “Regionally averaged endwall heat transfer correlations for a linear vane cascade,” *ASME*, 1985.

[28] R. J. Goldstein and R. A. Spores, “Turbulent Transport on the Endwall in the Region Between Adjacent Turbine Blades,” *J. Heat Transfer*, vol. 110, no. 4a, p. 862, Nov. 1988.

[29] N. S. Sharp, S. Neuscamman, and Z. Warhaft, “Effects of large-scale free stream turbulence on a turbulent boundary layer,” *Phys. Fluids*, vol. 21, no. 9, p. 095105, Sep. 2009.

[30] L. Sang Woo, K. Hyun Goo, and P. Byung-Kyu, “Effects of combustor-level high free-stream turbulence on blade-surface heat/mass transfer in the three-dimensional flow region near the endwall of a high-turning turbine rotor cascade,” *J. Mech. Sci. Technol.*, vol. 19, no. 8, pp. 1347–1357, 2005.

[31] S. W. Lee, S. B. Jun, B.-K. Park, and J. S. Lee, “Effects of combustor-level high inlet turbulence on the endwall flow and heat/mass transfer of a high-turning turbine rotor cascade,” *KSME Int. J.*, vol. 18, no. 8, pp. 1435–1450, 2004.

[32] A. Perdichizzi, “Mach Number Effects on Secondary Flow Development Downstream of a Turbine Cascade,” *J. Turbomach.*, vol. 112, no. 4, p. 643, Oct. 1990.

[33] K. S. Hermanson and K. . Thole, “www2.mne.psu.edu_psuexccl_Pubs_2000-Hermanson-IJTJE.pdf,” *Int. J. Turbo Jet Engines*, pp. 179–196, 2000.

[34] M. F. Blair, “An Experimental Study Heat Transfer in a Large-Scale Turbine Rotor Passage,” *J. Turbomach.*, vol. 116, no. 1, p. 1, Jan. 1994.

[35] M. Lorenz, A. Schulz, and H.-J. Bauer, “An Experimental Study of Airfoil and Endwall Heat Transfer on a Linear Turbine Blade Cascade — Secondary Flow and Surface Roughness Effects,” *Heat Transf. Res.*, vol. 41, no. 8, pp. 867–887, 2010.

[36] M. Stripf, A. Schulz, and H.-J. Bauer, “Roughness and Secondary Flow Effects on Turbine Vane External Heat Transfer,” *J. Propuls. Power*, vol. 23, no. 2, pp. 283–291, Mar. 2007.

[37] C. H. Sieverding and P. Wilputte, “Influence of Mach Number and End Wall Cooling on Secondary Flows in a Straight Nozzle Cascade,” *J. Eng. Power*, vol. 103, no. 2, p. 257, Apr. 1981.

[38] T. E. Biesinger and D. G. Gregory-smith, “Reduction In Secondary Flows and Losses in a Turbine Cascade By Upstream Boundary Layer Blowing,” 1993.

[39] S. D. Yapa, C. J. Elkins, and J. K. Eaton, “Gt2014-25484 Endwall Vortex Effects on Turbulent Dispersion of Film Coolant,” pp. 1–10, 2014.

[40] W. Ghopa Wan Aizon, K. Funazaki, and T. Miura, “Purge flow effect on aerodynamics performance in high-pressure turbine cascade,” *J. Mech. Sci. Technol.*, vol. 27, no. 6, pp. 1611–1617, Jul. 2013.

[41] A. A. Thrift, K. A. Thole, and S. Hada, “Effects of Orientation and Position of the Combustor-Turbine Interface on the Cooling of a Vane Endwall,” *J. Turbomach.*, vol. 134, no. 6, p. 061019, Nov. 2012.

[42] K. a. Thole and D. G. Knost, “Heat transfer and film-cooling for the endwall of a first stage turbine vane,” *Int. J. Heat Mass Transf.*, vol. 48, pp. 5255–5269, 2005.

[43] A. A. Thrift, K. A. Thole, and S. Hada, “Effects of an Axisymmetric Contoured Endwall on a Nozzle Guide Vane: Adiabatic Effectiveness Measurements,” *J. Turbomach.*, vol. 133, no. 4, p. 041007, Oct. 2011.

[44] B. Laveau, R. S. Abhari, M. E. Crawford, and E. Lutum, “High Resolution Heat Transfer Measurement on Flat and Contoured Endwalls in a Linear Cascade,” *J. Turbomach.*, vol. 135, no. July 2013, p. 041020, 2013.

[45] P. Schuepbach, R. S. Abhari, M. G. Rose, and J. Gier, “Influence of Rim Seal Purge Flow on the Performance of an Endwall-Profiled Axial Turbine,” *J. Turbomach.*, vol. 133, no. 2, p. 021011, Apr. 2011.

[46] T. W. Simon and R. Erickson, “Effects of Stator/Rotor Leakage Flow and Axisymmetric Contouring on Endwall Adiabatic Effectiveness and Aerodynamic Loss,” *Heat Transf. Res.*, vol. 42, no. 1, pp. 45–64, 2011.

[47] K. S. Hermanson and K. A. Thole, “Effect of Inlet Conditions on Endwall Secondary Flows,” *J. Propuls. Power*, vol. 16, no. 2, pp. 286–296, Mar. 2000.

[48] M. D. Barringer, K. A. Thole, and M. D. Polanka, “Effects of Combustor Exit Profiles on Vane Aerodynamic Loading and Heat Transfer in a High Pressure Turbine,” *J. Turbomach.*, vol. 131, no. 2, p. 021008, Apr. 2009.

[49] A. Suryanarayanan, B. Ozturk, M. T. Schobeiri, and J. C. Han, “Film-Cooling Effectiveness on a Rotating Turbine Platform Using Pressure Sensitive Paint Technique,” *J. Turbomach.*, vol. 132, no. 4, p. 041001, Oct. 2010.

[50] A. A. Thrift and K. A. Thole, “Influence of flow injection angle on a leading-edge horseshoe vortex,” *Int. J. Heat Mass Transf.*, vol. 55, no. 17–18, pp. 4651–4664, Aug. 2012.

[51] Y. Zhang, X. Yuan, and P. Ligrani, “Film cooling effectiveness distribution on first-stage vane endwall with and without leading-edge fillets,” *Int. J. Heat Mass Transf.*, vol. 66, pp. 642–654, Nov. 2013.

[52] M. Salcudean, I. Gartshore, K. Zhang, and Y. Barnea, “Leading Edge Film Cooling of a Turbine Blade Model Through Single and Double Row Injection: Effects of Coolant Density,” in *Volume 4: Heat Transfer; Electric Power; Industrial and Cogeneration*, 1994, p. V004T09A002.

[53] S. V. Ekkad, J. C. Han, and H. Du, “Detailed Film Cooling Measurements on a Cylindrical Leading Edge Model: Effect of Free-Stream Turbulence and Coolant Density,” *J. Turbomach.*, vol. 120, no. 4, p. 799, Oct. 1998.

[54] R. D. Erickson, “Experimental investigation of disc cavity leakage flow and hub endwall contouring in a linear rotor cascade.,” M.S. Thesis, University of Minnesota, Twin Cities, 2010.

[55] F. E. Ames, “Experimental Study of Vane Heat Transfer and Film Cooling at Elevated Levels of Turbulence,” 1996.

[56] J. T. Chung, “Flow and Heat Transfer Experiments in the Turbine Airfoil/Endwall Region,” PhD Thesis, University of Minnesota, Minneapolis, MN, 1992.

[57] L. Wang, “A Study on Gas Turbine Flows, Turbulence Generation, and Film Cooling Flow Measurements,” University of Minnesota, Minneapolis, MN, 1996.

[58] M. J. Assael, K. D. Antoniadis, and J. Wu, “New Measurements of the Thermal Conductivity of PMMA, BK7, and Pyrex 7740 up to 450K,” *Int. J. Thermophys.*, vol. 29, no. 4, pp. 1257–1266, Aug. 2008.

[59] R. Shaw, “The influence of hole dimensions on static pressure measurements,” *J. Fluid Mech.*, vol. 7, no. 04, p. 550, Mar. 2006.

[60] R. J. Goldstein, *Fluid Mechanics Measurements*. Taylor and Francis, 1996.

[61] G. Sovran, *Fluid Mechanics of Internal Flow*. Amsterdam-London-New York: Elsevier Publishing Company, 1967.

[62] R. D. Blevins, *Theoretical Diffuser Performance, Applied Fluid Dynamics Handbook*. New york, 1984.

[63] J. D. Piggush, “An Experimental Investigation of Endwall Leakage Flows and Misalignment in Gas Turbine Nozzle Guide Vane,” M.S. Thesis, University of Minnesota, Twin Cities, 2005.

[64] L. V. King, “On the Convection of Heat from Small Cylinders in a Stream of Fluid: Determination of the Convection Constants of Small Platinum Wires with Applications to Hiot- Wire Anemometry,” vol. 214. Philosophical Transactions of the Royal Society of London, pp. 373–432, 1914.

[65] D. J. Wilson, “An Experimental Investigation of the Mean Velocity, Temperature and Turbulence Fields in Plane and Curved Two-Dimensional Wall Jets: Coanda Effect,” PhD Thesis, University of Minnesota, Twin Cities, MN, 1970.

[66] R. Oke, “Measurements in a Gas Turbine First Stage Nozzle Guide Vane Cascade with Film Cooling and Endwall Contouring,” PHD Thesis, University of Minnesota, Twin Cities, 2001.

[67] J. A. Schetz and A. E. Fuhs, *Handbook of Fluid Dynamics and Fluid Machinery (Vol 2)*. John Wiley and Sons.

[68] Tennekes and Lumley, *A First Course in Turbulence*. The MIT Press.

[69] J. O. Hinze, *Turbulence*, 2nd Ed. McGRAW-HILL.

[70] R. B. Stull, *An Intrduction to Boundary Layer Meteorology*. Kluver Academic Publishers, 2008.

[71] A. N. Kolmogorov, “The Local Structure of Turbulence in Incompressible Viscous Fluid for Very Large Reynolds Numbers,” *Proc. R. Soc. A Math. Phys. Eng. Sci.*, vol. 434, no. 1890, pp. 9–13, Jul. 1991.

[72] F. E. Ames and R. J. Moffat, “Heat Transfer with High Intensity, Large Scale Turbulence: The Flat Plate Turbulent Boundary Layer and the Cylindrical Stagnation Point,” Report No. HMT-44, Stanford University, CA, 1990.

[73] “General Operating Instructions Validyne Variable Reluctance Pressure Transducer.” Validyne Engineering Co., pp. 2–5.

[74] G. W. Burns, M. G. Scroger, M. C. Croarkin, W. F. Guthrie, and G. F. Strouse, “Temperature-Electromotive Force Reference Funcitons and Tables for the Letter-Designated Thermocouple Types Based on the ITS-90.” N.I.S.T., 1993.

[75] “Laminar Flow Element (User’s Manual).” Meriam Instruments.

[76] R. J. Moffat, “Describing the Uncertainties in Experimental Results,” *Exp. Therm. Fluid Sci.*, 1988.

[77] S. W. Burd, C. J. Satterness, and T. W. Simon, “Effects of Slot Bleed Injection over a Contoured Endwall on Nozzle Guide Vane Cooling Performance: Part II-Thermal Measurements,” in *ASME Turbo Expo, Paper 2000-GT-200*, 2000.

[78] R. A. Oke, T. W. Simon, T. Shih, B. Zhu, L. Lin, and M. Chyu, “Measurements over a Film-Cooled, Contoured Endwall with Various Coolant Injection Rates,” in *ASME Turbo Expo, Paper 2001-GT-0140*, 2001.

[79] S. L. Dixon and C. A. Hall, *Fluid Mechanics and Thermodynamics of Turbomachinery*, Sixth Edit. Elsevier Publishing Company.

[80] A. Ayaskanta, T. W. Simon, R. Erickson, H. K. Moon, and L. Zhang, “High Pressure Turbine Rotor Stage Endwall Cooling and Passage Thermal Fields as Affected by Leakage Flow and Combustor Liner Coolant Streams,” in *Volume 8B: Heat Transfer and Thermal Engineering*, 2013, p. V08BT09A062.

[81] T. W. Simon and J. Piggush, “Hot Gas Path Heat Transfer Characteristics/Active Cooling of Turbine Components,” in *Thermal Engineering in Power Systems*, R. S. Amano and B. Sunden, Eds. WITPress, 2008.

[82] “TSI Thermal Anemometry Probes Catalog.” TSI Inc.

[83] D. A. Adolfson, “Oscillatory and Unidirectional Fluid Mechanics Investigations in a Simulation of a Stirling Engine Expansion Space,” University of Minnesota, Twin Cities, 2003.

Appendix

The following sections discuss the essential features of the rotor cascade test facility. The information provided herein gives sufficient background knowledge to the reader for understanding the results discussed in Chapter 8. For further details, reading of the test facility development by Erickson[54] is recommended. This test facility experimentally simulates the first stage rotor stage of a high pressure gas turbine, although it doesn't include the upstream first stage stator vane row. The overall set up of the test facility remains the same with similar approach flow characteristics (turbulence levels, Reynolds number and approach flow temperature profile). The major differences are the geometrical features such as blade and endwall shape, cascade layout (stator and rotor have different inlet flow angles) and leakage slot geometry.

Rotor Cascade Layout

The test facility consists of a blowing type wind tunnel driven by centrifugal and axial blowers (same upstream flow delivery system as in the stator cascade test facility). Before entering the test section, the air flow passes through the turbulence generator that produces typical low-NO_x combustor exit conditions representative of a high pressure gas turbine engine. As a result, a high free stream turbulence is obtained (turbulence intensity ~ 14%).

The test section is made up of a stationary, two-passage blade cascade as shown in Figure 0-1. The detailed dimensions are listed in Table 0-1. The coordinate system used is as follows: 'x' refers to the axial direction perpendicular to the leading edge plane of the blades ($x/C_{ax} = 0$), 'y' refers to the pitchwise direction from the pressure side to the suction side and 'z' refers to the spanwise direction. The cascade is scaled up from the actual

engine size by a factor of approximately 14. Since it represents a rotor stage of the high pressure turbine, the inlet is made to be incident at the leading edge plane at an angle (α_1 = 40˚). The blades are made up of Medium Density Fiberboard (MDF) chosen for their low thermal conductivity to have nearly zero thermal gradients at the endwall. The blade mid-span static pressure profiles are given in Figure 0-2. On comparison with stator blade static pressure profiles (Figure 5-1), it can be observed that the flow through the stator cascade undergoes higher acceleration, hence larger drop in inlet static pressure as measured by the dimensionless pressure coefficient (higher negative values of C_p).

The endwall in the study is contoured with two different shapes investigated namely 'shark nose' and 'dolphin nose', shown in Figure 0-3. They are also made up of MDF that has low thermal conductivity which enables the measurement of endwall 'adiabatic' effectiveness. The shark nose design has a more gradual slope with contouring over x/C_{ax} = -0.21 to 0.31. The dolphin nose design, on the other hand, has a steep region near the leading edge of the blade with curvature over x/C_{ax} = -0.14 to 0.06. Both the endwall shapes are placed in such a manner relative to the blades such that the span is uniform throughout from the inlet till the exit, unlike the stator cascade facility.

For exhausting the flow back into the atmosphere, a straight-walled, single channel diffuser is used with the tailboards connecting the blade exit plane to diffuser inlet. They are adjusted such that similar blade static pressure profiles are obtained for both passages ensuring same amount of flow going entering both passages.

Leakage Slot Geometry

Just upstream of the cascade is the leakage flow slot which is an experimental simulation of the leakage flow out of the stator-rotor disc cavity in a high pressure gas turbine. The leakage flow supply plenum and slot are shown in Figure 0-4. It should be noted that it is

a much larger slot than the one used in the stator cascade facility which, as shown by the experimental results, has a significant impact on the coolant flow migration and mixing. The injection slot denoted by distance h_i, simulates the rim (labyrinth) seal in the gas turbine engine where the local fluid velocities become very high. The detailed dimensions are given in Table 0-2. The leakage flow passes through this gap and enters a large open volume where it mixes and is directed upward from where it travels through the leakage slot and out into the passage. The ratio of leakage mass flow rate to approach flow mass flow rate is reported as the 'mass flow ratio (MFR). The flow to the leakage plenum is heated (~10˚C) above the mainstream flow temperature. Thus, the passage and leakage flows are of approximately the same density (within 3%).

Approach Flow Characteristics

Engine representative approach flow conditions are essential to the study which include similar turbulence characteristics, high Reynolds number and approach flow temperature

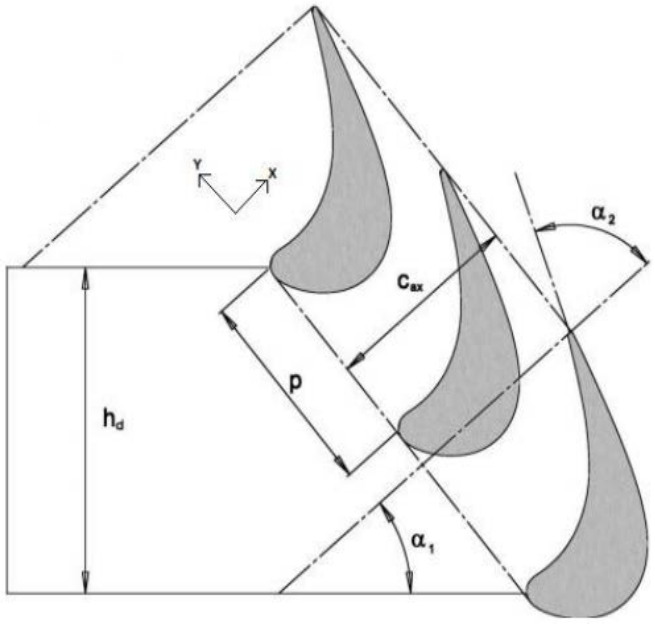

Figure 0-1: Cascade Layout [54]

profile. The approach flow characteristics are given in Table 0-3. The condition of high Reynolds number is satisfied with the inlet mean velocity being equal to 11.5 m/s (Re based on true chord length ~ 430,000). The velocity measurement is taken at an inlet plane (x/C_{ax} = -0.58) using hot wire anemometry. The turbulence characteristics are also measured at locations within this plane. The turbulence generator upstream of the tests section generates high free stream turbulence (~14%). The approach flow temperature profile is engine representative (shown in Figure 0-5) simulating the effect of combustor liner coolant presence in the combustor exit flow, It is ensured that the temperature of the wall upstream of the leakage flow slot (T_W) is maintained at a temperature equal to the leakage flow temperature (T_L) measured at the rim-seal gap as shown in Figure 0-6. The temperature, T_O, is measured at mid-span, mid-pitch location of inlet plane (x/C_{ax}= -0.25).

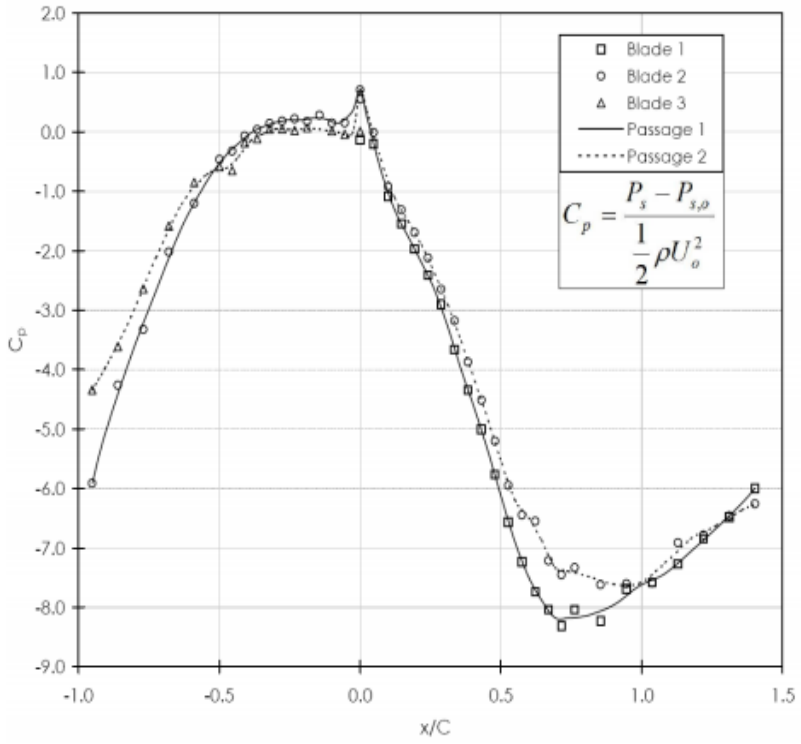

Figure 0-2: Blade mid-span static pressure profiles [54]

Measurement Techniques

The measurement of velocity, pressure and temperature are made using similar techniques and instrumentation as described in Chapter 4. Figure 0-7 shows the grid used for the measurement of passage thermal fields and endwall adiabatic effectiveness. The experimental methodology remains the same as described in Chapter 6. These topics are not repeated here for brevity. The uncertainty in the measurement of dimensionless temperature fields and effectiveness also remain similar ($\delta\eta = 0.010 - 0.013$ [3]).

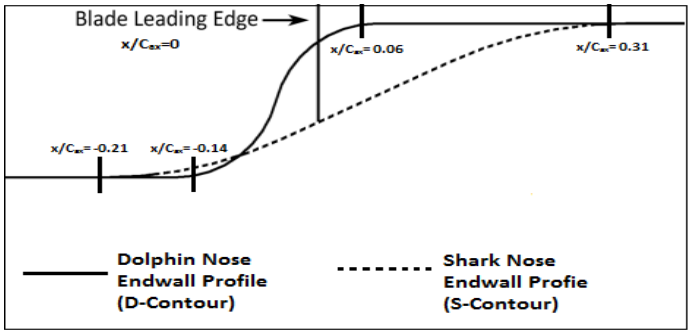

Figure 0-3: Endwall contour shapes

Table 0-1: Rotor cascade dimensions [54]

Scale Factor	14.06
Chord Length (C)	55.79 cm
Axial Chord (C_{ax})	43.20 cm
Pitch (p)	42.10 cm
Blade Aspect Ratio	1.20
Inlet Flow Angle (α_1)	40˚
Outlet Flow Angle (α_2)	70˚
Flow Turning Angle	110˚
Inlet Duct Height (h_d)	64.50 cm
Inlet Duct Width (w_d)	50.60 cm
Blade-Endwall Corner Fillet Radius	2 mm

Table 0-2: Leakage plenum dimensions in Rotor cascade [54]

Stator Endwall Lip (hs)	**2.14 cm**
Rotor Endwall Lip (hr)	**2.85 cm**
Injection Slot (hi)	**0.50 cm**
Plenum Height (hp)	**28.80 cm**
Plenum Width (wp)	**21.60 cm**
Chamfer Angle (β)	**15.0˚**

Table 0-3: Approach flow characteristics [54]

Bulk Inlet Flow Properties		**Turbulence Characteristics**	
Inlet Re_c	430,000	Λ/C	0.08-0.13
U_o	11.5 m/s	Lu/C	0.190
Tu	14%	ε	32 m^2/s^3

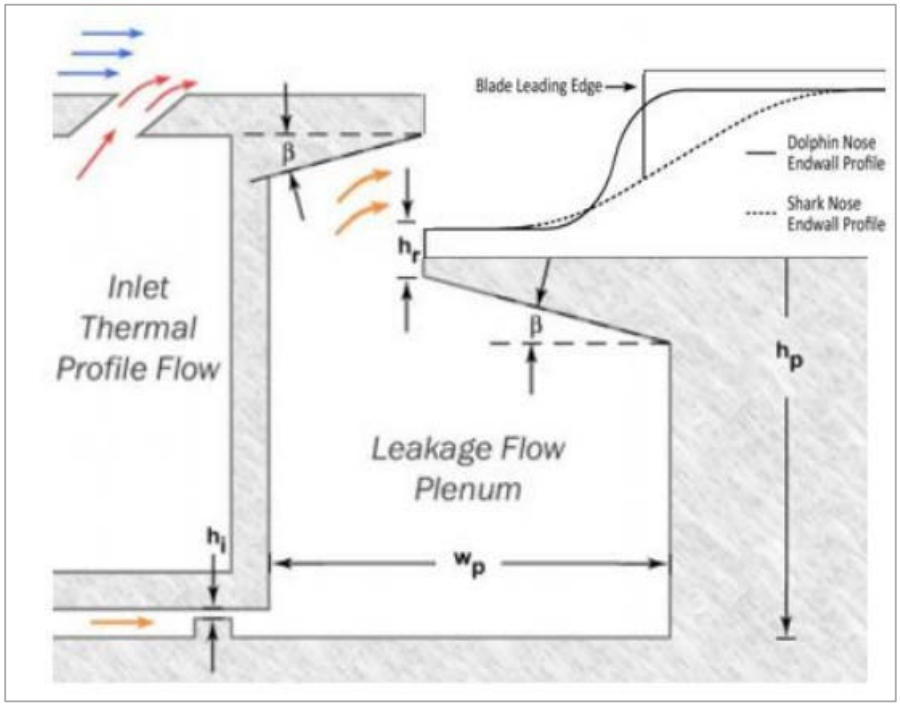

Figure 0-4: Leakage flow supply plenum [54]

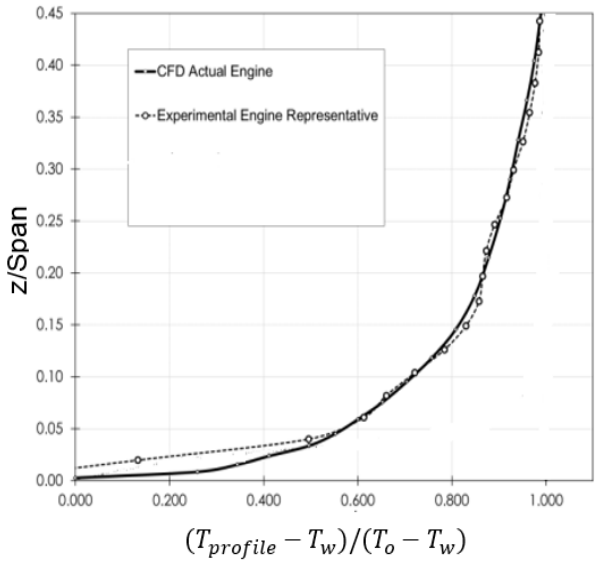

Figure 0-5: Approach flow engine representative temperature profile [54]

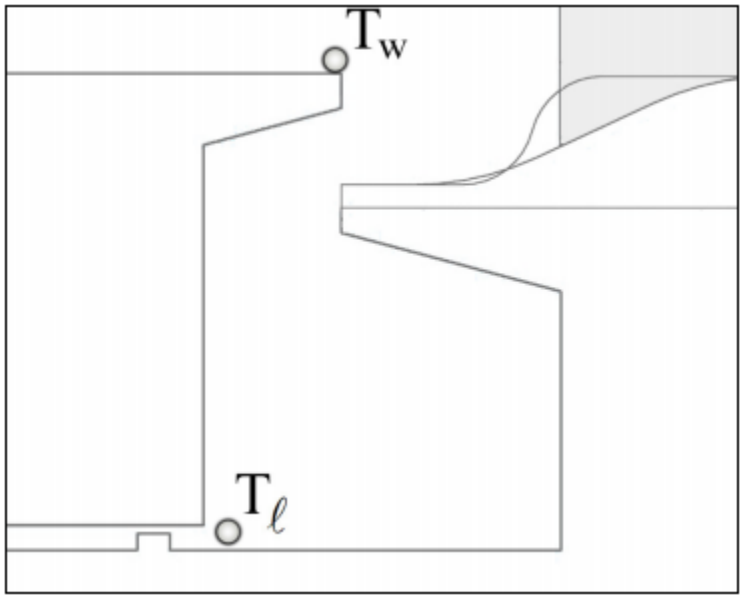

Figure 0-6: Approach flow wall and leakage flow temperature measurement locations [54]

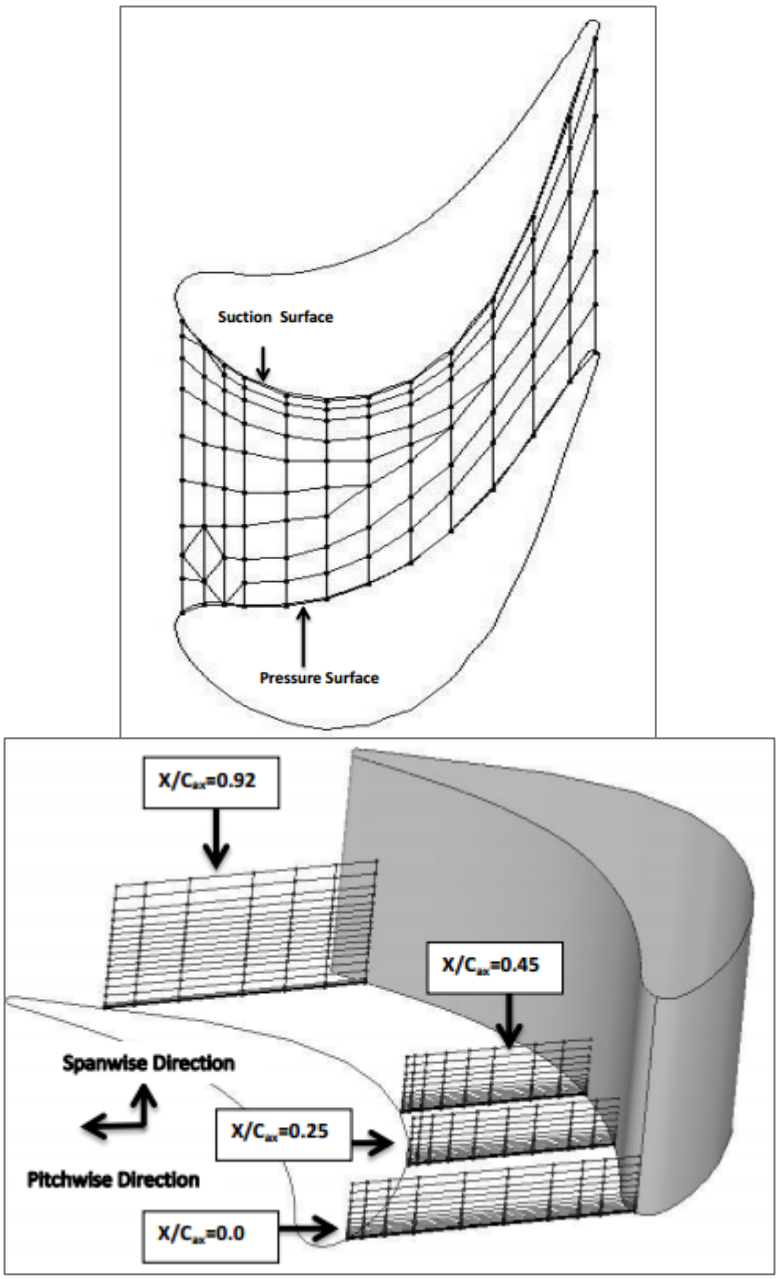

Figure 0-7: Measurement locations for (Top) Endwall adiabatic effectiveness and (Bottom) Passage thermal fields